

**Measurement of the ZZ production cross section and
limits to the anomalous Triple Gauge Couplings with
Forward Electrons with the ATLAS detector**

Dissertation
zur Erlangung des Grades
Doktor der Naturwissenschaften
am Fachbereich 08: Physik, Mathematik und Informatik
der Johannes Gutenberg-Universität
in Mainz

von
Deywis Moreno-Lopez
geboren in Bogota, Kolumbien

May 20, 2014

Datum der mündliche Prüfung: 24.06.14

Abstract

Measurements of the self coupling between bosons are important to test the electroweak sector of the Standard Model (SM). The production of pairs of Z bosons through the s-channel is forbidden in the SM. The presence of physics, beyond the SM, could lead to a deviation of the expected production cross section of pairs of Z bosons due to the so called anomalous Triple Gauge Couplings (aTGC). Proton-proton data collisions at the Large Hadron Collider (LHC) recorded by the ATLAS detector at a center of mass energy of 8 TeV were analyzed corresponding to an integrated luminosity of 20.3 fb^{-1} . Pairs of Z bosons decaying into two electron-positron pairs are searched for in the data sample. The effect of the inclusion of detector regions corresponding to high values of the pseudorapidity was studied to enlarge the phase space available for the measurement of the ZZ production. The number of ZZ candidates was determined and the ZZ production cross section was measured to be: 7.3 ± 1.0 (Stat.) ± 0.4 (Sys.) ± 0.2 (lumi.)pb, which is consistent with the SM expectation value of $7.2^{+0.3}_{-0.2}$ pb. Limits on the aTGCs were derived using the observed yield, which are twice as stringent as previous limits obtained by ATLAS at a center of mass energy of 7 TeV.

Abstract(German)

Der elektroschwache Sektor des Standardmodelles (SM) kann mit Hilfe der Messung von Selbstkopplungen zwischen Eichbosonen studiert werden. Die Erzeugung von Z -Paaren durch einen neutralen Vertex ist im SM verboten (aTGCs). Neue physikalische Prozesse könnten den Wirkungsquerschnitt der Produktion von zwei neutralen Bosonen ändern. In dieser Arbeit wird ein Datensatz von Proton-Proton-Kollisionen analysiert, um den Wirkungsquerschnitt der Produktion von zwei neutralen Bosonen zu bestimmen. Die Protonen wurden am Large-Hadron-Collider bei einer Schwerpunktsenergie von $\sqrt{s} = 8$ TeV zur Kollision gebracht. Es wurde eine gesamte Luminosität von $20,3 \text{ fb}^{-1}$ analysiert. Elektron-Positron-Paare werden in dem Datensatz selektiert. Der Effekt der Nutzung von Bereichen mit höher Pseudorapidität des Detektors wurde studiert. Der Wirkungsquerschnitt der Produktion von zwei neutralen Bosonen von 7.3 ± 1.0 (Stat.) ± 0.4 (Sys.) ± 0.2 (lumi.)pb wurde gemessen, und stimmt mit der SM-Vorhersage von $7.2_{-0.2}^{+0.3}$ pb überein . Mit der gesehenen Anzahl an Ereignisse wurden Grenzen auf aTGCs berechnet. Die Grenzen sind um einen Faktor zwei besser als die bisherigen Grenzen von ATLAS bei einer Schwerpunktsenergie von $\sqrt{s} = 7$ TeV.

Acknowledgements

Entfernt auf Grund datenschutzrechtlicher Bestimmungen.

Contents

1	Introduction	19
2	The Standard Model of Particle Physics	23
2.1	Elementary Particles	25
2.2	Symmetries within the SM	26
2.3	The Electroweak Interaction	27
2.3.1	The Higgs Mechanism	27
2.3.2	Lagrangian of the Electroweak Theory	28
2.4	Quantum Chromodynamics (QCD)	29
2.4.1	Running Coupling Constant	30
2.5	Proton-Proton Interaction	30
2.6	Production of Dibosons	32
2.6.1	Triple Gauge Coupling	33
2.6.2	Anomalous Neutral Triple Couplings (aTGC)	34
2.6.3	Diboson Searches at LEP and Tevatron	36
2.6.4	Diboson Physics at the LHC	37
2.7	PDFs and Monte Carlo (MC) Generators	39
2.8	ZZ Cross Section Prediction	41
3	The ATLAS Experiment	43
3.1	The Large Hadron Collider	43
3.2	The ATLAS Detector	45
3.2.1	Inner Detector	46
3.2.2	Pixel Detector	47
3.2.3	SemiConductor Tracker (SCT)	48
3.2.4	Transition Radiation Tracker (TRT)	48
3.3	Calorimeter System	49
3.3.1	The Electromagnetic Calorimeter	50
3.3.2	The Hadronic Calorimeter	52

3.4	Muon Spectrometer	53
3.5	Luminosity Determination in ATLAS	54
3.6	ATLAS Trigger System	55
3.6.1	Level1 Trigger (L1)	55
3.6.2	Level2 Trigger (L2)	55
3.6.3	Event Filter (EF)	55
3.7	2011 and 2012 Data Taking	56
4	Electron Reconstruction Performance in ATLAS	59
4.1	Electron Reconstruction	60
4.1.1	Sliding-window Algorithm	60
4.1.2	Topocluster Reconstruction	61
4.2	Electron Identification	61
4.2.1	Central Electron Identification	62
4.2.1.1	Cut Based Selection	63
4.2.2	Forward Electron Identification	66
4.2.3	Electron Isolation	69
4.3	Efficiency of the Identification	69
4.3.1	Efficiency Determination in Forward Region	70
4.3.1.1	Signal and Background Separation	72
4.3.1.2	Uncertainties	74
4.3.2	Efficiencies with 2010 Data Cuts	75
4.3.2.1	Efficiency as function of Eta	75
4.3.2.2	Efficiency as Function of p_T	76
4.3.2.3	Efficiency as Function of NPV	77
4.3.3	Efficiencies with Pile-up Independent Cut Set	78
4.3.3.1	Efficiency as Function of NPV	80
4.3.3.2	Efficiency as Function of p_T	80
4.3.3.3	Efficiency as Function of Eta	80
4.4	Discussion and Outlook	83
5	$ZZ \rightarrow 4e$ Events in the 2012 ATLAS Data	85
5.1	Diboson Event Selection	85
5.1.1	Data Selection	86
5.2	MC Signal and MC Backgrounds	90
5.2.1	MC Corrections	90
5.3	Data Driven Background Estimation	92
5.3.1	Matrix Method	92

CONTENTS

5.3.2	Fake Rate Estimation	94
5.4	Systematic Uncertainties to the Background Estimation	97
5.4.1	MC Systematic Uncertainties Estimation	97
5.4.2	Systematic Uncertainties for the Data Driven Background	98
5.5	Data-MC Comparison	99
5.5.1	Electron Kinematic Variables	99
5.5.2	ZZ Kinematic Variables	101
6	Cross Section Measurement	107
6.1	Fiducial and Total Cross Section Definition	107
6.2	Fiducial Volume Definition	108
6.3	Efficiency Determination	109
6.4	Acceptance Determination	110
6.5	Cross Section Calculation	112
6.6	Systematic Determination	113
6.7	Differential Cross Section	116
7	Limits on aTGC in ATLAS	117
7.1	Anomalous Triple Gauge Couplings	117
7.2	Matrix Elements Reweighting	120
7.3	Limits Extraction	122
7.3.1	Yield Determination	122
7.3.2	aTGC Limits Extraction	125
8	Conclusions	129
	Appendices	137
A	Monte Carlo Samples used in this Analysis	139
B	Signal and Background functions in Forward Region	141
C	Additional Kinematic Distributions of ZZ	143

List of Figures

2.1	Example of a proton-proton interaction	31
2.2	Example of a PDF distribution	31
2.3	Representation of the TGCs	33
2.4	ZZ production through triple gauge couplings.	34
2.5	Effect of aTGC on SM kinematic distribution	35
2.6	ZZ production via $q\bar{q}$ interaction	37
2.7	ZZ production via gluon-gluon fusion	37
2.8	Example of Z production plus gluons (a) and quarks ((b) and (c)).	38
2.9	$t\bar{t}$ production with an associate Z boson.	39
2.10	Processes with final experimental signatures similar to the ZZ	39
3.1	LHC experiments	44
3.2	ATLAS detector	45
3.3	Inner detector	47
3.4	Main components of the track system.	48
3.5	ATLAS calorimeter system.	50
3.6	Barrel part of electromagnetic calorimeter	51
3.7	Forward calorimeter.	52
3.8	Luminosity of the data taking period 2011 and 2012.	56
3.9	Number of interactions per beam crossing	57
4.1	Reconstruction and Identification in forward region	62
4.2	Signal and background fitting functions used in forward electron identification	73
4.3	Invariant mass spectrum of tag and probe pairs no identification is applied	73
4.4	Invariant mass spectrum of tag and probe pairs identification is applied	74
4.5	Efficiency in data and MC after electron identification	76
4.6	SFs as function of η	76
4.7	Identification efficiencies as a function of p_T in EMEC	77
4.8	Identification efficiencies as a function of p_T in FCal	77

4.9	Identification efficiencies as function of NPV in EMEC	78
4.10	Identification efficiencies as function of NPV in FCal	78
4.11	Identification efficiencies as function of NPV new loose identification	79
4.12	Identification efficiencies as function of NPV new medium identification	79
4.13	Identification efficiencies as function of NPV new tight identification	80
4.14	Identification efficiencies as function of p_T new loose identification	81
4.15	Identification efficiencies as function of p_T new medium identification	81
4.16	Identification efficiencies as function of p_T new tight identification	82
4.17	Identification efficiencies as function of η new loose identification	82
4.18	Identification efficiencies as function of η new medium identification	83
4.19	Identification efficiencies as function of η new tight identification	83
5.1	ZZ candidate with four central electrons	89
5.2	ZZ candidate with three central electrons and one forward.	89
5.3	Fake factors of forward electrons	95
5.4	Fake factors of central electrons	96
5.5	η distributions of electrons coming from ZZ candidates	99
5.6	p_T distributions of electrons coming from CCCF ZZ candidates	100
5.7	η and p_T distributions of electrons coming from CCCF ZZ candidates	101
5.8	Mass spectrum of leading Z	102
5.9	p_T distribution of leading Z	103
5.10	Mass spectrum of the ZZ candidates	103
5.11	p_T distribution of the ZZ candidates	104
5.12	Rapidity distribution of the ZZ candidates	104
5.13	Mass spectrum and p_T (right) of CCCC and CCCF ZZ candidates	105
6.1	ZZ events at reconstruction and generation level in PowhegPythia samples	110
6.2	ZZ events at reconstruction and generation level in ggVV samples	110
6.3	Number of ZZ events at generation level in PowhegPythia samples	111
6.4	Number of ZZ events at generation level in ggVV samples	112
6.5	Differential fiducial cross as function of the invariant mass of the ZZ	116
6.6	Differential fiducial cross as function of the p_T of the leading Z	116
7.1	Invariant mass of the ZZ events predicted by SM compared to the distribution for the TGC0 sample	118
7.2	Transverse momentum of the leading Z predicted by SM compared to the distri- bution for the TGC0 sample	118
7.3	Invariant mass of the ZZ events predicted by SM compared to the distribution for the TGC1 sample	119

LIST OF FIGURES

7.4	Transverse momentum of the leading Z predicted by SM compared to the distribution for the TGC1 sample	119
7.5	Invariant mass of the ZZ events predicted by SM compared to the distribution for the TGC0 sample reweighted to SM expectation	121
7.6	Transverse momentum of the leading Z predicted by SM compared to the distribution for the TGC0 sample reweighted to SM expectation	122
7.7	Invariant mass of the ZZ events predicted by SM compared to the distribution for the TGC2 sample reweighted	123
7.8	Transverse momentum of the leading Z predicted by SM compared to the distribution for the TGC2 sample reweighted	123
B.1	Functions used to fit the data and the background in order to make forward electron identification.	142
C.1	Invariant mass of the subleading Z	143
C.2	p_T of the subleading Z	144
C.3	Distribution of the ZZ candidates	144

Chapter 1

Introduction

One of the most successful theories in physics of recent years is the Standard Model (SM) which is a description of the properties and interactions governing the fundamental elements of matter. The development of this theory began in the middle of the 20th century, when correlations between the elementary particles started to be recognized and a mathematical framework that could explain the nature of apparently different forces was found.

An important characteristic of the SM is its capacity of simplification. The SM reduces the number of possible interactions between elementary particles and the number of fundamental interacting particles to only a few. The interactions are the basic forces of nature, i.e, electromagnetic, weak and strong forces. The masses of the fundamental particles are small, so gravity is negligible at this level. Fundamental particles can be classified as leptons or quarks, where the distinction between them arises from the possibility of interacting via the strong force.

However, the capacity of simplification of the SM is not the only characteristic that made it successful, but its capacity of making precise predictions of the existence of new particles. In order to test the SM predictions, accelerators and detectors have been developed towards the end of the last century and the beginning of the current one.

The LHC, which is one of the most recent accelerators, is a particle collider designed to test the limits of the SM. Two significant objectives were to be accomplished by the LHC: the search for the Higgs boson and the search for new phenomena not predicted by the SM. The first one has already been achieved with the discovery of a new particle with properties consistent with the Higgs boson, responsible for the generation of the mass in the observed particles.

Searches for new physics are still ongoing in the LHC physics program. The SM, as already mentioned, is successful in the description of the nature, but certain issues are beyond the SM. For example, recent experiments with neutrinos show the existence of their mass states. In the SM the mass of the neutrinos is zero.

Furthermore, new particles are needed in order to explain the nature of the so called dark matter. Particles that only interact gravitationally and are responsible for the mass distribution

around galaxies measured in cosmological experiments. These are a few examples that show why scientists believe the SM is not a final theory and new physics exist at energy scales that have not yet been tested.

The accumulated data after two years of operation at the LHC also allows for precision measurements of SM physics. Particularly in this work, the production of two neutral bosons (ZZ) is studied. The measurement of the ZZ production is important because the SM puts limits on the mechanism that generates dibosons.

The diboson production cross section is small compared to that predicted for WW or single Z . But it is experimentally a clean signature as not so many processes are available to produce the same final states as the ZZ . Additionally, such measurement is made at the LHC at an energy order of tens of TeV, not possible in previous experiments.

The existence of new physics can be studied, too, in a ZZ analysis. Production of ZZ via the ZZZ/γ vertex is forbidden in the SM. If a deviation on the number of predicted dibosons is found, one possible explanation is the existence of an anomalous triple gauge coupling between the Z bosons, as a result of new physics at energy scales beyond the reach of previous experiments.

This thesis studied the diboson production centered on the channel with four electrons¹ found at the final state and compares the effect of including electrons with high values of pseudorapidity. The document is structured as follows.

Chapter 2 is dedicated to a description of the SM and the principal components of this theoretical framework. Then, the mechanism of production of ZZ in hadron-hadron collisions is introduced and the nature of the triple gauge couplings is explained. The study of anomalous neutral triple gauge couplings is discussed and present limits on the values of latter are given. The state of the art of the experimental ZZ searches is also shown and at the end an introduction to Monte Carlo simulations is given.

Chapter 3 is dedicated to the description of the LHC. Its principals detectors are introduced and emphasis laid on the description of the ATLAS detector. The different subsystems of ATLAS are detailed and the behavior of the detector after the first years of operation is reported.

As already mentioned, this thesis is focused on the electron channel. For that reason chapter 4 shows a detailed description of the reconstruction and identification methods used for electrons in ATLAS. The development of the different identification menus is shown. The efficiency of identification of electrons at high values of the pseudorapidity is presented at the end of the chapter.

Chapters 5 and 6 are dedicated to the description of the ZZ selection and its backgrounds and the calculation of the ZZ cross section respectively, corresponding to the ATLAS data collected at a center of mass energy of 8 TeV with an integrated luminosity of approx. 20 fb^{-1} .

¹If not mentioned explicitly, electrons and positrons are not distinguished, so both are named electrons.

Finally, in chapter 7, the study of anomalous triple gauge couplings is shown. Limits on the triple gauge couplings are derived. The last chapter is dedicated to the conclusions and a short discussion about the final results.

Chapter 2

The Standard Model of Particle Physics

*“cause we are all just
Protons, Neutrons, Electrons
That rest on a Sunday
Work on a Monday”
—The Cat Empire*

The basic elements of matter, so called elementary particles (e.g., leptons and quarks) and the forces responsible for the interaction between them (e.g., strong, weak, electromagnetic force), were discovered during the first part of the past century. Subsequently, theoretical efforts were done in order to have a physics model capable of explaining the observed phenomena and minimal particle content.

As a result of the theoretical work, the interaction between elementary particles is currently well described using a framework of gauge invariant fields. Leptons and quarks interact through the exchange of quantized states of these fields (force carriers), obeying rules depending on charge properties; e.g., color, weak, electric charge. For example, the electromagnetic force can be described as the exchange of photons between particles with electric charge.

This theory of interacting particles and gauge fields is called Standard Model (SM). In the SM the elementary particles possess spin $1/2^1$, so obeying the Fermi statistics. On the other hand, the force carriers are bosons with spin 1. The relevant forces at subatomic level are the strong, weak and electromagnetic. The gravity does not play a major role at that level.

The electromagnetic and weak interactions are unified in the SM, in the electroweak theory proposed by S. Glashow, S. Weinberg and A. Salam [1]. The electroweak theory states that

¹In this thesis, natural units are used; $c=\hbar=1$. In these units, particle energy, mass and momentum are expressed in eV.

weak and electromagnetic interactions appear as separate forces due to a spontaneous symmetry breaking of the electroweak gauge field. In the electroweak gauge field, masses of the force carriers disappear and the electroweak interaction is a long range force like gravity. The spontaneous symmetry breaking (SSB) is also called Higgs mechanism [2] [3] and the particle that is responsible for the SSB is named Higgs boson.

The strong interaction carriers are gluons; they possess a color charge in three varieties red, blue and green². Gluons only couple with quark particles and with themselves. The structure of the strong interaction forbids the existence of isolated quarks and gluons. Systems bound by the strong interaction appear only as colorless combinations (confinement) and are called hadrons. Three quarks, one red, one blue and one green, form a baryon, like the proton or the neutron. One quark and one antiquark are combined to form a meson. The confinement is responsible for the short range of the strong interaction; however, the mathematical description of this interaction is very similar to that of the electromagnetism using gauge fields (QED) and it is known as quantum chromodynamics (QCD).

Experimentally, the SM has been successfully tested in most ranges of energy. Particles predicted for the model have been discovered using colliders. The strong interaction carriers were found at the Deutsches Electron Synchrotron (DESY) in the year 1979 [4] [5] [6] [7]. Four years later, the particles that are responsible for the weak interaction (W^+ , W^- and Z boson) were discovered in the Super Proton Antiproton Synchrotron ($Spp\bar{p}S$) at CERN [8] [9] [10]. The piece that remained missing in the SM, the Higgs boson, was discovered in the year 2012 at CERN using the Large Hadron Collider (LHC). The two experiments, A Toroidal LHC Apparatus (ATLAS) and the Compact Muon Solenoid (CMS) of the LHC, reported the detection of a new boson, compatible with the SM prediction, in the mass range 125-126 GeV [11] [12].

The SM is undoubtedly a successful description of our nowadays knowledge of the nature but some issues remain open:

- The excess of matter over antimatter.
- The nature of the dark matter.
- The mass of neutrinos.
- The big difference between the masses of leptons.

For that reason, searches for physics beyond the SM (BSM) is one of the most active branches in the experimental particle physics. The discovery of particles not predicted by the SM or the deviation of the values of some properties, like the self coupling between weak bosons, if found, are important as a hint for new physics.

²Quarks and gluons do not have any physical color. The names refer to an inner freedom characteristic.

In this chapter, a description of the fundamental particles and its symmetries based on the SM is presented. Subsequently, the electroweak theory and the strong interaction are discussed. The last part of the chapter is dedicated to show the physics of the production of two Z bosons using proton-proton colliders and the perspectives for the discovery of physics BSM in the production of ZZ .

2.1 Elementary Particles

An elementary particle is defined as a particle that does not have an inner structure. In the history of physics, different particles were candidates to be the fundamental pieces of matter depending, on the maximal energy attainable by the particle colliders at the time.

Our current knowledge allows us to classify the elementary particles of spin $1/2$ as fermions. Fermions can be separated into two subgroups depending on their color charge. Fermions with color charge, associated to the strong interaction, are referred to as quarks; the ones without color charge are called leptons. There are six quarks (u,d,s,c,t,b) and six kinds of leptons: three with electric charge: i.e., electrons, muons and taus; and three neutral, massless neutrinos³. Leptons and quarks can be ordered in three generations; see table 2.1, all fermions that belongs to a different generation possess similar properties and the principal difference between generations is their mass. The lightest fermions belong to the first generation. The third-generation fermions are the most massive ones. Most of the known matter in the universe is made up of first-generation fermions.

	Spin	Q	Y	I_3	Generation		
					First	Second	Third
Quarks	1/2	2/3	1/3	1/2	u(up)	c(charm)	t(top)
	1/2	-1/3	1/3	-1/2	d(down)	s(strange)	b(bottom)
Leptons	1/2	0	-1	1/2	ν_e	ν_μ	ν_τ
	1/2	-1	-1	-1/2	e	μ	τ

Table 2.1: Fermion properties. Q corresponds to the electric charge of the fermion in units of e , Y is the hypercharge and I_3 is the third component of the weak isospin [13].

The fermions listed in the previous table have a third component of the weak isospin (I_3) different from zero. Fermions with I_3 zero do not take part in the weak interaction and are referred to as right fermions. Right neutrinos do not exist in nature. The hypercharge Y is defined as shown below in equation 2.1. The importance of the hypercharge in the electroweak theory will be discussed along with the electroweak theory.

³In the SM the neutrinos do not have mass. Experiments of neutrino oscillation show that they possess a mass different to zero.

$$Y = 2(Q - I_3) \tag{2.1}$$

2.2 Symmetries within the SM

The elementary particles can be described using a framework of quantum fields. The motion equations of these matter fields ($\psi(x)$) are derived from a Lagrangian density \mathcal{L} .

One transformation α over the matter field can be written as:

$$\psi' = e^{-i\alpha}\psi \tag{2.2}$$

If the motion equations of ψ do not change after the application of the transformation α , the matter field is symmetric under phase transformation. The Noether-Theorem [14] states that this invariance can be understood as the existence of a conserved quantity.

If the transformation α is independent from the coordinate system, the referred symmetry is called a global symmetry. Additionally, the dependency of α on the spatial coordinates produces terms of the form $\partial_\mu\alpha$ when the motion equations are derived. Therefore, the Lagrangian is no longer invariant under this local phase transformation. A way to recover the invariance is to introduce a vector field A_μ that follows the same transformation, similar to the matter field (equation 2.2), and to change the differential operator $\partial_\mu\alpha$ for the covariant differential operator D_μ :

$$D_\mu = \partial_\mu - igA_\mu \tag{2.3}$$

g is the coupling of the force field A_μ with the matter field $\psi(x)$, characteristic of the force. The SM is a local invariance gauge theory with non Abelian symmetry group⁴:

$$SU(3)_C \otimes SU(2)_L \otimes U(1)_Y \tag{2.4}$$

$SU(3)_C$ is a non-Abelian group of order 3, generated by the color charge. The number of generators is eight⁵. $SU(2)_L$ is a non-Abelian group with three generators (W^1, W^2, W^3). SU2 only couples with the weak isospin I_3 , the symbol L means that SU2 acts only on left fermions. U(1) is a group with only one generator B that couples with the electric charge.

Force carriers of strong (gluons) and electromagnetic interactions (photons) are massless, as required by the gauge invariance of $SU(3)_C$ and U(1), but the weak interaction carriers are massive. In order to solve this apparent contradiction, a spontaneous symmetry breaking (SSB) of $SU(2)_L \otimes U(1)_Y$ has to be introduced to explain the origin of the weak boson masses. In the next section, the idea behind the SSB is further discussed.

⁴A group with transformation A is non-Abelian if two members (a,b) of the group have the property $aAb \neq bAa$

⁵The number of generators of a group of order n is $n^2 - 1$

2.3 The Electroweak Interaction

The weak and electromagnetic interactions are unified in the electroweak theory, referred to as the GWS-theory in honor its authors S.Glashow, S.Weinberg and A.Salam. The symmetry of the electroweak theory is the $SU(2)_L \otimes U(1)_Y$.

As previously mentioned, the $SU(2)_L$ is a non-Abelian group, with three generators W^1, W^2, W^3 that couples with the weak isospin. The left-handed fermions are doublets of weak isospin $1/2$ and $-1/2$, for example, the ν_e and the electron are members of one doublet $\psi_L^T = (\nu_e, e^-)$. All right-handed fermions are $SU(2)$ singlets ($I_3 = 0$).

The $U(1)_Y$ part of the GWS theory acts over all left and right fermions (chiral symmetry) and the gauge transformation is given by the equation 2.2. The conserved quantity, is in this case, the hypercharge Y , already defined in equation 2.1, and the gauge boson corresponds to B^0 .

The observed weak bosons W^+, W^-, Z^0 and the photons γ are mixed states of W^1, W^2, W^3 and B^0 as a consequence of the non-Abelian self coupling between bosons, of the form:

$$W^\mp = \frac{1}{\sqrt{2}}(W^1 \pm iW^2) \quad (2.5)$$

$$\begin{pmatrix} \gamma \\ Z \end{pmatrix} = \begin{pmatrix} \cos \theta_W & \sin \theta_W \\ -\sin \theta_W & \cos \theta_W \end{pmatrix} \begin{pmatrix} B^0 \\ W^3 \end{pmatrix} \quad (2.6)$$

where θ_W is referred to as the weak mixing angle. As mentioned before, the Lagrange density stays invariant after the gauge transformation if the gauge bosons are massless. The masses of the weak bosons (W^+, W^-, Z^0) are the result of the breaking of the electroweak symmetry. When the ground state of the gauge field (vacuum) is not stable, it could break the symmetry when it is chosen. This is known as the SSB. The specific way in which bosons and fermions obtain mass after the SSB (Higgs mechanism) is further clarified in the next section.

2.3.1 The Higgs Mechanism

A spontaneous symmetry breaking of the electroweak force can be studied through the introduction of a complex scalar field, shown in the equation 2.7. The Φ field is referred to as Higgs field.

$$\Phi = \begin{bmatrix} \phi^+ \\ \phi^0 \end{bmatrix} = \begin{bmatrix} (\omega_2 + i\omega_1)/2 \\ (\omega_4 + i\omega_3)/2 \end{bmatrix} \quad (2.7)$$

The ϕ^+ and ϕ^0 are two complex scalar fields that form a weak isospin doublet ($I_3 = \pm 1/2$) and carry hypercharge $Y(\phi^+) = Y(\phi^0) = -1$. The contribution of the Higgs field to the Lagrangian density can be written as:

$$\mathcal{L} = T(\Phi) - V(\Phi) \quad (2.8)$$

the potential $V(\Phi)$ is of the form:

$$V(\Phi) = \mu^2 |\Phi|^2 + \lambda |\Phi|^4 \quad (2.9)$$

As can be seen from 2.9, the potential $V(\Phi)$ vanishes if $|\Phi| = 0$. Another possibility is when $|\Phi| = \sqrt{-\mu^2/2\lambda} = \nu/\sqrt{2}$. If it is the case, the vacuum is no longer $|\Phi| = 0$ and unique but infinitely degenerate. An appropriate choice of the vacuum:

$$\Phi_{min} = \frac{1}{\sqrt{2}} \begin{bmatrix} 0 \\ \nu + h(x) \end{bmatrix} \quad (2.10)$$

breaks the symmetry, due to the selection of the particular vacuum state. $h(x)$ denotes a real observable Higgs field. Before the symmetry breaking, Ψ is written as shown in equation 2.7. When the vacuum is chosen, the symmetry is broken and three of the scalar Higgs (ω_1, ω_2 and ω_3) are absorbed for the W^1, W^2, W^3 of the $SU(2)_L$, because the Higgs fields possess weak isospin and gain mass. The $h(x)$ survives this process and should be observed as a real object, because the world in that we live in is one with broken electroweak symmetry.

A confirmation of the Higgs mechanism was obtained in the year 2012 with the discovery of a new boson particle, in the mass range of 125-126 GeV [11] [12], compatible with the SM predictions.

2.3.2 Lagrangian of the Electroweak Theory

To finalize this section, the explicit form of the electroweak Lagrangian will be given, because it will be necessary later when the self-coupling between electroweak bosons is explained. The Lagrangian can be written as follows:

$$\begin{aligned} \mathcal{L}_{EW} = & \bar{\Psi} i \gamma^\mu D_\mu \Psi - \frac{1}{4} F_{\mu\nu} F^{\mu\nu} - \frac{1}{4} B_{\mu\nu} B^{\mu\nu} \\ & + (D_\mu \Phi)^\dagger (D^\mu \Phi) - V(\Phi) - G_f [\bar{e}_R \Phi^\dagger \Psi_L + (\bar{\Psi}_L \Phi) e_R] \end{aligned} \quad (2.11)$$

The first line of equation 2.11 is known as the gauge sector and the second corresponds to the Higgs sector. It contains the Higgs potential introduced in the previous section in order to produce the SSB. The last term of the equation is referred to as the Yukawa term and is the responsible for the fermion masses. In the gauge sector, the term $\bar{\Psi} i \gamma^\mu D_\mu \Psi$ has the information about the interaction of the gauge bosons with the fermions. The terms $F_{\mu\nu}$ and $B_{\mu\nu}$ can be written as:

$$F_{\mu\nu} = \partial_\mu W_\nu - \partial_\nu W_\mu - g_W W_\mu W_\nu \quad (2.12)$$

$$B_{\mu\nu} = \partial_\mu B_\nu - \partial_\nu B_\mu \quad (2.13)$$

the above formula shows terms that correspond to the kinetic energy part of the gauge bosons W^1, W^2, W^3 and B^0 , previously introduced. An important characteristic visible here is the existence of the quadratic term $g_W W_\mu W_\nu$, which represents the self interaction of the gauge boson and is the responsible for the triple and quartic self coupling between the electroweak bosons. A detailed description of the self boson coupling will be given later, when the ZZ production is discussed.

2.4 Quantum Chromodynamics (QCD)

As it was already mentioned, the list of the fundamental constituents of matter change depending on the experimental possibilities. Protons and neutrons were considered the building blocks of matter for many years, but scattering experiments with high energetic electrons showed their inner structure; which consist of the called partons. Besides the experimental ability, the characteristics of the interaction between partons in protons and neutrons namely strong interaction, made the study of this force and its effects complicated.

Today, the strong interaction uses the mathematical framework of the field theory and it is referred to as QCD. The partons are now divided in gluons and quarks, with an inner degree of freedom known as color charge. There are three kinds of color charges: i.e., R, G, B, and a total of eight gluons and six quarks. As shown before, the color charge is the generator of a $SU(3)$ non-Abelian group. In order to understand some of the special properties of the strong interaction, the QCD Lagrangian can be explicitly written as:

$$\mathcal{L}_{QCD} = -\frac{1}{4} G_a^{\mu\nu} G_{\mu\nu}^a + \sum_f \bar{q}_f (i\gamma^\mu D_\mu - m_f) q_f \quad (2.14)$$

with

$$G_a^{\mu\nu} = \partial^\mu G_a^\nu - \partial^\nu G_a^\mu + g_s f^{abc} G_b^\mu G_c^\nu \quad (2.15)$$

the G_b^ν represents the gluon fields and g_s is the coupling constant of the strong interaction. The term $g_s f^{abc} G_b^\mu G_c^\nu$ corresponds to the self-interaction between gluons; it is a result of the non-Abelian nature of the group and it explains some features of the strong interaction like the dependency of the coupling constant with the energy (running coupling constant) and the confinement of partons in hadrons.

2.4.1 Running Coupling Constant

The behavior of the coupling constant of the strong interaction α shows a dependency on the energy. When the transferred momentum in strong interactions (Q) is lower than 1 GeV α , is sufficiently big enough to avoid a perturbative treatment of the theory. However, $\lim_{Q \rightarrow \infty} \alpha(Q^2) = 0$, this is called asymptotic freedom.

The coupling constant can be explicitly written as:

$$\alpha(Q^2) = \frac{\alpha_s(\mu^2)}{1 + \frac{\alpha_s(\mu^2)}{4\pi} (11 - \frac{2}{3}n_f) \ln \frac{Q^2}{\mu^2}} \quad (2.16)$$

where $\alpha_s(\mu^2)$ is the value of the strong coupling constant measured at a convenient energy μ . μ is then referred to as a renormalization scale μ_R .

The dependency of α_s on the energy is a result of the self interaction of gluons, discussed above. In strong processes, gluons are not only exchanged between quarks, but are sources of new gluons. This process increases the value of the color charge seen for an external particle.

Quarks and gluons are limited to distances lower than 1 fm. This characteristic is commonly known as confinement and it is a consequence of the dependency of α_s on the energy. For Q lower than approx. 200 MeV, the value of the coupling-constant is high enough to produce new quarks and gluons from the potential.

Confinement and asymptotic freedom play important effects on the collision of hadrons. A detailed discussion of the proton-proton interaction is given below.

2.5 Proton-Proton Interaction

At hadron colliders with high momentum transfer ($Q > 1$ GeV), it is expected to have hard collisions between the individual quarks confined in the hadrons, this is a direct consequence of the asymptotic freedom explained before. Besides the hard collision, low energy (large range) interactions between the rest of the quarks in the hadrons happen via the exchange of gluons, which in between emit gluon-gluon pairs that interact further. The result is the production of hadrons, so the colorless balance of the system is maintained; this process is referred to as hadronization. The produced hadrons are highly collimated and are collectively known as a jet.

The evidence of the inner structure of the protons was obtained in experiments of deep inelastic scattering (DIS) of energetic leptons for nucleons. The leptons are able to see the inner momentum distribution of the quarks inside the hadron, usually referred to as the parton density functions (PDF). With more momentum transferred, the PDF have contributions of other QCD processes, like gluon-gluon production.

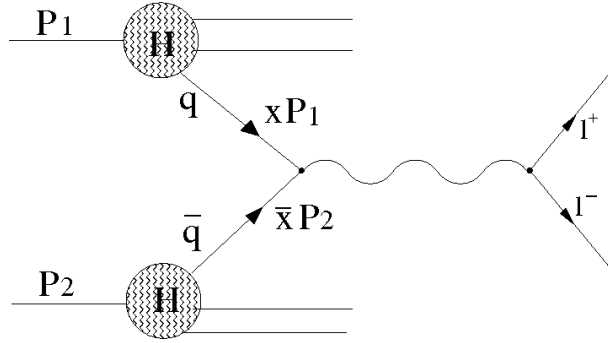


Figure 2.1: Example of a proton-proton interaction. A hard collision between a sea quark and a valence quark with a leptonic final state is shown.

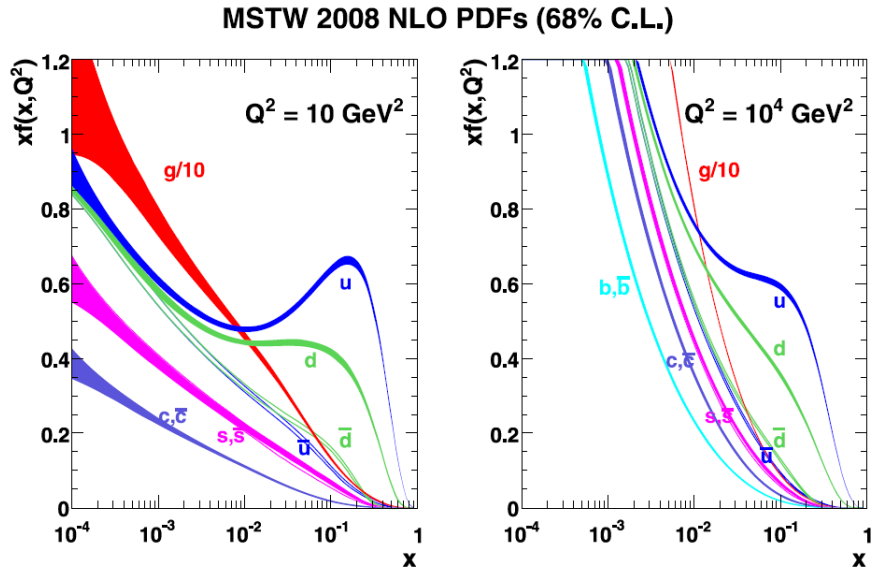


Figure 2.2: Example of a PDF distribution as function of the transfer momentum. Left side of the figure shows the effect of the use of a scale $Q^2 = 10 \text{ GeV}^2$. Right side shows the PDF at a scale $Q^2 = 10^4 \text{ GeV}^2$. Plot taken from [15]

In that way, the DIS can be considered as a hard process, where the probe particle interacts with an almost free parton and one low energy (long range interaction) contribution that affects the measurable parton distribution. The hard interaction is treated using perturbation theory and the QCD corrections are folded in the PDF functions. This separation is the so called factorization and allows precise QCD predictions in spite of the complexity of the strong interaction. The separation between the short and long range interaction is determined through an arbitrary variable factorization scale μ_F .

The simple picture of a proton or neutron composed of point particles is more complex when the energy used to probe the parton is sufficiently high. For example, apart from the two up quarks and the down one that build the proton, there are manifold quarks and antiquarks as a

result of the gluon-gluon interaction. These quarks are called sea quarks meanwhile the two up and the down one are referred to as valence quarks.

In figure 2.2, the distribution of the MSTW PDF is shown. The fraction of transferred momentum (x) times the PDF as function of the transferred momentum (x), is shown for two different scales of the total momentum transferred Q^2 . At high values of x , the major contributions to the PDF are coming from up and down quarks, that is valence quarks. At low values of x , contributions of other quarks (seaquarks) are more important. For the higher scale, this contributions of sea quarks are more important because the gluon splitting can be resolved.

The probability for a parton to emit a parton or to undergo a splitting is described by the Altarelli-Parisi splitting functions. For example, the probability of a quark to emit a gluon with a momentum fraction $1-x$ is:

$$P_{qg} = \frac{4}{3} \frac{1+x^2}{1-x} \quad (2.17)$$

A representation of the interaction between two protons can be seen in figure 2.1. A valence quark of one proton collides with a sea antiquark of the second proton. Quark and antiquark have a fraction x and \bar{x} of the initial momentum P_1 and P_2 of the protons. As a result of this hard interaction a new particle is produced which later decays (shown in figure marked as l^+ , and l^- ,) into a pair of leptons.

The cross section of the process ($\sigma(pp \rightarrow X)$) can be written as shown in equation 2.18.

$$\sigma(pp \rightarrow X) = \sum_{1,2} \int_0^1 dx_1 \int_0^1 dx_2 f_1(x_1, \mu_F^2) f_2(x_2, \mu_F^2) M(x_1, x_2, s, \mu_F^2, \mu_R^2) \quad (2.18)$$

In equation 2.18, x_1 and x_2 correspond to the incoming partons 1 and 2. f_1 and f_2 are the PDFs for each parton depending on the already introduced factorization scale μ_F . M represents the partonic matrix element, depending on the factorization μ_F and renormalization scales μ_R .

2.6 Production of Dibosons

As mentioned in section 2.3.2, the electroweak Lagrangian makes precise predictions of the weak gauge boson interaction with fermions and values of the self interactions. Collision experiments conducted at the end of the 20th century gave precise values for the boson-fermions coupling compatible with SM expectations. The bosons self-couplings was measured in those experiments as well, but, with the development of the proton-proton collider at CERN, a new interest in the measurement of these couplings at TeV scales was awoken. In this work, a special attention is given to the production of two neutral bosons.

In the following section, a description of the production of ZZ via a triple gauge bosons vertex (TGC) is given. Later, the production mechanism of Z pairs in the LHC and some

previous results are discussed. At the end of the section, an explanation of the anomalous TGCs and their physical implication is given.

2.6.1 Triple Gauge Coupling

One consequence of the non-Abelian structure of the SM is the existence of triple and quadric self-couplings between gauge bosons. The general expression is condensed in equation 2.13.

A general picture of the triple gauge coupling (TGC) is shown in figure 2.3.

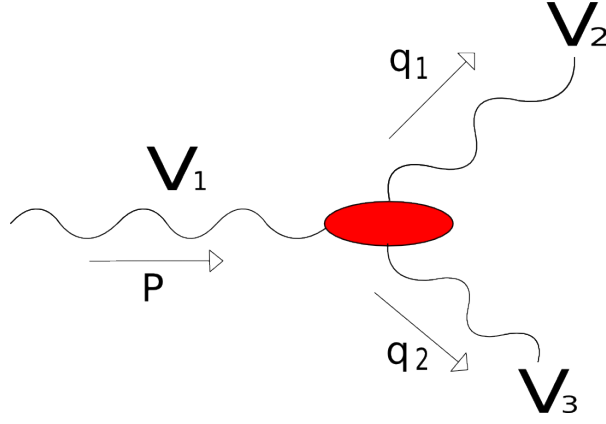


Figure 2.3: Representation of the TGCs. An incoming vector boson V_1 with momentum P meets two outgoing vector bosons: V_2 and V_3 with momenta q_1 and q_2 , respectively.

In the SM V_3 and V_2 have to be different bosons. That means charged vertices are allowed; e.g., W^+W^-Z/γ , $W^+Z/\gamma W^+$, but TGCs that involve three neutral bosons (ZZZ or $ZZ\gamma$) are forbidden in the SM.

The vertex function shown in figure 2.3 can be parametrized as:

$$\begin{aligned}
 \Gamma_V^{\alpha\beta\mu} = & f_1^V (q - \bar{q})^\mu g^{\alpha\beta} - \frac{f_2^V}{M_W^2} (q - \bar{q})^\mu P^\alpha P^\beta + f_3^V (P^\alpha g^{\mu\beta} - P^\beta g^{\mu\alpha}) \\
 & + i f_4^V (P^\alpha g^{\mu\beta} + P^\beta g^{\mu\alpha}) + i f_5^V \epsilon^{\mu\alpha\beta\rho} (q - \bar{q})_\rho \\
 & - f_6^V \epsilon^{\mu\alpha\beta\rho} P_\rho - \frac{f_7^V}{M_W^2} (q - \bar{q})^\mu \epsilon^{\alpha\beta\rho\sigma} P_\rho (q - \bar{q})_\sigma
 \end{aligned} \tag{2.19}$$

where P , q and \bar{q} are the four-momenta of V_1 , V_2 and V_3 , respectively. The coefficients f_i^V are form factors that depend on P^2 . The form factors have information of the nature of the interacting particles.

For example, the first line in equation 2.19 is related to the dipolar and quadrupolar moment of charged bosons. The complex functions f_4^V and f_5^V are called neutral triple gauge couplings and are functions of q_1 and q_2 and P , as shown in figure 2.3.

The Lagrangian generator of the function vertex shown in figure 2.3 in the case of neutral bosons is: $Z_1 Z_2 V$ with Z_1 and Z_2 on-shell and $V = Z, \gamma$ in general off-shell, can be written as [16] [17] [18]:

$$\mathcal{L} = \frac{e}{m_Z} [f_4^V (\partial_\mu V^{\mu\beta}) Z_\alpha (\partial^\alpha Z_\beta) + f_5^V (\partial^\sigma V_{\sigma\mu} \tilde{Z}^{\mu\beta} Z_\beta)] \quad (2.20)$$

where $Z^{\mu\beta}$ and $V^{\mu\beta}$ are the vector boson tensors and $\tilde{Z}^{\mu\beta} = \frac{1}{2} \epsilon_{\mu\nu\rho\sigma} Z^{\rho\sigma}$. f_4^γ and f_4^Z are CP violating. f_5^γ and f_5^Z couplings conserve CP, but violate parity, P [17].

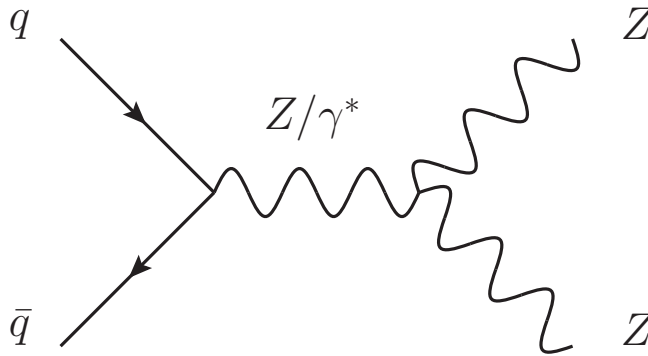


Figure 2.4: ZZ production through triple gauge couplings.

In the SM, the values for the triple gauge couplings are predicted to be zero at tree level. For that reason, the ZZ production through the s-channel shown in figure 2.4 does not exist. Contributions at next orders can be introduced and parametrized. If any deviation to the SM values of the TGCs is found, it constitutes a proof of the limits of the SM. In the next section, anomalous values of the TGC are discussed.

2.6.2 Anomalous Neutral Triple Couplings (aTGC)

Values different from zero for the triple gauge couplings, referred to as anomalous TGCs couplings (aTGCs), would produce extra terms in the effective Lagrangian shown in equation 2.11. As a result of these terms, an enhancement of the ZZ production cross section at high values of p_T is expected. As an example, in figure 2.5, the p_T of the Z with the larger transverse momentum of the ZZ system is shown, it was measured in the ATLAS experiment at center of mass energy of $\sqrt{s} = 7$ TeV corresponding to an integrated luminosity of 4.6 fb^{-1} .

The background expectation and the measured data are compared with predictions of different values of the neutral triple gauge couplings, shown as dashed lines. The aTGCs curves correspond to simulations at different values of the triple gauge couplings, f_4^γ , f_4^Z , f_5^γ and f_5^Z . As already mentioned, an increase in the number of events at high values of p_T is expected if the aTGCs values are different of zero.

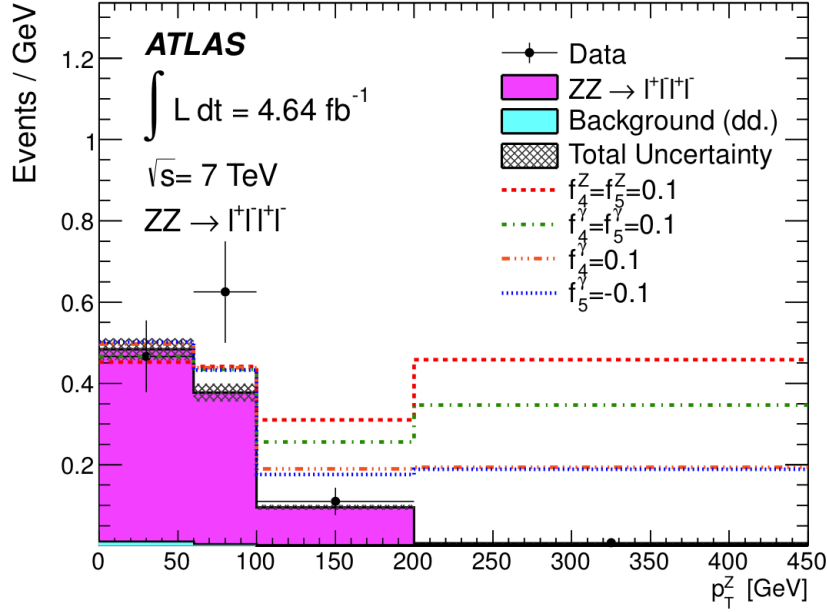


Figure 2.5: In figure $Z p_T$ distribution measured in ATLAS with a center of mass energy of $\sqrt{s} = 7$ TeV, corresponding to an integrated luminosity of 4.6 fb^{-1} compared with simulations of anomalous neutral triple gauge couplings at values different from zero. Figure taken from [19].

In order to study aTGCs, form factors $f_i^V(s)$ depending on the partonic center of mass energy (\sqrt{s}) are introduced:

$$f_i^V(s) = \frac{f_{i0}^V}{\left(1 + \frac{s}{\Lambda_{FF}^2}\right)^n} \quad (2.21)$$

where $i = 4, 5$, n is a constant and Λ_{FF} is a cutoff related to the scale of new physics generating the anomalous TGCs. The dependency with s in equation 2.21 is introduced to avoid possible violation of the partial-wave unitarity, due to the rapid growing of the SM deviation with the partonic center of mass energy [16] [17] [18].

The effects of the four triple gauge couplings; f_4^γ , f_4^Z , f_5^γ and f_5^Z , on the ZZ production cross section can be directly determined through observation of deviations on the expected number of produced bosons compared with the SM predictions. If any significant deviation is observed, limits on the values of the aTGCs can be calculated.

The basic assumption on the study of the aTGCs is that new physics exist at one scale Λ_{FF} , far beyond the reach of current experiments. New particles due to these physics are directly observable, but the effects of these can be seen as anomalous interactions of the SM particles. A simple method to generate aTGCs is through virtual effects at loop level [16] [17] [18]. New heavy fermions arising from a fourth generation of fermions can produce this vertex correction.

Limits to the anomalous triple gauge coupling have been derived using collision data. Table

2.2 shows the one dimensional 95% confidence level intervals for anomalous neutral gauge boson couplings derived for the ATLAS experiment, at a center of mass energy of $\sqrt{s} = 7$ TeV, corresponding to an integrated luminosity of 4.6 fb^{-1} .

Λ_{FF}	f_4^γ	f_4^Z	f_5^γ	f_5^Z
3 TeV	[-0.022,0.023]	[-0.019,0.019]	[-0.023,0.023]	[-0.020,0.019]
∞	[-0.015,0.015]	[-0.013,0.013]	[-0.016,0.015]	[-0.013,0.013]

Table 2.2: One dimensional 95% confidence intervals for aTGCs derived from ATLAS data at $\sqrt{s} = 7$ TeV. Limits are presented for $\Lambda_{FF} = 3$ TeV and $\Lambda_{FF} = \infty$, both include the total systematic. [19].

In the table shown above, limits for two Λ_{FF} values are given. The 3 TeV value is used to avoid the partial-wave unitarity violation at the LHC energy. The limits with any form factor (i.e. $\Lambda_{FF} = \infty$) are used in order to make a comparison with other experiments, with different energy conditions. The extraction of the confident limits is based on the comparison of the measured and expected number of events in variables like the p_T of the most energetic Z or the invariant mass of the ZZ , because these variables are very sensitive to the anomalous couplings. Then, the couplings are parametrized as a function of the observed yield. A detail description of the extraction procedure is given in chapter 7.

2.6.3 Diboson Searches at LEP and Tevatron

At the end of the 20th century, a series of experimental efforts were done in order to test the predictions of the SM. The Z boson discovery and precision measurement of the mass of the Z and the couplings with fermions, were done in experiments like the Large Electron-Positron collider (LEP) at CERN, and hadron colliders like the Tevatron in the Fermi National Accelerator Laboratory (Fermilab) in USA.

ZZ production was studied at LEP by the L3 [20], OPAL [21], ALEPH and DELPHI [22] collaboration in multiple final states. At an energy of $\sqrt{s} = 200$ GeV in e^+e^- collisions, a combined cross section $\sigma(e^+e^- \rightarrow ZZ) = 0.90 \pm 0.12$ pb was measured.

The Tevatron experiments, $D\bar{O}$ [23] [24] [25] and CDF [26], looked for Z pair production using proton-antiproton beams at an energy of $\sqrt{s} = 1.96$ TeV. CDF, using a total integrated luminosity of 1.9 fb^{-1} has observed three ZZ events in the channels $ZZ \rightarrow llll$ and $ZZ \rightarrow ll\nu\bar{\nu}$ ($l = e, \mu$) [26]. $D\bar{O}$ with 1.7 fb^{-1} of data, reported the observation of three events in the $ZZ \rightarrow llll$ channel [23].

CDF and $D\bar{O}$ measured a cross section of $\sigma = 1.4^{+0.7}_{-0.6}$ pb and $\sigma = 1.60 \pm 0.63$ (stat) $^{+0.16}_{-0.17}$ (sys.) pb. CDF has made an update of the ZZ analysis to an integrated luminosity of 4.8 fb^{-1} , reporting the observation of five events in the $ZZ \rightarrow llll$ channel [25].

Most recently, the two experiments of the LHC, ATLAS and CMS, using proton-proton

collisions, have released results of ZZ production with 5 fb^{-1} data at an energy of $\sqrt{s} = 7 \text{ TeV}$. A detail discussion of the ZZ studies using hadron colliders is shown below.

2.6.4 Diboson Physics at the LHC

The study of the production of pairs of Z bosons, as already mentioned, is important to test the electroweak sector of the SM. With the operation of the LHC at center of mass energy in the order of ten TeV, a new opportunity is obtained to test the SM at higher energy scales compared with those accessible with previous experiments like LEP or Tevatron.

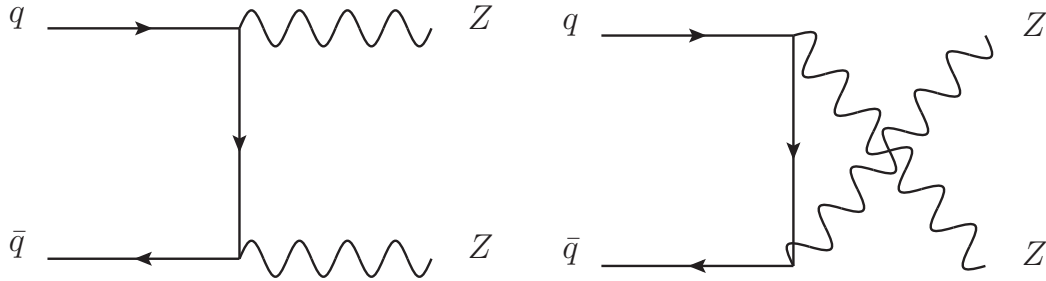


Figure 2.6: Feynmann diagrams of the ZZ production via quark-antiquark interaction.

At hadron colliders, $q\bar{q} \rightarrow ZZ$ production proceeds at the tree level, principally via quark-antiquark annihilation. The Feynman diagrams for this production mode are shown in figure 2.6 and correspond to the t- and u-channel; the s-channel involves the TGC shown in 2.4, which, as already mentioned, does not exist in the SM.

One additional production mode corresponds to the gluon-gluon fusion shown in figure 2.7. The contribution of gluon-gluon fusion to the ZZ production is about 6%, so the quark-antiquark interaction is the dominant mechanism of dibosons production in hadron colliders.

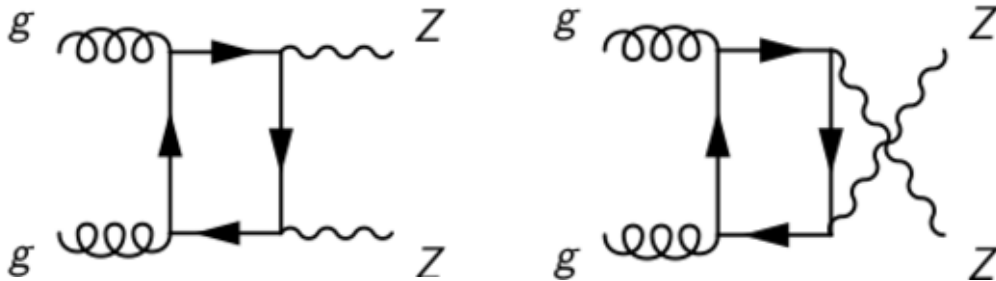


Figure 2.7: Feynmann diagrams of the ZZ production via gluon-gluon fusion.

Each Z boson produced via any of the referred mechanisms can decay into different particles with a determined probability. For example: quark-antiquark (70%), neutrino antineutrino (20%) and oppositely charged leptons (10%). In this work, the $ZZ \rightarrow e^+e^-e^+e^-$ channel is

studied. The corresponding branching ratio for this decay mode is [13]:

$$BR(ZZ \rightarrow e^+e^-e^+e^-) = (0.03363)^2 = 0.001 \quad (2.22)$$

Different kinds of processes can show similar final signatures as those of dibosons. Figure 2.8 shows processes with final real Z and a variable number of jets, which can fake the signal of leptons in the detectors. On the left side of figure 2.8, a Z boson and a gluon are produced. The gluon will produce new hadrons, due to the nature of the strong interaction; and the new hadrons are measured as jets in the detector. The middle and right side of the figure show the Z production with b-quarks. The b-quarks also form jets after hadronization.

Additionally to this sources of background, $t\bar{t}$ production, as shown in figure 2.9, can produce leptonic and jet final states that contribute with the background of the diboson production. In this case, the high mass of the top-quark allows the production of heaviest particles like W bosons, which can produce leptons in final states.

Contribution of the mentioned process, with jet contents, can be reduced experimentally, using tighter selection criteria on the identification of the leptons. Process with four final real leptons, like those shown in figure 2.10 cannot be reduced experimentally. One example is the right side of figure 2.10, which represents the production of a Higgs boson via Vector Boson Fusion (VBF). The produced Higgs decay into a ZZ^* and, additionally, two jets with high values of the pseudorapidity are produced.

The expected number of ZZ and background events of each kind can be determined for a specific luminosity with the help of Monte Carlo (MC) simulations. In the next section, a brief description of the MC generators used in this analysis is given.

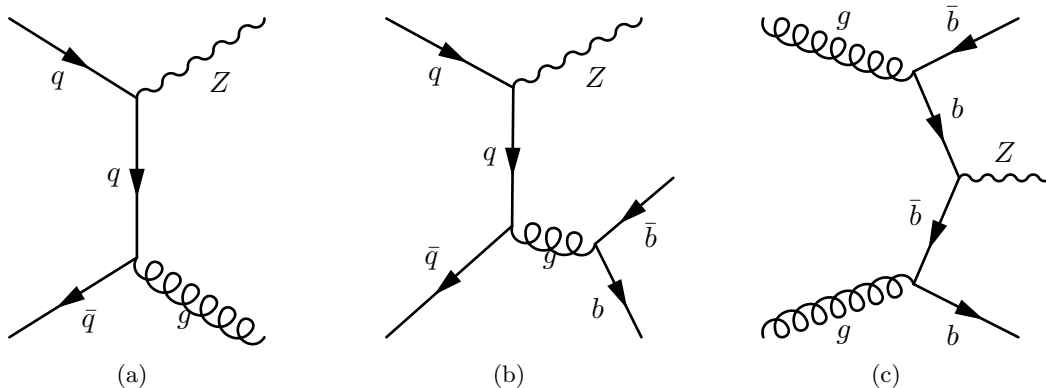


Figure 2.8: Example of Z production plus gluons (a) and quarks ((b) and (c)).

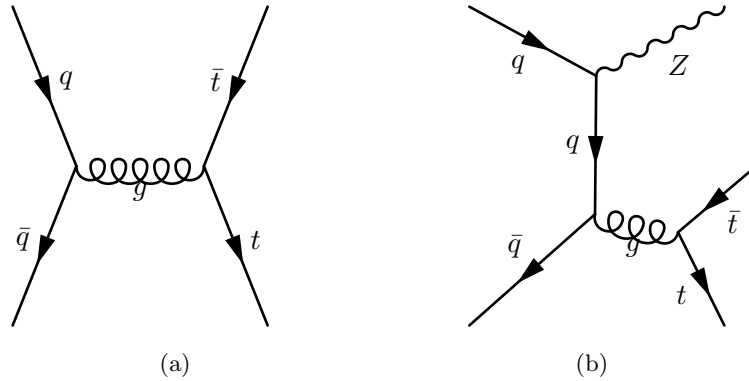


Figure 2.9: $t\bar{t}$ production with an associate Z boson.

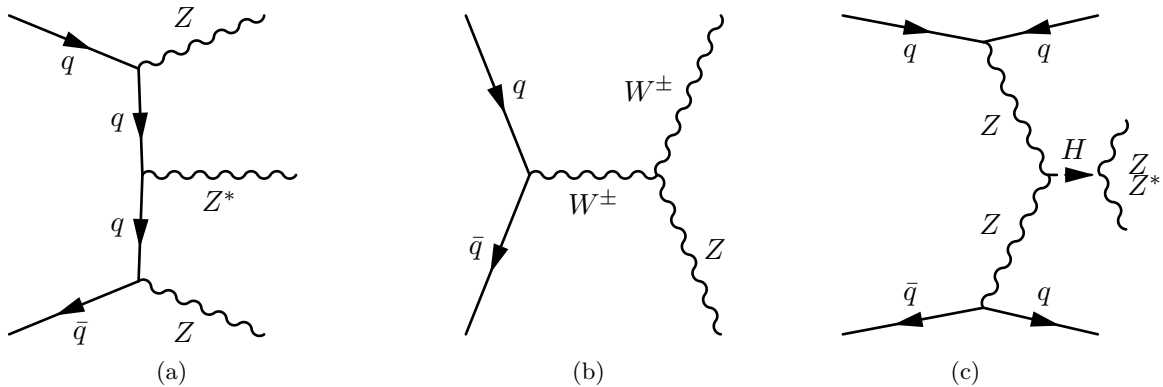


Figure 2.10: Processes with final experimental signatures similar to the ZZ production. (a) ZZZ^* process, (b) ZWW and (d) Higgs production via vector boson fusion.

2.7 PDFs and Monte Carlo (MC) Generators

As already mentioned in section 2.5, the characteristics of the QCD interaction force to consider protons as non-elementary particles but as a compost of quarks and gluons carrying the fraction momentum of the proton. The momentum distributions (PDFs) can be measured in collision experiments and the universality of the QCD allowed to apply the PDFs to the study of other phenomena.

The most common method used to study physics process is the generation of simulations that reproduce the expected behavior of the process. The four vectors of the particles involved in the initial process are generated following a density distribution. The density distribution in this case corresponds to the PDF used in the generator convolved with the matrix element

governing the process already introduced in equation 2.18.

The PDFs are necessary to calculate the cross section, for example, using the equation 2.18. The degree of the perturbation approximation, e.g., Leading Order (LO), Next to Leading Order (NLO), depends on the PDFs.

The most commonly set of PDFs used are:

1. **CT10** [27]: A NLO PDFs set based in a heavy-quark mass implementation in perturbative QCD cross sections. It includes data of Deep Inelastic Scattering from HERA-I, vector boson production and single-inclusive jet production from Tevatron measurements.
2. **MSTW2008** [28]: It includes LO, NLO and NNLO PDFs sets. The fits include a large amount of data from HERA and Tevatron Run II. It improves the uncertainty propagation of the data to the fits in comparison with previous PDFs that used similar perturbative schema.

The different set of PDFs listed above are generally included in MC generators that are able to simulate physics processes, at order depending on the PDF. The matrix elements, that simulate the hard interaction process are calculated for the generator and predictions on the cross sections are given.

Kinematic distributions can be produced, too, with the help of MC generators. These simulated distributions are known as generator level distributions. Different kinds of generators exist; those used in this analysis to estimate the signal and background contributions are listed below.

1. **PowhegPythia** [29]: It is a NLO generator used in this analysis to simulate the MC signal via quark-antiquark interaction. It includes fermionic decays of the ZZ and $Z(\gamma^*)$ interference terms.
2. **ggVV** [30]: this generator is used to complement the **PowhegPythia** signal prediction because it includes the full $gg \rightarrow (Z\gamma^*)(Z\gamma^*) \rightarrow \ell^+\ell^-\ell^+\ell^-$
3. **MC@NLO** [31]: Its a NLO event generator, which calculates the matrix elements with additional single particle corrections to the hard process. In this piece of research is used for the generation of $t\bar{t}$ background samples.
4. **MadGraph** [32]: It is a tool to automatically generate matrix elements used principally to obtain prediction of rare and new physics processes. In this work, some of the background processes are simulated using this generator.
5. **ALPGEN** [33]: It is a LO generator designed for the study of multiparton hard processes in hadronic collisions. Predictions of anomalous triple gauge couplings can be made with **ALPGEN**.

6. **MCFM** [34]: It is a parton level MC program used to obtain the cross sections of various femtobarn level processes in hadron-hadron colliders at Next to Leading Order. With help of this program, a theoretical prediction of the ZZ cross section at $\sqrt{s} = 8$ TeV will be given.

An important aspect of the experimental physics is the modeling of detector response to the experimental conditions. A powerful tool designed to achieve this task is the simulation toolkit **GEANT4** [35]. The toolkit provides a series of components to simulate all aspects of the experimental setup. The geometry of the systems, materials involved, fundamental particles of interest and the interaction of the particles with the matter and electromagnetic fields can be implemented in the simulation. As already discussed in this section, MC distributions at generator level are produced using Monte Carlo methods. Further interactions of the produced particles with the matter are tracked through the different geometric domains of the detector with a detail model of **ATLAS** implemented using **GEANT4**. A collection of hits in sensitive areas of the detector are formed, and later, a simulation of the response of the electronic is conducted (digitalization). In that way, a full simulation of the response of the detector is obtained to be compared with real data.

2.8 ZZ Cross Section Prediction

In order to have an idea of the expected number of ZZ events at a particular center of mass energy, the cross section of the process must be determined. In this work, **MCFM** samples were used to calculate the theoretical total cross section of the ZZ . Scale variations and uncertainties in the PDF were considered and are quoted as the uncertainty in the total cross section shown below. The total production cross section of the ZZ ($\sigma_{ZZ}^{total}(pp \rightarrow ZZ + X)$) is [34]:

$$\sigma_{ZZ}^{total}(pp \rightarrow ZZ + X) = 7.2^{+0.3}_{-0.2} \text{ pb} \quad (2.23)$$

Chapter 3

The ATLAS Experiment

Announcer: It's a dead heat! They're checking the electron microscope.

And the winner is... Number three in a quantum finish!

Professor Farnsworth: Not fair! You changed the outcome by measuring it!

—Futurama

Collision experiments have been used in the past to study matter and the interactions governing the particle dynamics. One of the nowadays operating colliders is the Large Hadron Collider (LHC) a circular accelerator placed in the ancient facilities of the LEP-Experiment¹. Protons are accelerated in the LHC, which was designed with four places where the accelerated protons can collide². In each point, a detector was built, where the products of the collision could be measured. ATLAS³ is one of these detectors.

Like other LHC detectors, ATLAS consists of a set of subsystems with specific characteristics, able to work in an environment of high energy and particles density. The subsystems are designed to make precise measurements of energy, momentum and tracks of the products of the proton-proton collisions. In this chapter, the characteristics of ATLAS and the different subsystems belonging to it are described.

3.1 The Large Hadron Collider

The LHC is located at the common border of France and Switzerland. The design center of mass energy is 14 TeV with an instantaneous luminosity of $10^{34} \text{ cm}^{-2} \text{ s}^{-1}$; these characteristics make the LHC one of the most prominent tools to do searches in today's experimental particle physics.

¹Large Electron-Positron Collider

²The physics program of the LHC include the collision of lead nuclei.

³A Toroidal LHC Apparatus

The accelerating complex of the CERN research center sets the infrastructure for different experiments. The ring of the LHC is around 26.7 km long and is located 100 meter under the floor level. Figure 3.1 shows the position of the LHC detectors.

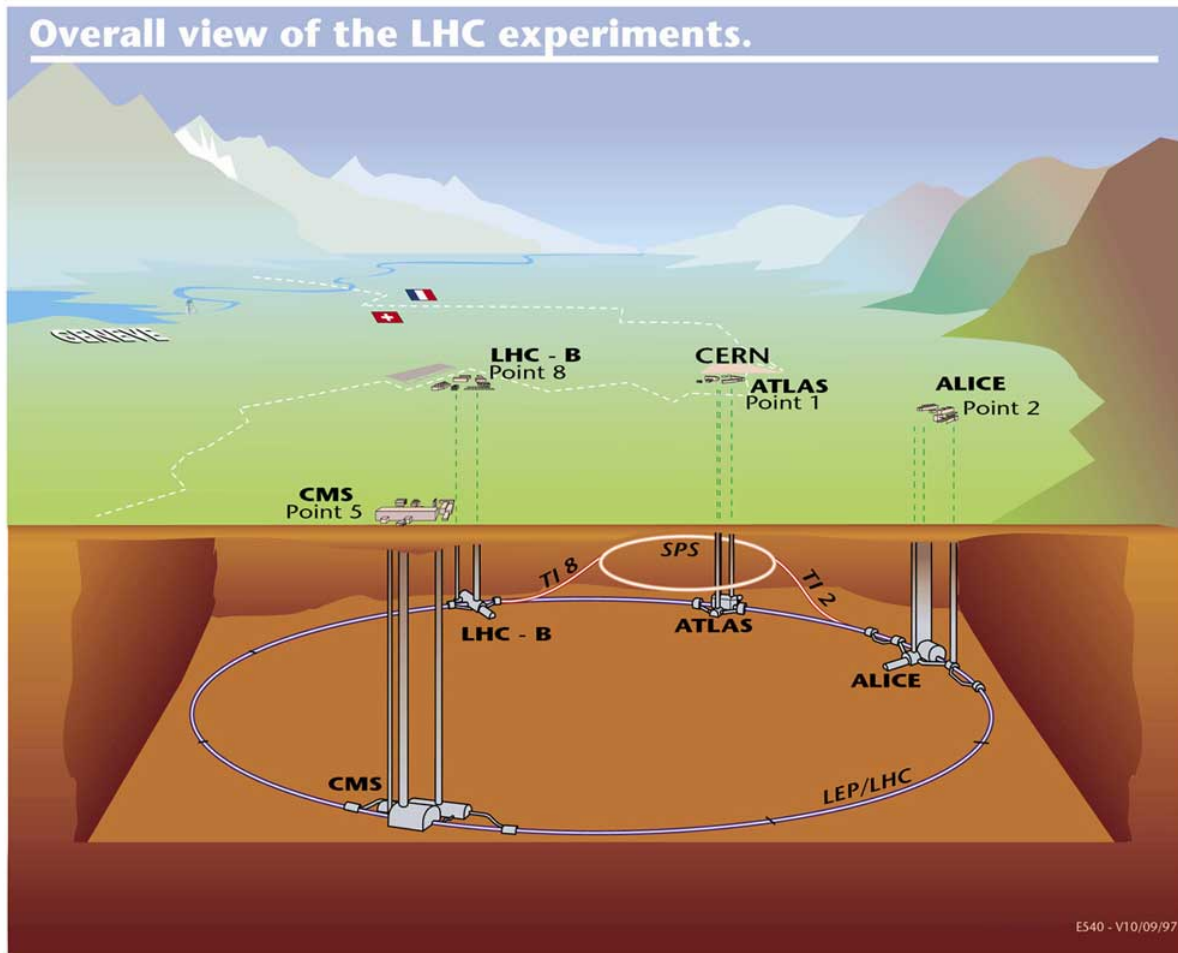


Figure 3.1: Localization of the LHC experiments. Image taken from [36].

Protons are obtained in the LHC through ionization of hydrogen. The produced protons are accelerated in successive steps, first with the help of a linear accelerator (LINAC2), then using two synchrotrons (SP and SPS). The protons are later injected into the main storage ring. ATLAS and CMS⁴ are general detectors, made for the search of new physics in proton-proton collisions. The other two detectors LHCb and ALICE are designed to look for specific physics processes with protons and heavy ions, respectively.

The accelerated protons are injected into the storage ring in bunches which collide in four intersection points where the detectors are placed. The number of particles in the bunch and the frequency of bunch collision define the instantaneous luminosity.

⁴Compact Muon Solenoid

The physics program of the LHC started in the year 2009. At the beginning, the collisions were done at a center of mass energy of 900 GeV. In 2010, the energy was increased to $\sqrt{s} = 7$ TeV. The data analyzed in the present work was obtained in 2012 and first half of 2013, at a center of mass energy of $\sqrt{s} = 8$ TeV that corresponds to an integrated luminosity of approx. 20.3 fb^{-1} .

The products of the collisions in the detectors are first analyzed using a trigger system, in order to reduce the size of the data to be stored. Only events possessing objects that fulfill an appropriate set of thresholds in some variables are recorded. The events are grouped in so called runs, depending on operational conditions. The runs are further grouped in periods, separated by time intervals that are used to make detector adjustments or to probe and change beam conditions, e.g., the spacing between bunches.

3.2 The ATLAS Detector

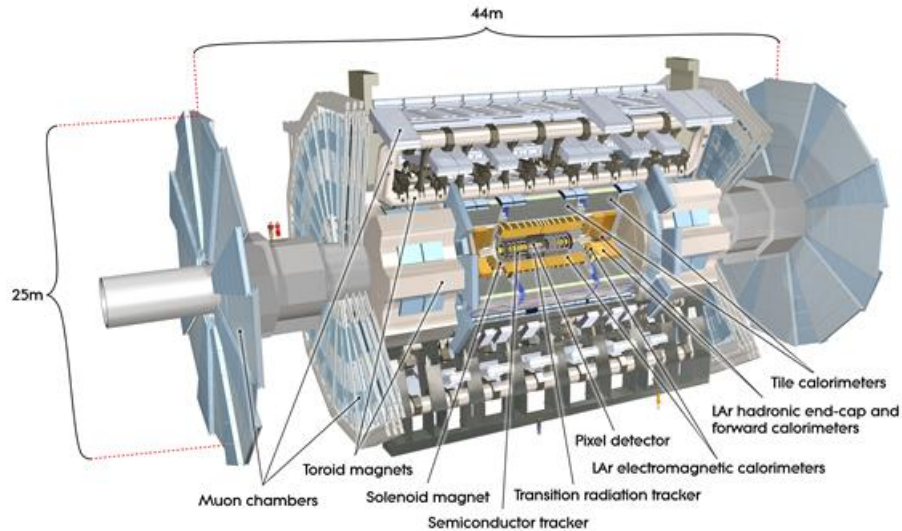


Figure 3.2: A schematic view of the ATLAS detector with the main subdetectors labeled. The dimensions of the detector are quoted, too [37].

The biggest of the four detectors located in the main ring of the LHC is the ATLAS detector. Due to the symmetry of the collision process, it was designed with a cylindrical form with a total length of 44 m and a diameter of 25 m [37]. Figure 3.2, shows a drawing of ATLAS. Protons collide at the center of the detector and the products of the collisions fly through the subdetectors that are placed at concentric layers. The innermost subdetector is responsible for the measurement of tracks of charged particles. This subsystem is called inner detector and is immersed in a solenoidal magnetic field of 2 Tesla. Radially outside the inner detector is the

calorimeter system, which is necessary for the measurement of the energy of collision products. The outermost device is the Muon Spectrometer, designed to detect the heavy brother of the electron. The muon spectrometer is immersed in a toroidal magnetic field. In between each subsystem are all the necessary elements to facilitate the functioning of the subdetector, e.g, cables and cryogenic systems.

The protons collide in the center of ATLAS, referred to as interaction point (IP). The IP is taken as the origin of a coordinate system in which the xy -plane is perpendicular to the beam pipe. The x -axis is defined by pointing to the center of the ring and the y -axis by pointing to the earth ground. A spherical coordinate system can be used, too. The azimuthal angle ϕ is placed in the previous defined xy -plane, with values from 0 to 2π . The polar angle θ is measured relatively to the direction of the beam pipe.

The pseudorapidity η is used more often than θ because the number of produced particles in one collision per pseudorapidity interval is constant. The pseudorapidity is related to the polar angle, as shown in the equation below.

$$\eta = -\ln\left(\tan\frac{\theta}{2}\right) \quad (3.1)$$

As function of η , three regions can be categorized. One central region (barrel), one endcap and one forward region⁵.

In ATLAS, the inner detector has a coverage until $|\eta| = 2.5$. The muon momentum can be measured until $|\eta| = 2.7$ and the calorimeters systems until $|\eta| = 4.9$ [37]. The inner detector can measure particle tracks with transverse momentum larger than 0.5 GeV in a pseudorapidity interval given by $|\eta| < 2.5$ [37].

3.2.1 Inner Detector

After the collision of the protons in the IP, the produced particles travel through the inner detector. If the particles are charged, the path is determined in the inner detector, which is able to find the origin of the produced particle (vertex).

The inner detector is one 6.2 m long cylinder with a radius of 1.05 m. One superconducting solenoid produces a magnetic field with a strength of 2 T, used to bend the track of the charged particles in order to measure the momentum of the particles. The inner detector was designed to measure the transverse momentum with a resolution of $\sigma_{p_T}/p_T = 0.05\%$

Figure 3.3 offers a sectional view of the inner detector which allows to see the three components that form the inner detector: e.g, Pixel detector, SemiConductor Tracker and the Transition Radiation Tracker. A detailed description of the inner detector components follows below.

⁵In this work the interval $2.5 < |\eta| < 4.9$ is referred to as forward region

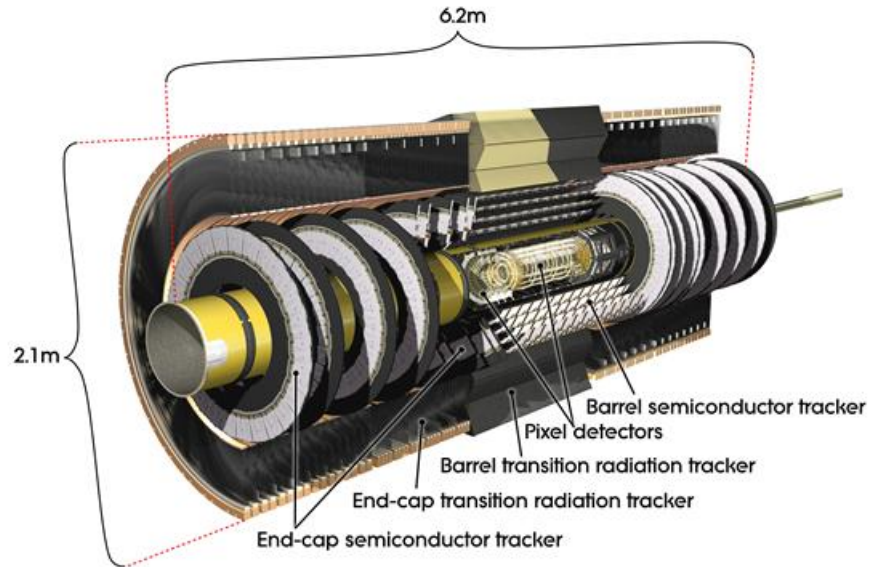


Figure 3.3: Sectional view of the inner detector. The pixel and semiconductor tracker in the barrel and endcaps are shown [37].

3.2.2 Pixel Detector

The pixel detector is the innermost detector of the ATLAS experiment. Using silicon sensors, it provides three measurement points for particles emerging from the beam pipe. The information collected by the electronics of the pixel detector allows the tracks reconstruction of charged particles and the determination of secondary vertex with high precision.

The single hit resolution of the pixel detector is $10 \mu\text{m}$ in the transverse direction and $100 \mu\text{m}$ in the longitudinal plane. The pixel detector has a transverse impact parameter resolution of the order of $15 \mu\text{m}$ and is able to measure the longitudinal primary vertex with a resolution better than 1 mm [38].

The detectors structure follows the same configuration as other components of ATLAS. Three concentric cylinders in the central region and three layers in the endcaps, perpendiculars to the beam pipe. The coverage in η is $|\eta| < 2.5$, including the central region and the endcaps.

A sectional view of the barrel part of the inner detector is visible in figure 3.4. The pixel detector corresponds to the structures at the bottom part of the figure, closer to the beam pipe.

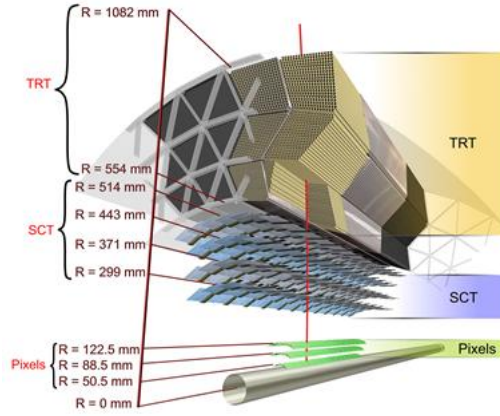


Figure 3.4: Main components of the track system. The distance of each component with respect to the beam pipe is given [37].

3.2.3 SemiConductor Tracker (SCT)

The SCT detector, which consists of silicon modules, can be seen in the middle part of figure 3.4. In the barrel there are four layers mounted in concentric cylinders. In each endcap the silicon modules are placed in three rings. The η coverage is limited to the central region, as is the pixel detector. The spatial resolution of the SCT modules is $17 \mu\text{m}$ in the $r - \phi$ plane and $580 \mu\text{m}$ along the beam pipe [37].

The SCT is designed to give up to four track points of charged particles emerging from the interaction point. Similar to the pixel is the SCT information of the track, necessary to make a precise reconstruction of the particles and the measurement of the track momentum. In figure 3.4, the SCT corresponds to the structures in the middle part of the figure.

3.2.4 Transition Radiation Tracker (TRT)

Charged particles traveling through matter radiate energy when passing materials with different dielectric constants; this property is referred to as transition radiation. The intensity of the emitted radiation is proportional to the Lorentz-Factor $\gamma = \frac{E}{m}$. This property is exploited in the Transition Radiation Tracker (TRT).

The TRT consists of drift tubes (straws) (4 mm diameter) filled with a gas mixture, interleaved with polypropylene fibers that induce the transition radiation. The radiation emitted from a charged particle excites the gas in the straws and the signal is collected. In the barrel part of the detector, around 50000 straws parallel to the beam pipe are placed. In the endcaps, 320000 straws are orthogonal to the beam pipe [37].

The electrical signal produced in a straw for an electron is in the range of 9 to 10 keV, while for

pions, for example, that are more massive than electrons, the produced signal is approx. 2 keV. A threshold can be applied to the measured electrical signal in order to make an identification of electrons from other charged objects like pions or jets. The value of the threshold is 5 keV for electron.

Additionally to the identification capability, the TRT brings up to 36 track information points. For that reason, the TRT provides a robust track information to the track reconstruction. The TRT track measurement resolution is of 130 μm in the $r - \phi$ plane and a pseudorapidity coverage up to $|\eta| < 2.0$. In figure 3.4, the TRT corresponds to the most external part of the inner detector.

3.3 Calorimeter System

The collision of high energetic particles produces a manifold of unstable particles. The decay of these yields as final products, as long the Standard Model allows, light fermions, photons and hadrons in jets.

In order to make a reconstruction of the original event, the track and energy of the products of the collision need to be measured. The track reconstruction in ATLAS is performed in the inner detector, described above. The energy of stable particles is determined using a set of calorimeter detectors. A calorimeter is a device where the particles emerging from the interaction point are stopped and the collected energy is measured.

In ATLAS, sampling calorimeters are used, meaning that the calorimeter is composed of two different materials: one with a high atomic number (passive material), in order to stop the incident objects, and another one that collects the energy deposited for the stopped particle (active material). The advantage of the sampling calorimeters is the compactness of the detector, very different when using a calorimeter made of only one material.

The relative energy resolution in sampling calorimeters to the measured energy E in GeV can be written as:

$$\sigma_E/E = \frac{a}{\sqrt{E}} \oplus \frac{b}{E} \oplus c \quad (3.2)$$

Where a , b and c are parameters that depend on the calorimeter region. a is called the sampling term and is related to the energy degradation, due to the deposit of energy in the absorbed layers. The parameter b is the noise term related to electronic noise of the LAr and with the accumulation of signal due to pile-up effects. The last term, c , is referred as constant term.

The choice of material appropriate for the construction of the calorimeter depends on the kind of interaction governing the particles to be stopped. Charged particles lose energy in matter through ionization, excitation or bremsstrahlung. For photons processes like Compton

scattering, photoelectric effect or electron-positron production are responsible for the deposition of energy. Hadrons lose energy rather through strong interaction with the atomic nucleus than through electromagnetic processes.

To cover all the possibilities of interaction two kinds of calorimeters were made in ATLAS: one electromagnetic calorimeter and one hadronic calorimeter. A sectional view of the calorimeter system is shown in figure 3.5. The ATLAS calorimeter covers the full ϕ angle and to $|\eta| < 4.9$ in pseudorapidity.

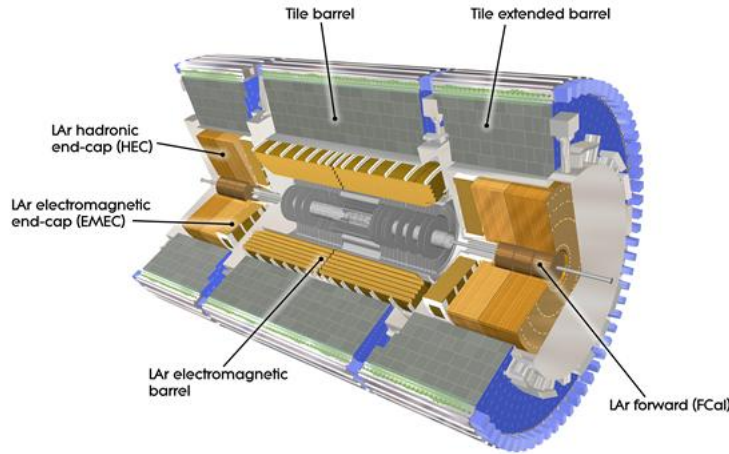


Figure 3.5: Sectional view of the ATLAS calorimeter system. The electromagnetic calorimeter is shown in yellow and the hadronic calorimeter in gray [37].

The electromagnetic calorimeter is divided in two parts: one central part with lead as passive material and one forward calorimeter made of copper. Both calorimeters use liquid argon (LAr) as active material. The central part is further segmented in a barrel part and two endcaps. The barrel electromagnetic calorimeter is surrounded by the hadronic barrel calorimeter made of steel and scintillating tiles; for that reason is it called tile calorimeter. In addition to the central tile calorimeter, the hadronic calorimeter has segments in the endcaps (Extended-Barrel-Calorimeter) and in the forward region, where tungsten is used as passive medium.

In following section a detailed description of the ATLAS calorimeters is given.

3.3.1 The Electromagnetic Calorimeter

One important characteristic of the ATLAS calorimeter system is the high coverage in pseudorapidity. In the electromagnetic calorimeter this process is done with use of a segmented distribution. The central part of the calorimeter covers the region below of $|\eta| < 3.2$ with a small gap (crack region) in the interface between the barrel and the endcaps ($1.375 < |\eta| < 1.475$). High values of the pseudorapidity are covered by the forward calorimeter (FCal). A special accordion

geometry was selected for the form of the electrodes and absorption material in central region. With help of this geometry, a full coverage in the polar angle ϕ is achieved. A summary of the principal characteristics of each segment of the electromagnetic calorimeter is given below.

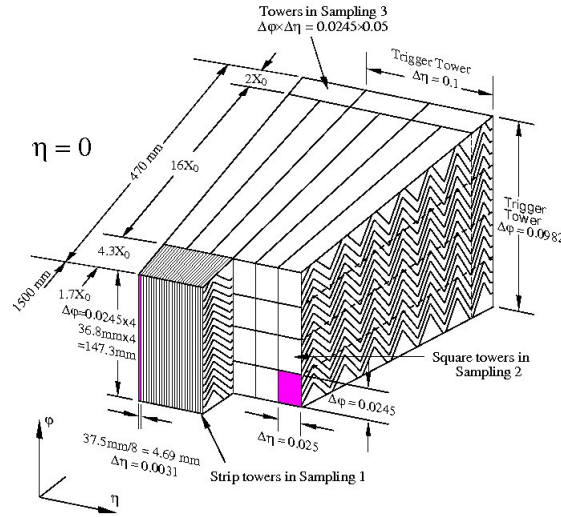


Figure 3.6: The geometry of the electromagnetic calorimeter in the barrel part is represented in the figure. The volumes designed to serve as energy deposits (samplings) are visible. The granularity of each sampling is shown [37].

- Barrel calorimeter: It consists of a 6.4 m long cylinder with an inner radius of 1.4 m and external one of 2.0 m. The pseudorapidity coverage is $|\eta| < 1.475$. As can be seen in figure 3.6, the calorimeter is segmented in three volumes (samplings) with different granularity. The first sampling, closer to the interaction point, has a granularity given by $\Delta\phi \times \Delta\eta = 0.1 \times 0.0031$. The second one, where most of the energy is expected to be deposited has a granularity of $\Delta\phi \times \Delta\eta = 0.025 \times 0.025$ while the third volume has a granularity twice as high in η ($\Delta\phi \times \Delta\eta = 0.025 \times 0.05$). The purpose of the fine granularity in the first sampling is to increase the identification of electrons over neutral pions, which can produce two energy deposits with a small angular separation, due to the decay into two photons.

A presampler is located in the region $|\eta| < 1.8$ in front of the first sampling in order to do corrections to the measured energy in the calorimeter.

- Endcap electromagnetic calorimeters (EMEC): They are settled in two wheels at each end side of the barrel. The wheels have an inner radius of 2.098 m and external one of 3.30 m; that corresponds to an absolute pseudorapidity coverage in the interval 1.375 to 3.2. Each endcap wheel consists of two concentric rings with different granularity. The external

one possesses, like the barrel calorimeter, three samplings to deposit energy. The inner wheel ($2.5 < |\eta| < 3.2$), referred to as EMEC-IW⁶, has only two samplings with a coarser granularity than that of the barrel.

- Forward calorimeter (FCal): covering the region $3.1 < |\eta| < 4.9$, the forward calorimeter is formed of cylindric structures (44,41 cm long and radius of 44.49 cm) parallel to the beam pipe [39]. The geometry of the FCal is different that the rest of the electromagnetic calorimeter; it consists of a hexagonal matrix of copper or tungsten with electrodes of the same material, with a gap between electrodes and the matrix filled with LAr. Three segments are distinguished in the FCal: the closest to the IP (approx. 4.7 m) is called FCal1 and corresponds to an electromagnetic calorimeter; FCal2 and FCal3 are hadronic calorimeters.

Figure 3.7, offers a frontal view of the FCal1. The gap between the electrodes and the copper matrix corresponds to 0.27 mm and is maintained with an isolation fiber. The granularity of the FCal1 corresponds to 0.2×0.2 in $\eta \times \phi$.

FCal2 and FCal3 are made of tungsten in order to limit the length of the calorimeter. The gap between matrix and electrodes is 0.37 mm for FCal2 and 0.5 mm for FCal3.

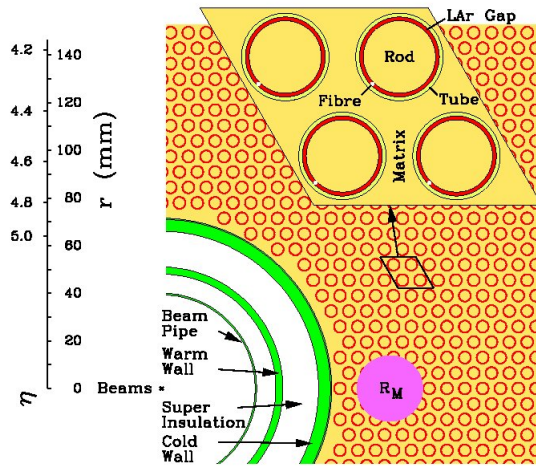


Figure 3.7: A transversal view of the front part of the forward calorimeter is shown. The special geometry of this calorimeter can be appreciated [37].

3.3.2 The Hadronic Calorimeter

The next detector, radially outside the interaction point after the electromagnetic calorimeter, is the hadronic calorimeter. The task of the hadronic calorimeter is to stop jets produced after

⁶Electromagnetic endcap inner wheel.

hadronization and to collect the released energy. The hadronic calorimeter is composed of a barrel part, an extended barrel calorimeter, commonly referred to as tile calorimeter, and the hadronic endcaps (HEC). The pseudorapidity coverage of the hadronic calorimeter is $|\eta| < 3.2$. The barrel covers $|\eta| < 1.0$, the extended barrel covers the interval $0.8 < |\eta| < 1.7$ and the HEC covers $1.5 < |\eta| < 3.2$.

The components of the hadronic calorimeter can be seen in figure 3.5. A brief description of each calorimeter is given below.

- The tile calorimeter: Barrel and extended barrel are sampling calorimeters of lead as passive medium and scintillating tiles as active medium. For that reason, both are named as tile calorimeter.

Like the electromagnetic barrel, the tile calorimeter has three volumes for energy deposition. The tile calorimeter is longitudinally segmented in a central barrel and two laterally extended barrels. The inner radius of the tile calorimeter is 2.28 m, while the external one is 4.23 m. The signal produced in the tile plates is read using photomultiplier devices.

- Hadronic endcap calorimeter (HEC): The HEC consist of two wheels (HEC1, HEC2) which are sampling calorimeters with LAr as active medium and copper as passive medium.

In the region $1.52 < |\eta| < 2.47$ the granularity of the HEC is $\Delta\phi \times \Delta\eta = 0.1 \times 0.1$. In the $2.47 < |\eta| < 3.2$ it is increased to $\Delta\phi \times \Delta\eta = 0.2 \times 0.2$.

3.4 Muon Spectrometer

Muons are charged particles with mass around 207 times the mass of the electron. With help of intense magnetic fields, muons are detected in ATLAS using the muon spectrometer.

The muon spectrometer sits outside the calorimeter system and is designed to provide precision muon measurements over a range of muon momentum of 3 GeV to 3 TeV, as well as to provide trigger signals for muon triggering. A magnetic field is used to deflect the muons traveling through the spectrometer.

The magnetic field is produced for a system of three superconducting air core toroids that are placed in the barrel part of the detector and endcaps. The strength of the magnetic field is in the range of 0.5 to 1 T. The toroidal magnetic field covers the region $|\eta| < 1.4$, while the endcap magnets cover $1.6 < |\eta| < 2.7$.

Muons traveling through the central region are detected using Monitoring Drift Tubes (MDT). This structure consists of three cylindric tubes, parallel to the beam pipe, filled with mixture of gases (Ar/CO₂). In the endcaps, the Cathode strip Chambers (CSC) are placed; these consist of three cylinders perpendicular to the MDTs. Two additional chambers are used to make precision measurements of the track and momentum of the muons: Resistive plate

chambers (RPC) and the gap Chambers (TGC). The information collected by the chambers is used to make an identification of the muons.

3.5 Luminosity Determination in ATLAS

As shown in the previous chapter, the number of events of a physics process depends on the delivered luminosity. For many studies, the uncertainty on the luminosity is the major component in the systematic uncertainty of the cross section determination. For that reason, an accurate measurement of the delivered luminosity is a key component to precise physics studies.

In particle colliders, the delivered instantaneous luminosity can be written as a function of the accelerator parameters, as:

$$L = \frac{n_b f_r N_1 N_2}{2\pi \Sigma_x \Sigma_y} \quad (3.3)$$

where n_b is the number of bunches per beam crossing, f_r is the frequency of the collisions, and N_1 and N_2 are the number of particles in each bunch. Σ_x and Σ_y are the transverse beam profiles. In order to make a measurement of the beam profiles, the so called van der Meer (vdM) scan is executed in ATLAS. In the vdM method, the beams are separated and the change in the counting of inelastic interactions μ_{inel} is determined. For the determination of μ_{inel} , specific detectors are placed at some distances of the interaction point (IP) of ATLAS. A brief description of the principal detectors is given below:

1. Beam Condition Monitor (BCM): placed at a distance of 184 cm of the IP, this subdetector consists of four diamond sensors arranged around the beam pipe. Originally designed as monitor of background levels, it provides also a fast bunch-by-bunch luminosity signal at $|\eta| = 4.2$ [40].
2. Luminosity measurement using Cherenkov Integrating Detector (LUCID): this detector is formed of aluminium tubes filled with perfluorobutane (C_4F_{10}) gas, distributed around the beam pipe at a distance of 17 m covering the pseudorapidity range $5.6 < |\eta| < 6.0$. Cherenkov photons, created in the gas from charged particles, are collected after reflections with the walls of the tubes using photomultiplier tubes.

Both detectors BCM and LUCID are fast enough to determine the ATLAS luminosity for each bunch crossing with small deadtime. Other systems of ATLAS, like the inner detector, FCal, etc are also used to measure the average particle rates, but in longer periods of time [40].

3.6 ATLAS Trigger System

For the nominal luminosity of ATLAS, an event rate of around 40 MHz is expected. However, the electronic system only has the capacity to process a data volume of 200 Hz. For that reason, a robust trigger system is an important part of the ATLAS experiment, aimed to reduce in order of approx. 10^5 the amount of data to be stored, rejecting uninteresting events.

In ATLAS, a three stage system is implemented. The first step, Level1 trigger (L1), basically uses information from the electronic system in order to find signal products of hard interactions, such as high p_T electrons, muons or jets. The next steps are commonly named High Level Trigger (HLT) and consist of two levels: the Level2 (L2) and the Event Filter (EF). At each level, the decision of the previous one is refined by using more detector information and allowing a longer time for the decision to be made. A tightening of the selection requirements is used to further reduce the signal rate. A detailed description of each level is given below.

3.6.1 Level1 Trigger (L1)

As already described, the Level1 looks for energy deposits in the calorimeters and signals in the muon system. The granularity for the search of deposits in the calorimeter is 0.1×0.1 in $\eta \times \phi$. In the case of muons candidates, the signals of muon candidates in the muon chambers are used.

When a deposit of energy in one $\eta \times \phi$ region is found, the adjacent cells are analyzed and added to the original region if the energy of these cells is bigger than a defined threshold. At the end, one cluster, called ROI, is formed. One event can have zero ROI, one, or more than one. In case one or more ROIs are found, they are all passed to the next trigger to be further inspected.

The Level1 trigger is sometimes referred to as an instrumental trigger, because all the selections are made based on electronic devices. A data rate reduction from 40 MHz to 75 kHz is achieved for this trigger level.

3.6.2 Level2 Trigger (L2)

The ROI information passes by the Level1 trigger feeds the Level2, where the full available information from the calorimeters, muon spectrometer and track system is used to analyze the found clusters. The data rate is further reduced in this step to 3,5 kHz

3.6.3 Event Filter (EF)

In the event filter, a full reconstruction of the event is made and complete information from the calorimeters muon system and inner detector is used to make a decision.

3.7 2011 and 2012 Data Taking

As this thesis is being written, the LHC was being upgraded to allow its operation at center of mass energy closer to the design value of 14 TeV in the year 2015. The physics program at the LHC started at the end of the year 2009, after solving some technical problems, with proton-proton collision at $\sqrt{s} = 900$ GeV.

In the year 2010 and 2011, the energy of the colliding proton was increasing up to 7 TeV. The instantaneous luminosity in 2010 was $2.1 \times 10^{32} \text{ s}^{-1} \text{ cm}^{-2}$ and in 2011 it increased up to $3.7 \times 10^{33} \text{ s}^{-1} \text{ cm}^{-2}$.

In the left side of the figure 3.8, the total integrated luminosity delivered by the LHC in the year 2011 is shown in green colour. After quality selections, the ATLAS data collected, in 2011, consisted of a total integrated cross section of 4.5 fb^{-1} .

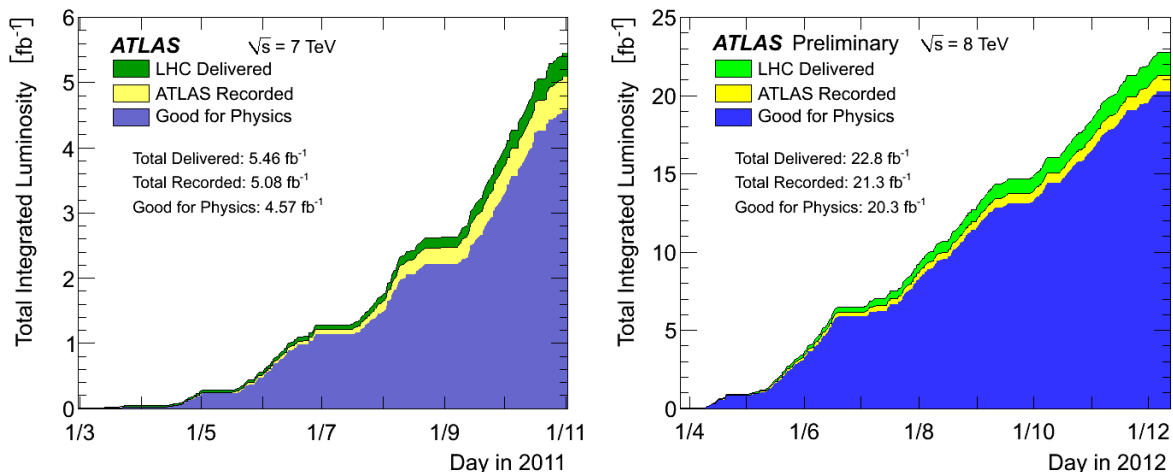


Figure 3.8: The total integrated luminosity as function of the data taking period in the years 2011 and 2012 is shown. The total integrated luminosity used in ATLAS physics analysis corresponds to the blue areas. Plots taken from [41].

In 2012, the center of mass energy of the collisions was increased to 8 TeV when an instantaneous luminosity of $8.0 \times 10^{33} \text{ s}^{-1} \text{ cm}^{-2}$ was achieved. In this work, the 2012 data is analyzed. The right side of figure 3.8 shows the development of the delivered luminosity in this period of time. The efficiency of the ATLAS data taking is larger than the 90% with a final integrated luminosity of 20.3 fb^{-1} .

An inevitable situation related to the increase of the instantaneous luminosity is the higher probability of having more than one proton-proton collision per bunch crossing. This effect is called pile-up and represents a challenge to be managed in order to have precise results in a physics analysis. In figure 3.9, a comparison of the mean number of interactions per beam crossing in the 2011 and 2012 data taking periods is shown. The average pile-up increase from 6 in 2011 to 20 in 2012.

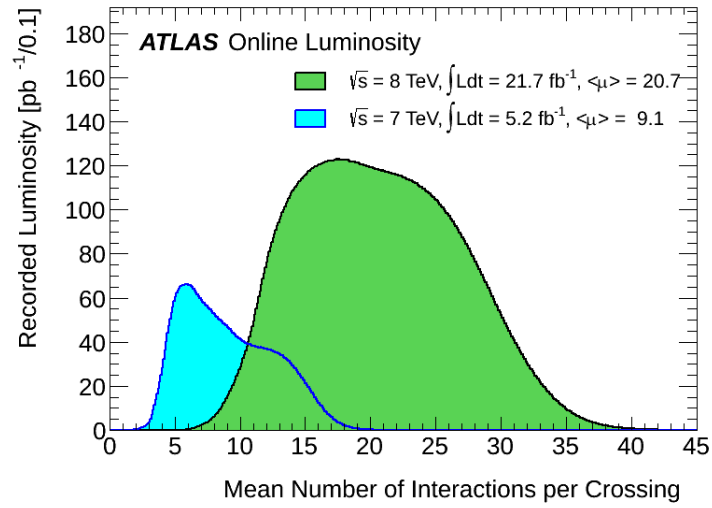


Figure 3.9: Mean number of interactions per beam crossing at $\sqrt{s} = 7$ and 8 TeV. Plot taken from [41].

$i \gg j$

Chapter 4

Electron Reconstruction Performance in ATLAS

“Many years later, as he faced the firing squad, Colonel Aureliano Buendia was to remember that distant afternoon when his father took him to discover ice.”

—One Hundred Years of Solitude

—Gabriel García Márquez

Processes with isolated leptons in the final state are important for the physics of the LHC, because they are produced mainly as the product of resonances, like those of the Z or W^\pm bosons. Additional particles are produced, which can fake the typical signal of electrons in the calorimeters or the tracking system. Heavy-flavoured lepton decays and leptons produced by the interaction of radiation with matter, contribute significantly to the final number of detected electrons. For that reason, it is of great importance to reconstruct and identify the produced electrons efficiently and, at the same time, to discard as much of the background as possible.

In the ATLAS detector, the different subdetector systems are combined in order to aid the identification of electrons at increasing levels of parameters purity, used for the selection of the candidates. A set of identification criteria is provided to be used for the physics analysis of the data with different values of efficiency, for the correct identification and background rejection.

In this chapter, an overview of the general strategy of the reconstruction and identification of electrons in the ATLAS detector is presented. The differences between electrons reconstructed and identified at high values of the pseudorapidity ($|\eta| > 2.5$) and in the central regions are discussed. At the end, a comparison of the identification efficiency between data and MC for electron candidates with high $|\eta|$ values is shown.

4.1 Electron Reconstruction

Dedicated algorithms for the reconstruction of electrons have been developed using at the beginning only MC simulations of the detector, and later using information coming from data and MC simulations. The basic idea is to identify compact deposits of energy in the electromagnetic calorimeter, depending on the coverage of the tracking system, a track that matches the properties of the energy deposit will be required. When the energy deposits are beyond the coverage of the tracking system ($|\eta| > 2.5$), only information from the calorimeters is available and the track matching is no longer possible. The central region of ATLAS ($|\eta| < 2.47$) has a full coverage of the tracking system and the reconstruction is made using the sliding-window algorithm [42].

4.1.1 Sliding-window Algorithm

The sliding-window algorithm works in three steps: first, energy deposits are observed in the electromagnetic calorimeter (clusters); second, the reconstructed tracks of charged particles in the inner detector, closer to the cluster coordinates, are associated with the cluster (track-cluster matching) and third, the full energy and coordinates of the deposit are calculated (final reconstruction). In 2012 data, an improvement of the track-cluster matching was introduced, where candidates with low energy, were suspected to be electrons losing energy due to Bremsstrahlung, and the reconstructed track and region of determination of the deposited energy were optimized to have a better description of the track and energy clusters. A detailed description of the involved steps is listed below:

- Cluster finding

Electromagnetic clusters with a total transverse energy greater than 2.5 GeV in a window of 3×5 in (η, ϕ) space, are searched using a sliding-window algorithm. The window resolution is $\Delta\eta = 0.025$ and $\Delta\phi = 0.025$, corresponding to the granularity of the electromagnetic calorimeter in the middle layer. From MC studies, an efficiency for the cluster reconstruction of almost 100% for electrons with $E_T > 20$ GeV and 97% at $E_T = 7$ GeV is expected [43].

- Track matching

Within the tracking volume, a pattern recognition and a tracking fit is performed. Tracks are extrapolated from their last measurement to the middle layer of the electromagnetic calorimeter. The extrapolated coordinates are compared to those of the reconstructed clusters. A track-cluster matching is considered successful if the angular separation $|\Delta\eta|$ between the reconstructed track and cluster is smaller than 0.05. When the ratio between the deposited energy in the hadronic calorimeter and the energy found in the electromagnetic calorimeter is lower than 10% and the ratio between the electromagnetic energy in a 3×7 and 7×7 in (η, ϕ) is bigger than 65%, a track recovery procedure is executed. This is

due to the high probability of losses due to bremsstrahlung. The size of the window for the observation of energy deposits is enlarged and an additional hypothesis for the track fits is used. This recovery was tested in the final data collected in 2011 and fully implemented in the data collected in 2012 [44].

An electromagnetic deposit is considered as an electron candidate when at least one track matches the reconstructed cluster. In the case of more than one track, tracks with more silicon hits are preferred.

- Final reconstruction

The track-cluster object found in the second step of the reconstruction process is considered an electron candidate. Then, the volume of the cluster is optimized to obtain the overall energy distribution in the different regions of the electromagnetic calorimeter. The window of the cluster is enlarged to 3×7 in the barrel part of the calorimeter and to 5×5 in the endcaps. The total energy of the candidate is determined through the sum of the estimated energy deposited in the material in front of the electromagnetic calorimeter, the measured energy in the cluster, the energy deposited outside of the cluster (lateral leakage) and the energy deposited beyond the electromagnetic calorimeter (longitudinal leakage). The spatial (η - ϕ) coordinates are taken from the track at the primary vertex.

4.1.2 Topocluster Reconstruction

For the reconstruction and identification of electrons in the forward region, only information from the calorimeters is available. For that reason, the separation between electrons, positrons or photons is not possible.

The energy in the calorimeters is grouped in three-dimensional clusters of variable sizes for the topocluster algorithm. This algorithm takes energy deposits with an energy-noise relation over one cell threshold in order to find protoclusters, these cells are seeds for the future cluster. The topocluster algorithm takes the neighboring cells to the protocluster and adds the cells to the protocluster when the energy-noise relation surpasses a neighbor threshold. The final cluster is formed with the addition of all the cells that are around the neighboring cells to get the most information available from the calorimeters. A scheme of the topocluster reconstruction is shown in the left side of figure 4.1.

4.2 Electron Identification

The reconstructed candidates found are not only isolated electrons. Jets produced in hadronization processes can produce electromagnetic deposits in the calorimeters and be reconstructed as electrons. Additionally, real electrons are also reconstructed due to the conversion of photons interacting with the material in the tracking system or in the material facing the calorimeter.

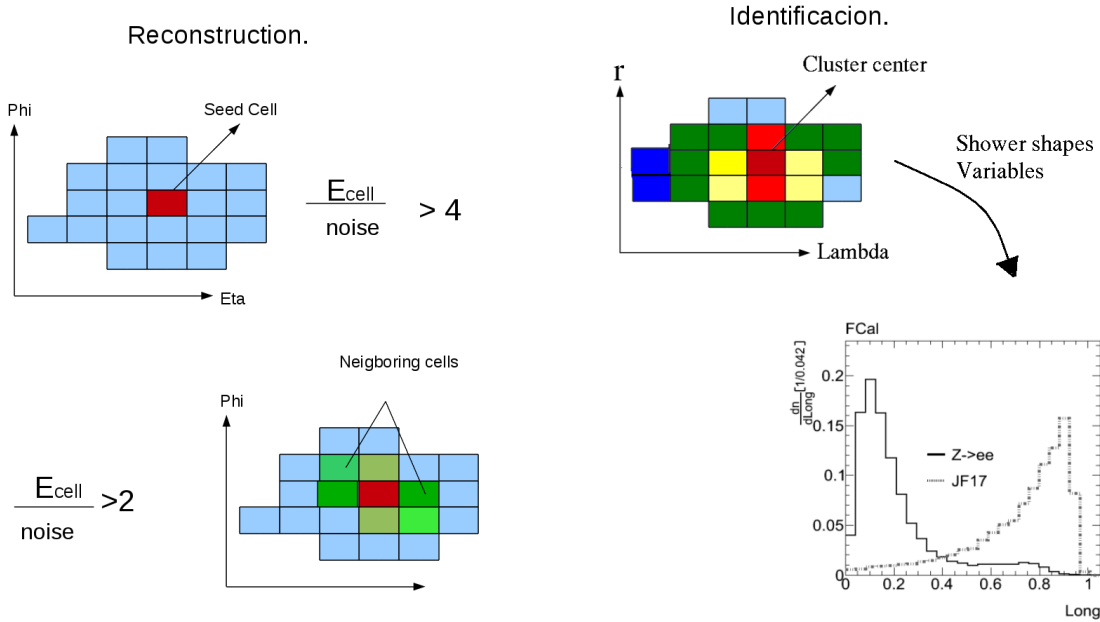


Figure 4.1: Schema of the reconstruction (left side) and identification (right side) process in the high pseudorapidity region.

For that reason, the disambiguation of electrons from specific processes is a vital element of a successful physics analysis in ATLAS.

The limits of the spatial coverage of the inner detector define two regions to be considered in electron reconstruction. The region with $|\eta| < 2.47$ is fully covered by the track system. To identify electrons, it is possible to use information from the energy deposited in the calorimeters and the track of the charged particle; this region is called central region and consists mainly of the barrel of the electromagnetic calorimeter. The forward region includes high values of the pseudorapidity ($|\eta| > 2.5$). The inner wheel of the endcaps (EMEC-IW) and the forward calorimeter (FCal) belong to this region.

Different levels of identification in the 2011 data were applied based on rectangular cuts of discriminating variables. In addition to cut-based-selection, an identification method based on a multivariate analysis was applied to the 2012 data. In the next sections, a description of the identification methods and variables used in the central and forward regions is given.

4.2.1 Central Electron Identification

In order to do a separation between signal electrons and background, the electron identification in the central region uses the longitudinal and lateral extensions of the shower shapes of the clusters, the quality of the track and the track-cluster matching as discriminator parameters.

Using these parameters, variables are built to have a set of selection criteria with increasing background rejection but decreasing identification efficiencies. At the beginning (2011), thresh-

olds on the variables were used as selection criteria. With the increase of the instantaneous luminosity and center of mass energy in 2012 data, the behavior of the shower shape variables changed, due to the increase in the number of interactions per bunch crossing. For that reason, some cuts in variables with strong pile-up dependency were loosened, and a multivariate analysis (MVA), as an alternative to the cut based identification method, was included [44].

4.2.1.1 Cut Based Selection

Thresholds in η and p_T binning over cluster and track variables are used to build a set of discriminating criteria. A description of the variables used in the identification menus is given in table 4.1. In the 2010 and 2011 data, three levels of identification were defined: loose, medium and tight. Each set is a subset of the previous one, with efficiencies of around 95% for loose, 90% for medium and 80% for tight selection. In the 2012 data, a new identification named multilepton was introduced, with the same efficiency as the loose selection, but with a higher background rejection. A list of the variables used in each identification menu can be seen in table 4.2. The multilepton menu also has the possibility of doing a better identification of electrons with p_T in the region below of 10 GeV. The purpose of this new identification criteria is to supply a better tool to work with low energy electrons coming from Higgs boson decays ($H \rightarrow ZZ^* \rightarrow 4l$). The principal characteristics of the identifications menus are discussed in more detail below.

- Loose selection

The loose identification criteria is based on cuts on the ratio of the energy deposited in the different layers of the calorimeter; the content of energy of the cluster in a 3×7 versus 7×7 cells and in the minimum number of hits in silicon detectors. With respect to the track-cluster matching quality, a maximum $\Delta\eta$ separation depending on the data taking period is tolerated to accept the candidate; for example, the cut value of this variable in 2012 is $|\Delta\eta| < 0.015$. Real electrons or photons coming from the decay of neutral pions are rejected with a cut in the separation of energy maximal in the first layer of the calorimeter.

- Medium selection

The medium selection includes the previous cuts on the shower shape variables as in the loose selection, but with a tighter cut on the quality of the track-cluster matching, namely $|\Delta\eta| < 0.005$. Real electrons produced by photon conversions are filtered by means of the rejection of reconstructed tracks, with no hits in the first layer of the pixel detector (b-layer cut). Additional track parameters are included in the medium identification criteria, such as the minimal radiation threshold in the TRT detector.

- Tight Selection

With a lower efficiency of identification, compared with medium and loose selection, but a better background rejection, electrons are identified as tight when they pass the same

Variable Type	Description	Variable name
Hadronic leakage	★ Ratio of E_T in the first layer of the hadronic calorimeter to E_T of the EM cluster (used over the range $ \eta < 0.8$ and $ \eta > 1.37$)	R_{had1}
	★ Ratio of E_T in the hadronic calorimeter to E_T of the EM cluster (used over the range $ \eta > 0.8$ and $ \eta < 1.37$)	R_{had}
Third layer of EM calorimeter	★ Ratio of E_T in the third layer to the total energy	f_3
Second layer of EM calorimeter	★ Ratio in η of cell energies in 3×7 versus 7×7 cells.	R_η
	★ Ratio in ϕ of cell energies in 3×3 versus 7×7 cells.	R_ϕ
	★ Lateral width of the shower.	$w_{\eta 2}$
First layer of EM calorimeter.	★ Total shower width.	w_{stot}
	★ Ratio of the energy difference associated with the largest and second largest energy deposit over the sum of these energies	E_{ratio}
	★ Ratio of E_T in the strip layer to the total energy	f_1
Track quality	★ Number of hits in b-layer > 0 for $ \eta < 2.01$	n_{Blayer}
	★ Number of hits in the pixel detector (≥ 1).	n_{Pixel}
	★ Number of hits in the pixels and SCT (≥ 7).	n_{Si}
	★ Transverse impact parameter (< 5 mm).	d_0
	★ Ratio of d_0 and its uncertainty (Significance of d_0)	σ_0
	★ Momentum lost by the track between the perigee and the last measurement point divided by original momentum	$\frac{\Delta p}{p}$
TRT	★ Total number of hits in the TRT.	n_{TRT}
	★ Cut on the TRT high threshold fraction	F_{HT}
Track-cluster matching	★ $\Delta\eta$ between the cluster and the track (< 0.015)	$\Delta\eta_1$
	★ $\Delta\phi$ in the middle layer and the extrapolate track	$\Delta\phi_2$
	★ Defined as $\Delta\phi_2$, but the track momentum is rescaled to the cluster energy	Δ_{Res}
	★ Ratio of cluster energy to track momentum	E/p
Conversions	★ Electron candidates matching to reconstructed photon conversions are rejected	lisConv

Table 4.1: Definition of the variables used for electron identification cuts for the central region of the detector ($|\eta| < 2.47$) [44].

cuts of the variables used in loose and medium identification, plus a tighter TRT radiation threshold and a cut on the ratio energy of the cluster and track momentum.

- Multilepton menu

With the evidence of the existence of the Higgs boson a new identification working point was introduced during the 2012 data-taking. The scope of the new menu is to increase the acceptance of the detector in a region of low energetic leptons. For that reason, the multilepton identification criterion was introduced. Effects such as the bremsstrahlung losses in charged particles were implemented, so electron candidates losing energy through interaction with matter could be identified. The ZZ analysis with 2012 data implemented this multilepton menu as a base for the identification of central electrons, due to the similarity of the final states with the Higgs boson decay.

Variable	Loose	Medium	Tight	Multilepton
$R_{had(1)}$	×	×	×	×
f_3		×	×	×
R_η	×	×	×	×
$w_{\eta 2}$	×	×	×	×
w_{stot}	×	×	×	×
E_{ratio}	×	×	×	×
n_{Blayer}		×	×	×
n_{Pixel}	×	×	×	×
n_{Si}	×	×	×	×
σ_0				×
$\frac{\Delta p}{p}$				×
n_{TRT}		×	×	×
F_{HT}		×	×	×
$\Delta\eta_1$	×	×	×	×
$\Delta\phi_2$			×	×
Δ_{Res}				×
E/p			×	
!isConv			×	

Table 4.2: The table shows the variables used for electron identification in each criteria in the central region of the detector ($|\eta| < 2.47$) [44].

In the 2012 data-taking a multivariate tool is introduced as an alternative to the cut based strategy. The MVA used the same variables as the loose, medium and tight set cuts, but probability density functions are introduced to calculate the probability of a candidate to be signal or background. In order to make a decision simultaneous variable evaluations are performed. For that reason, non-defined cuts are obtained and background analysis using cuts inversions are not possible, for example if a data driven method is necessary.

4.2.2 Forward Electron Identification

The precise measurement of some processes requires the full coverage of the azimuthal angle θ in the region that corresponds to high values of pseudorapidity ($2.5 < |\eta|$). In ATLAS, the inner wheel of electromagnetic endcaps (EMEC-IW) and the forward calorimeters (FCal) are responsible for the detection of electrons and photons with high pseudorapidity values. However, the lack of tracking information and extreme conditions, like the high levels of radiation or the presence of the beam pipe around the forward detectors, demands the use of reconstruction and identification methods that are different to those in the central region.

In order to discriminate electrons from the hadronic background, only the differences between the shape of the showers can be used. The longitudinal and transverse spread of the shower is measured in a coordinate system that depends on the center and axis of the cluster. The x coordinate of the center of the cluster (x_c) is calculated (see equation 4.1) as the sum of the energy E_i in each cell of the calorimeter, weighted with the distance of the cells (x_i) to the cluster core, normalized with the total energy.

$$x_c = \frac{1}{E_{norm}} \sum_i E_i x_i \quad (4.1)$$

A similar relation exist for the y and z axis. A vector $\vec{c} = (x_c, y_c, z_c)$ could be formed to define the shower center. One correlation matrix (C) can be calculated; its elements are the deviations of the position of each cells i of the clusters with respect to the shower center. Examples of matrix elements are shown below. The additional terms, e.g., C_{zz} , C_{yz} , C_{xz} , are calculated in the same form

$$C_{xx} = \frac{1}{\sum_i E_i^2} \sum_i E_i^2 (x_i - x_c)^2 \quad (4.2)$$

$$C_{xy} = \frac{1}{\sum_i E_i^2} \sum_i E_i^2 (x_i - x_c)(y_i - y_c) \quad (4.3)$$

With the help of the eigenvectors of the matrix C , the axis of the shower can be defined. The axis of cluster \vec{s} is one of the eigenvectors of C with an angular difference, with respect to a vector pointing from the Interaction Point to the center of the shower, no bigger than 20° .

With the help of the equation 4.4, the lateral extension of one cell r_i can be calculated using the vectors \vec{c} , \vec{s} and a vector \vec{m}_i with the coordinates of the cell.

$$r_i = |(\vec{m}_i - \vec{c}) \times \vec{s}| \quad (4.4)$$

A similar relation can be used to find the longitudinal extension λ_i along the shower axis:

$$\lambda_i = (\vec{m}_i - \vec{c}) \cdot \vec{s} \quad (4.5)$$

The total lateral and longitudinal extension of the cluster is calculated as the sum of the r_i and λ_i , over the total of cells of the cluster, weighted with the total energy of the cluster.

With the cluster parameters described above, variables are defined using clusters moments with respect to the center \vec{c} and axis of the cluster \vec{s} defined above, or a combination of them. The cluster moment of degree n of a variable x is defined as:

$$\langle x^n \rangle = \frac{1}{E_{norm}} \sum_i E_i x_i^n \quad (4.6)$$

where $E_{norm} = \sum_i E_i$ and i is the index of the cell in the cluster.

Six variables in the forward region are available for the identification of electrons. In the following part of this section these variables are described.

- Center lambda (λ_c): Electrons produce more compact showers as jets. The depth of the shower (λ) depends on the energy of the incident particle and the characteristics of the calorimeter. The center lambda is a measurement of distance of the cluster center with respect to the front of the calorimeter along the cluster axis. The distribution of the variables is different for EMEC and FCal, but a maximal value of the variable at approx 200 mm for EMEC and 220 mm for FCal exists in both cases.
- Second moment of lambda ($\langle \lambda^2 \rangle$): The Second moment of the longitudinal extension of the cluster λ_i is defined using:

$$\langle \lambda^2 \rangle = \frac{1}{\sum_i E_i} \sum_i E_i \lambda_i^2 \quad (4.7)$$

Due to the different constituent materials of EMEC and FCal, the behavior of this variable is different in each of the forward calorimeters, but for real electrons the contribution is more important at low values of the center λ .

- Second moment of r ($\langle r^2 \rangle$): The radial distance of the cells r_i with respect to the shower axis is used to evaluate the transverse form of the shower shapes. A similar equation to the one shown above (see equation 4.7) is used to get the $\langle r^2 \rangle$

$$\langle r^2 \rangle = \frac{1}{\sum_i E_i} \sum_i E_i r_i^2 \quad (4.8)$$

The maximum value of the variable is around of 1400 mm² for EMEC and 600 mm² for FCal for real electrons. The lateral extension from the electrons is expected be smaller that the extension of showers with hadronic origin.

- Energy fraction ($Frac_{Max}$): The energy fraction of the cluster in the more energetic cell is a good variable to discriminate between real electrons and jets. Electrons deposit more energy in a small volume of the calorimeter; for that reason, bigger values of these variables indicate the possibility to have an electron. Signal electrons deposit in the most energetic cells between 45% and 80% of the total energy in both calorimeters with tiny differences, due to the different granularity in EMEC and FCal.
- Lateral: The lateral variable is calculated using the equation shown below:

$$lateral = \frac{lateral_a}{lateral_a + lateral_b} \quad (4.9)$$

$lateral_a$ and $lateral_b$ are calculated using the equation 4.8. In $lateral_a$ the values of r_i are equal to zero for the most energetic cells. In the case of $lateral_b$, the distances r_i are set to 4 cm for the most energetic cells and zero for the rest. Lateral will show small values when the contribution of the most energetic cells to the overall energy content of the cluster, in a perpendicular direction to the cluster axis, is bigger than that from the rest of the cells. It is expected that jets deposit energy in more cells, so the importance of the most energetic cells is lower in that case. A good separation between signal and background can be made at values of lateral of 0.6 for EMEC and 0.3 for FCal.

- Longitudinal: Similarly to the lateral variable, a relation depending on the distance of the cells with respect to the most energetic cells and the energy content of each cell can be built along the shower axis. The longitudinal variable is defined as:

$$longitudinal = \frac{longitudinal_a}{longitudinal_a + longitudinal_b} \quad (4.10)$$

where $longitudinal_a$ and $longitudinal_b$ are calculated using the equation 4.7. In $longitudinal_a$ is λ_i equal to zero for the most energetic cells. In $longitudinal_b$ is $\lambda_i = 10$ cm for the most energetic cells and zero for the rest. Similar as for the lateral variable, low longitudinal values are expected for showers produced for electrons. In this case, the cut to make a signal-background separation is around 0.2 and 0.4 for EMEC and FCal, respectively.

During the first year and a half of operation, only two identification criteria were available in forward region: loose and tight. Then, for the second half of 2011, a new pile-up independent identification was developed: forward medium. In the 2012 data, a drop in the identification efficiency, due to the increasing pile-up, was observed. A new retuning of the identification cuts with a MVA method, similar to that in the central electron identification, was made.

4.2.3 Electron Isolation

In addition to the previous identification selections, isolation methods are used in ATLAS in order to increase the rejection of jets faking electrons. Two types of isolation are used in ATLAS: calorimeter and track based isolation. In the case of the calorimeter isolation, the sum of transverse energy of the cells around the cluster in a cone $\Delta R = \sqrt{\Delta\eta^2 + \Delta\phi^2}$, excluding the E_T of the clusters, must be lower than certain value. Each analysis determines the isolation criteria to be used. The track isolation is similar to the calorimeter isolation, but it takes the sum of the momentum contributions of the tracks in a cone ΔR .

4.3 Efficiency of the Identification

For the evaluation of the electron identification efficiency, a method to find real electrons is needed. The tag and probe method (T&P), using $Z \rightarrow e^+e^-$ and $J/\psi \rightarrow e^+e^-$ decays, was implemented for this purpose. $Z \rightarrow e^+e^-$ and $J/\psi \rightarrow e^+e^-$ are used because the mass of these particles is well defined and the energy of the electrons comes from them. They are standard candle for the particle physics.

In the T&P method, one of the electrons, product of the decay, must pass a strict selection criteria (tag electron); the second electron is used to make the efficiency estimation (probe electron). The invariant mass of both selected candidates should be within a mass interval around the mass of the Z boson or J/ψ . Additional cuts over the candidates or events (isolation, missing transverse energy, etc) can be applied. The probe sample should be separated in electron signal and background. A fitting procedure can be conducted, with appropriate hypothesis, to the functions describing the signal and background shapes. The efficiency ϵ_{id} is calculated using the equation shown below

$$\epsilon_{id} = \frac{N_{id}}{N_{Reco}} \quad (4.11)$$

N_{Reco} and N_{id} are the number of probe electrons before and after the identification.

To do a comparison with the MC prediction, the MC efficiency ϵ_{MC} is calculated using the same equation, but, in this case, no background subtraction is necessary.

ϵ_{Data} and ϵ_{MC} can be used to calculate scale factors (SF) to correct the MC efficiencies, in order to do a better data and MC comparison. The SF is given by:

$$SF = \frac{\epsilon_{Data}}{\epsilon_{MC}} \quad (4.12)$$

In the next sections, a detailed description of the determination of the efficiency of the identification of electron candidates in the forward region is given.

4.3.1 Efficiency Determination in Forward Region

For the evaluation of the efficiency of the identification of the forward electrons, the tag and probe method (T&P), with one central electron and one forward electron candidate, is used. This was done in order to extract the invariant mass spectrum of Z bosons in data samples and to get the efficiency of the identification in forward calorimeters. A pre-event selection was made (see detailed description of the event selection in section 5.1.1), based on a list of runs to be used in physics analysis. Only events with more than three tracks per primary vertex and reconstructed electrons which pass a trigger selection depending on the data period, are considered. Three high level triggers were used, with E_T of 20 GeV and medium identification. With the increase of the number of interactions per beam crossing, a new threshold of 22 GeV was used and an electron isolation and veto in the deposited hadronic energy were applied at the end of the data taking ¹.

Electron candidates are searched for in the events that pass the preselection mentioned before. The tag electrons are required to pass the following cuts:

- sliding-window algorithm reconstruction
- $p_T > 25$ GeV
- $|\eta| < 2.47$, outside of the crack region.
- Calorimeter and track isolation
- tight identification

The probe electrons in the forward region should pass less cuts:

- Topocluster reconstruction
- $p_T > 20$ GeV
- $2.5 < |\eta| < 4.9$

Additionally, electron isolation on the tag electron is required. A calorimeter isolation equivalent to 95% of E_T in a cone of 0.2 around the selected electron is used. Meanwhile, the track should have a p_T value less than 1 GeV in a cone of 0.3 around the selected track. The impact of the isolation criteria to the basic selection and the independence with the pile-up effect can be seen in tables 4.3, 4.4 and 4.5.

¹The triggers used were: EF_e20_medium, EF_e22_medium and EF_e22vh_medium1. The ATLAS trigger naming convention is:

(trigger level)_(number of objects)(type of object)(threshold)_(quality criteria)

EMEC (2 fb^{-1})			
	Signal	Back	Signal/Back
reco	177059	79844	2.22
reco + track isolation	149108	36748	4.06
reco + calo isolation	154040	45384	3.39

Table 4.3: Number of events at reco level in the standard selection and with the introduction of track and energy isolation criteria. Calorimeter isolation: 95% of E_T in a cone of 0.2 around the central tagged electron. The track isolation: p_T less than 1 GeV in a cone of 0.3 around the selected track of the central electron.

FCal (2 fb^{-1})			
	Signal	Back	Signal/Back
reco	56608	44472	1.27
reco + track isolation	57162	26507	2.16
reco + calo isolation	56554	20291	2.79

Table 4.4: Number of events at reco level in the standard selection and with the introduction of track and calorimeter isolation criteria. Calorimeter isolation: 95% of E_T in a cone of 0.2 around the central tagged electron. Track isolation: p_T less than 1 GeV in a cone of 0.3 around the selected track of the central electron.

Signal/Back						
NPV	EMEC (2 fb^{-1})			FCal (2 fb^{-1})		
	reco	reco + track isolation	reco + calo isolation	reco	reco + track isolation	reco + calo isolation
0-2	1.89	4.08	3.42	1.24	2.88	2.12
2-5	2.26	4.15	3.48	1.29	3.01	2.32
5-7	1.88	3.99	3.22	1.31	2.70	2.21
7-9	2.02	4.14	3.39	1.32	2.68	2.10
9-16	1.91	3.85	3.44	1.16	2.49	1.77

Table 4.5: Signal background relation at reco level in the standard selection and with the introduction of track and calorimeter isolation criteria. Calorimeter isolation: 95% of E_T in a cone of 0.2 around the central tagged electron. Track isolation: p_T less than 1 GeV in a cone of 0.3 around the selected track of the central electron.

The tables 4.3 and 4.4 show the effect of the calorimeter and track isolation in the selection

of forward electron candidates without any additional identification (reco level). The sample corresponds to one fraction of the 2011 data, the signal and background numbers are derived using a T&P method (see 4.3.1.1). The p_T of the forward electrons should be larger than 30 GeV. The calorimeter isolation is applied on the central electron tagged with the forward candidate, correspond to a 95% of E_T in a cone of 0.2 around of the selected electron. Meanwhile, the track should have a p_T value less than 1 GeV in a cone of 0.3 around the selected track.

The tables show that the amount of background is reduced with the use of the isolation criteria, but the signal is less affected. The pile-up effect over the isolation criteria can be seen in the table 4.5, where the ratio signal and background as a function of the number of primary vertex with more than 3 tracks is calculated. The signal background relation increases in EMEC and FCal and the increment is constant as a function of NPV. One last cleaning cut is applied with the help of the missing E_T ($E_T^{miss.}$) ($E_T^{miss.} < 25$ GeV) in order to reduce the background produced by the $W \rightarrow \nu_e e$ process.

4.3.1.1 Signal and Background Separation

The invariant mass of tag and probe electrons is calculated and pairs with mass within an interval of 55 to 130 GeV around the Z mass are considered. The invariant mass spectrum had contributions from real electrons coming from Z bosons and background electrons. A fit procedure was implemented using RooFit [45] in the mass range to make a separation of signal and background.

The signal is fitted using a Crystal-Ball function convoluted to a Breit-Wigner. The Breit-Wigner function is used to give a description of the Z peak, the Crystal-Ball is introduced to get account of the bremsstrahlung loses at low energy values of the electron candidates. With the help of Z MC simulations, parameters like the mean of the Breit-Wigner are determined and used as start parameters when the data are fitted; the width of the Breit-Wigner is fixed to the PDG [13] value of the Z width. The exponential fall of the Crystal-Ball is fixed too, with the help of the MC; the mean and sigma of this function are fixed with the data. The explicit form of the functions used to fit the signal and background can be seen in appendix B.

The background is described with a Landau function. The mean and the sigma value of the function are determined using data. The typical form of the curves is shown in figure 4.2. The left plot shows the Crystal-Ball function in red and the Breit-Wigner in solid blue. The convolution is shown in dashed blue. The Landau function can be seen in the right plot.

In figure 4.3, the invariant mass of tag and probe pairs is shown; the plot corresponds to probe candidates between $2.60 < |\eta| < 2.70$. The signal (black) and the Landau background (red) separation is visible. The number of signal candidates in a mass window 80-100 GeV is used to calculate the efficiency.

The identification criteria are further applied to the forward candidates to get the identi-

fication efficiency. The effective background reduction using the identification criteria on the forward candidates can be seen in figure 4.4, where the candidates after loose and tight selection are shown.

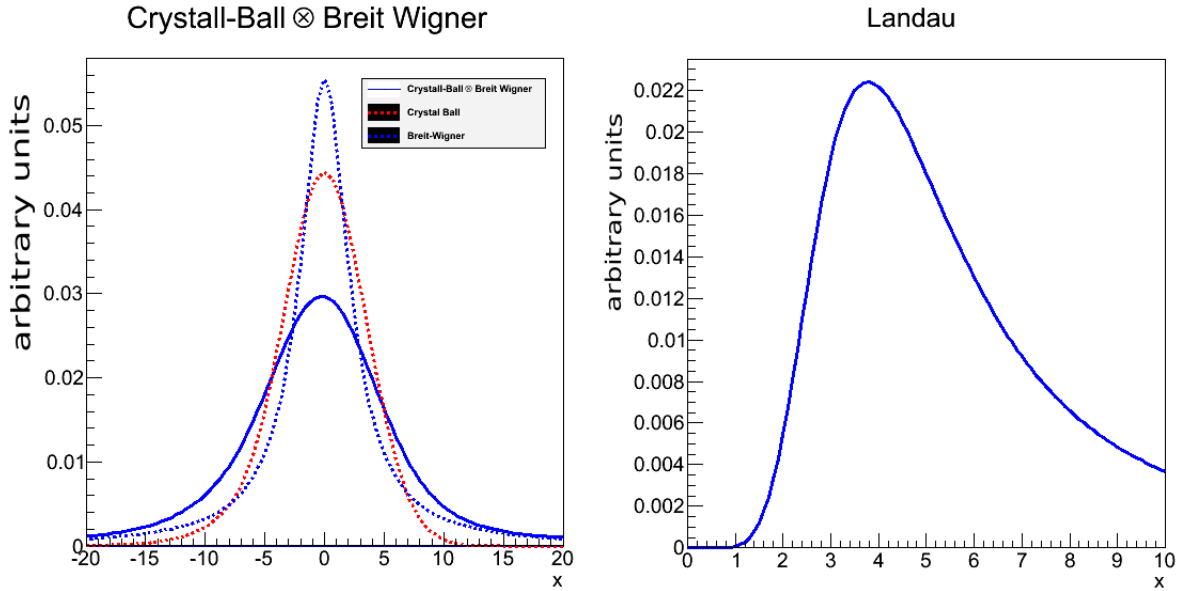


Figure 4.2: The figure shows the functions used to fit the data and the background in order to have the number of electrons corresponding to signal and background. A description of the used function is given in appendix B.

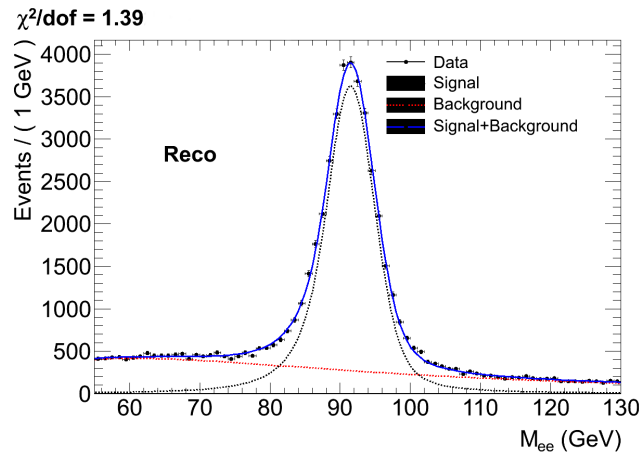


Figure 4.3: Invariant mass spectrum of tag and probe pairs without identification criteria in $2.60 < |\eta| < 2.70$. The graph shows the signal and background fitting

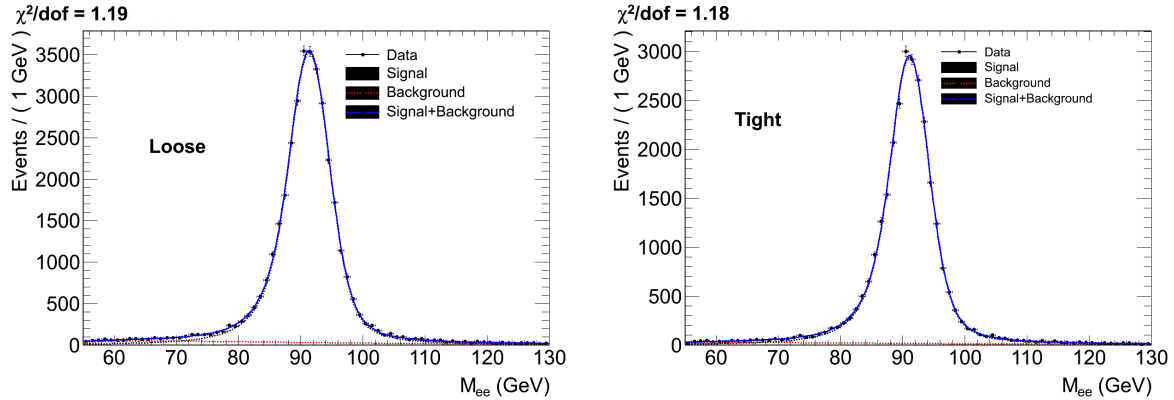


Figure 4.4: Invariant mass spectrum of tag and probe pairs with loose (left) and tight (right) identification criteria in $2.60 < |\eta| < 2.70$

4.3.1.2 Uncertainties

Apart from statistical uncertainties, which are calculated assuming binomial statistics, and which have shown tiny contributions to the total uncertainties, different sources of systematic errors were studied. A detailed description of the systematic sources is listed below.

- Change of the fit range: The fit quality for the signal and the background should depend on the election of the fit rang; for that reason, the efficiency values for a smaller fit range (60-120 GeV) and a larger one (50-140 GeV) were calculated.
- Signal mass window: For the estimation of the efficiency, the candidates with invariant mass around the mass of the Z boson are used. The width of the window can induce tiny differences in the efficiency values. A bigger mass window, 60-120 GeV, was used to quantify this effect.
- Tag electron selection: Variations to the characteristics of the tag electron were introduced to see the effect of the tag selection on efficiency. The minimum p_T values of the central electron were changed to 23 GeV and 30 GeV.
- Calorimeter isolation: The effects of tighter and weaker energy isolation over the central electron were probed. The standard isolation in the electromagnetic calorimeter, corresponding to 95% of E_T in a cone of 0.2, is changed to a 98% and 90% in the same cone of 0.2 around the central electron.
- Track Isolation: The track isolation of the central electron was changed, too. Two effects on the track isolation were tested. One of these corresponds to the usual track cone isolation of 0.3 with a larger limit of the energy, namely p_T down to 3 GeV. The impact

of the cone isolation selection was probed changing it from 0.3 to 0.4 with the same cut on the p_T in the cone (1 GeV).

- Missing E_T variation: Two variations to the E_T^{miss} were applied: $E_T^{miss} < 20$ GeV and $E_T^{miss} < 35$ GeV.
- Background subtraction: The description of the background is important to get the correct amount of signal in the mass window. For $2.50 < |\eta| < 3.16$ (EMEC), an exponential function for the background subtraction was used. In $3.35 < |\eta| < 4.90$ (FCal), Chebyshev polynomials of third order were used.
- MC Template: The signal was fitted using shapes derived using only MC simulations to modeling the signal distribution.
- Counting in mass window: Instead of using the value given by the fit, the number of events in the mass window were counted.

In general, the main contributions come from the background choice and the use of MC templates in EMEC and FCal. All the systematic variations are assumed to be uncorrelated and added in quadrature to get the total systematic uncertainties.

4.3.2 Efficiencies with 2010 Data Cuts

With data collected in the year 2010, a basic set of cuts on the variables defined in the section 4.2.2 was derived: a loose selection, with efficiency around the 95% in EMEC and 90% in FCal, applying cuts on the λ_c , $\langle \lambda^2 \rangle$ and $\langle r^2 \rangle$ variables; and a tight selection that uses all the six shower shape variables to make the identification with an efficiency of 70% in EMEC and 60% in FCal. To compare the results, a detailed study of the efficiencies of 2011 data that uses this set of cuts is described below.

4.3.2.1 Efficiency as function of Eta

In order to make efficiency studies, 10 $|\eta|$ -bins in the forward region were defined. In the EMEC within the interval 2.50 to 3.00, five bins with a width of 0.1 and one bin from 3.00 to 3.16 were used. In the FCal only three bins were defined, due to the low number of probe electrons. The bins are 3.35-3.60, 3.60-4.00 and 4.00-4.90. The interval $3.16 < |\eta| < 3.35$ corresponds to the transition between EMEC and FCal.

Data-MC comparison is shown in 4.5. The agreement is better in the figure on the left side of 4.5, especially in the EMEC region. The right side and the left side of 4.5 show a loss of efficiency in the range $3.16 < |\eta| < 3.35$, due the transition between calorimeters.

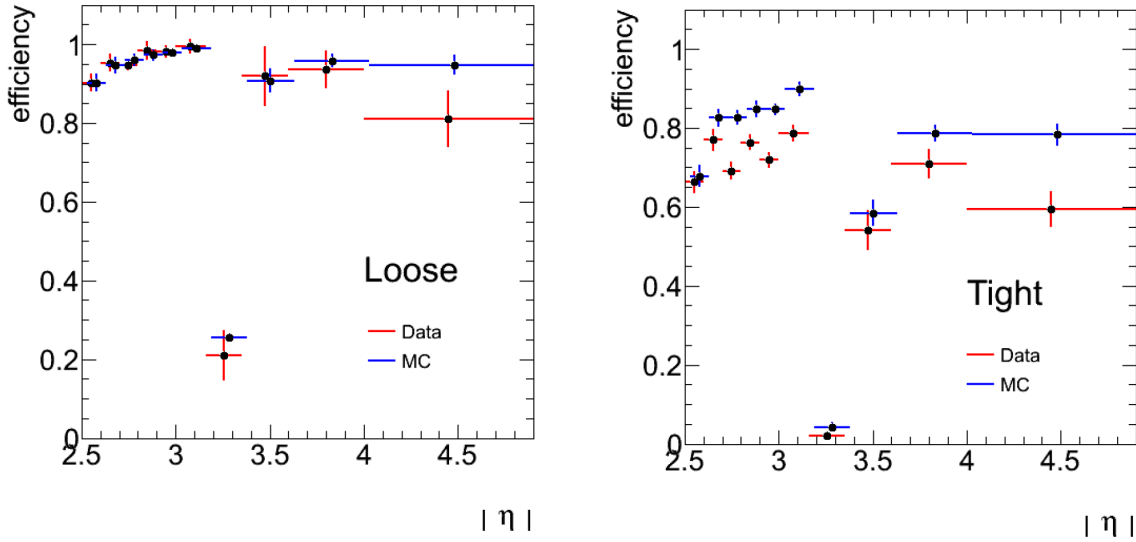


Figure 4.5: The plot shows a comparison of the efficiency in data and MC, after loose and tight selection. Data and MC agreement is better for EMEC with loose forward identification.

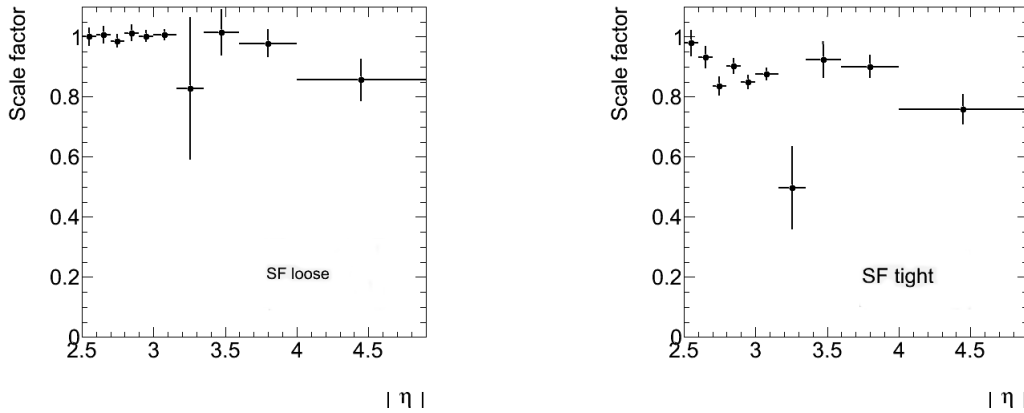


Figure 4.6: SF as function of η for loose (left) and tight (right). Statistical and systematics uncertainties are shown.

From the right plot it is clear that the scale factors, defined in equation 4.12, are necessary in order to account for incorrect modeling in the MC. The corresponding SFs as a function of $|\eta|$ are shown in figure 4.6. The SFs for EMEC loose are closer to one.

4.3.2.2 Efficiency as Function of p_T

The tag and probe method also helped to determine the efficiency as a function of the p_T of the probe candidates. The independent contributions in EMEC and FCal are visible in figures 4.7 and 4.8.

It can be observed that the data and MC agreement is quite good. However, in the EMEC, after tight selection some, discrepancies are visible. The efficiency in the four plots shows a drop for high p_T values.

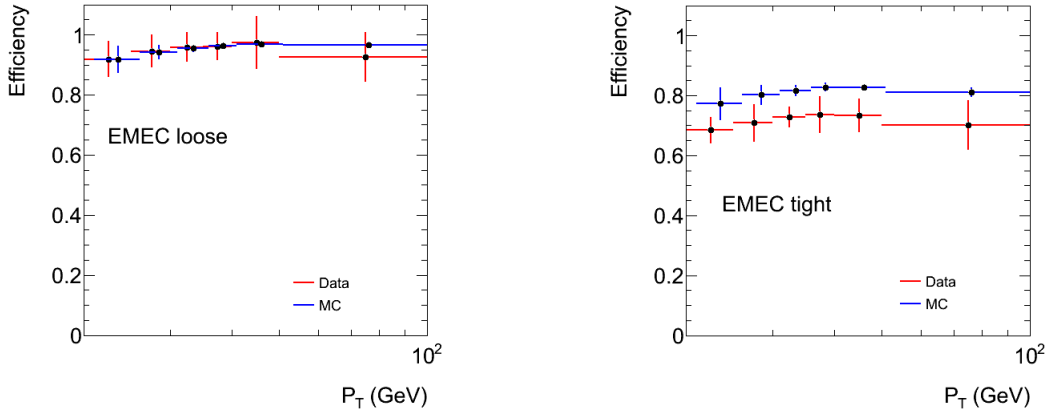


Figure 4.7: Identification efficiencies as a function of p_T in EMEC for loose (left) and tight (right). Statistical and systematic uncertainties are shown

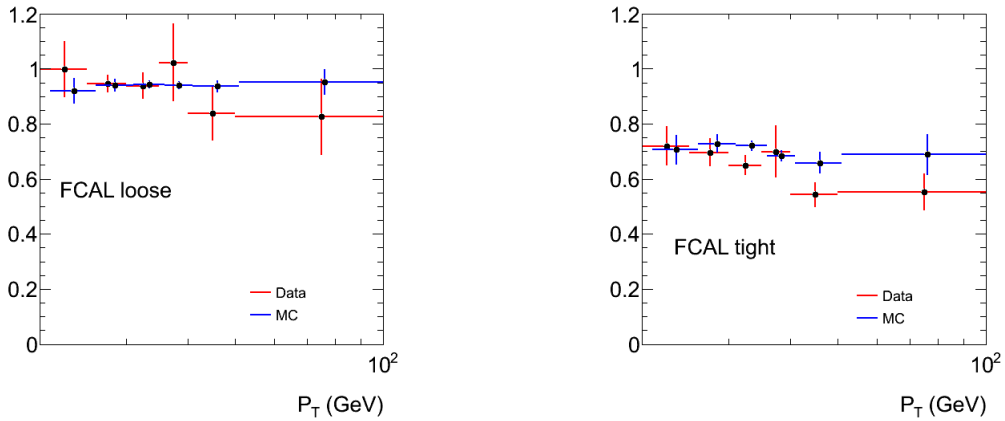


Figure 4.8: Identification efficiencies as a function of p_T in FCAL for loose (left) and tight (right). Statistical and systematic uncertainties are shown

4.3.2.3 Efficiency as Function of NPV

With the increase of the luminosity, the pile-up increases, too. The pile-up can be quantified using the information of the number of primary vertex (NPV). In figures 4.9 and 4.10, the efficiency as a function of NPV is shown. The Data-MC agreement is quite good, especially in EMEC and FCAL loose. However, the dependency of the efficiency is strong after tight selection in EMEC and FCAL.

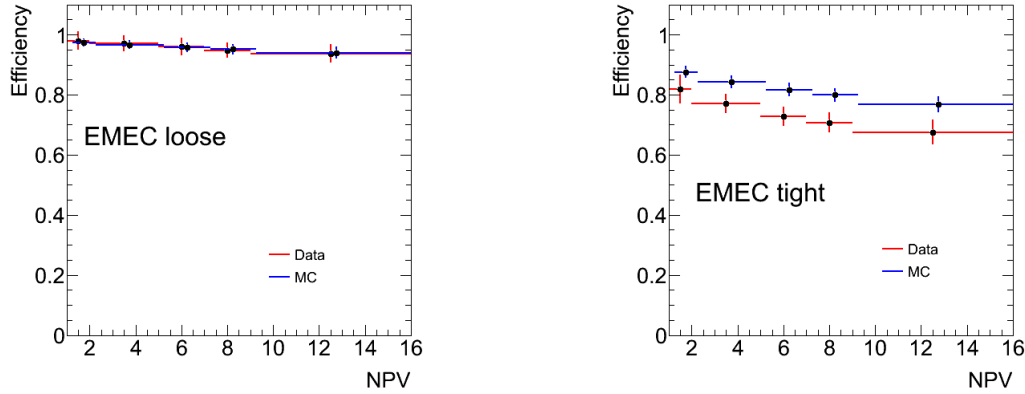


Figure 4.9: Identification efficiencies as function of NPV in EMEC for loose (left) and tight (right). Statistical and systematic uncertainties are shown.

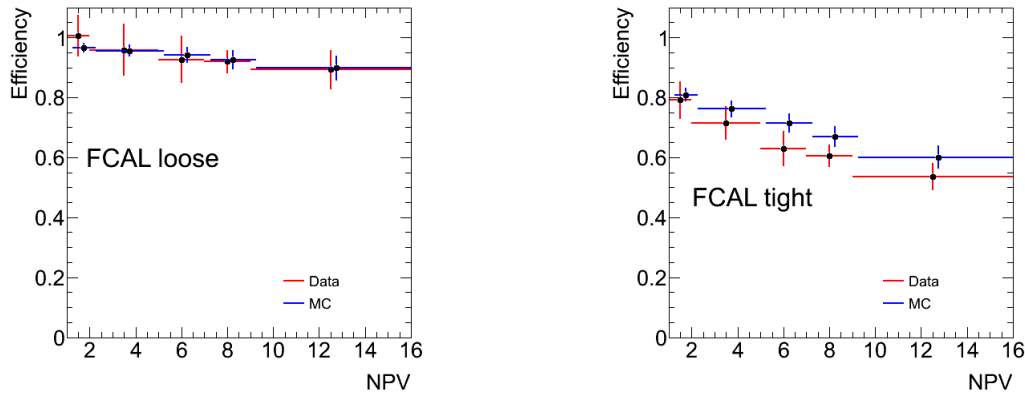


Figure 4.10: Identification efficiencies as function NPV in FCal for loose (left) and tight (right). Statistical and systematic uncertainties are shown.

4.3.3 Efficiencies with Pile-up Independent Cut Set

Figure 4.9 and 4.10 show the need for optimization of the identification cuts in order to have efficiencies that are independent from pile-up. To do that, a systematic study of variable and cuts behavior as function of the pile-up increase was made. As a result, new thresholds for the variables were defined, with dependency of the p_T on the forward candidate, η value and NPV. The resulting efficiencies, scale factors and their respective uncertainties have been determined in the same way, as described above for the unoptimized set with the cuts from 2010.

In addition to the loose and tight identification, a new medium identification level was introduced for forward electrons, in order to parallel what was done for central electrons.

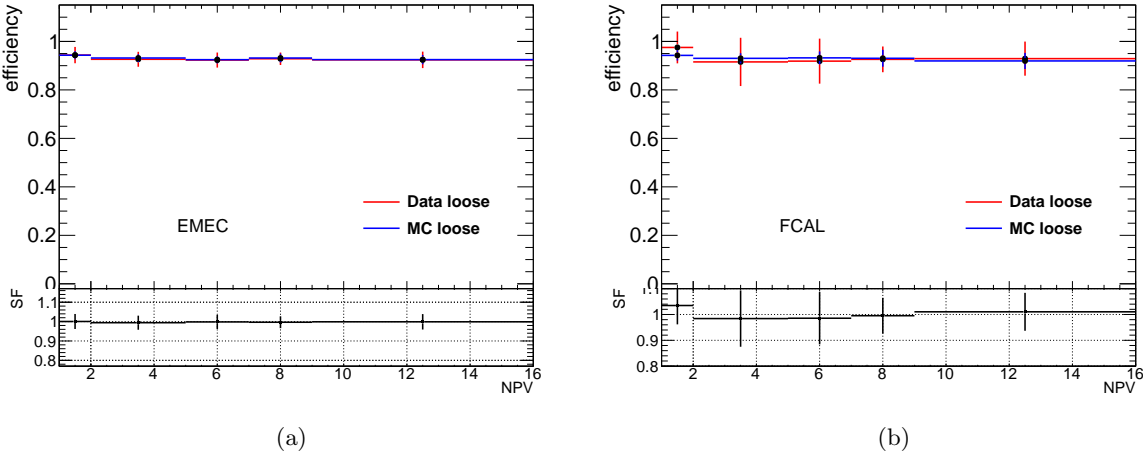


Figure 4.11: Identification efficiencies as function of NPV with new loose identification. EMEC (a) and FCal (b).

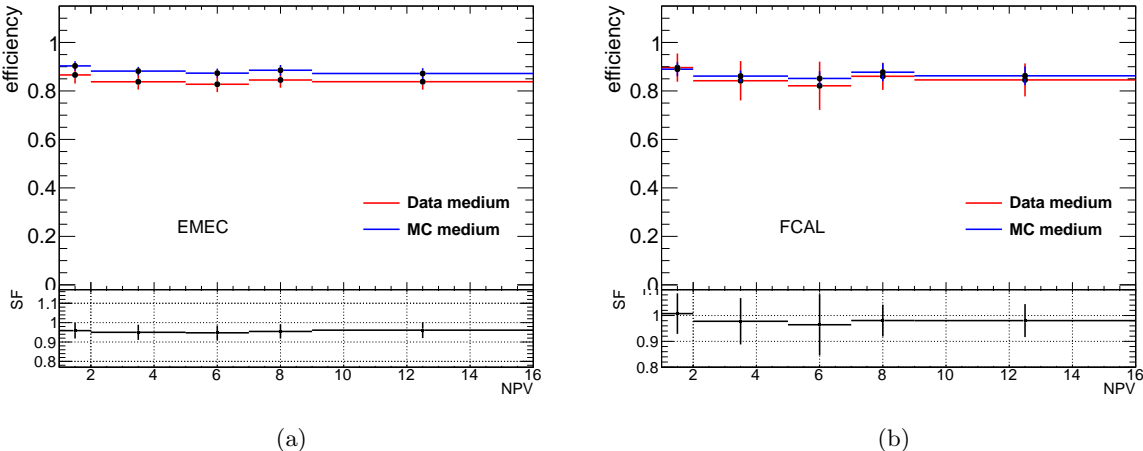


Figure 4.12: Identification efficiencies as function of NPV with new medium identification. EMEC (a) and FCal (b).

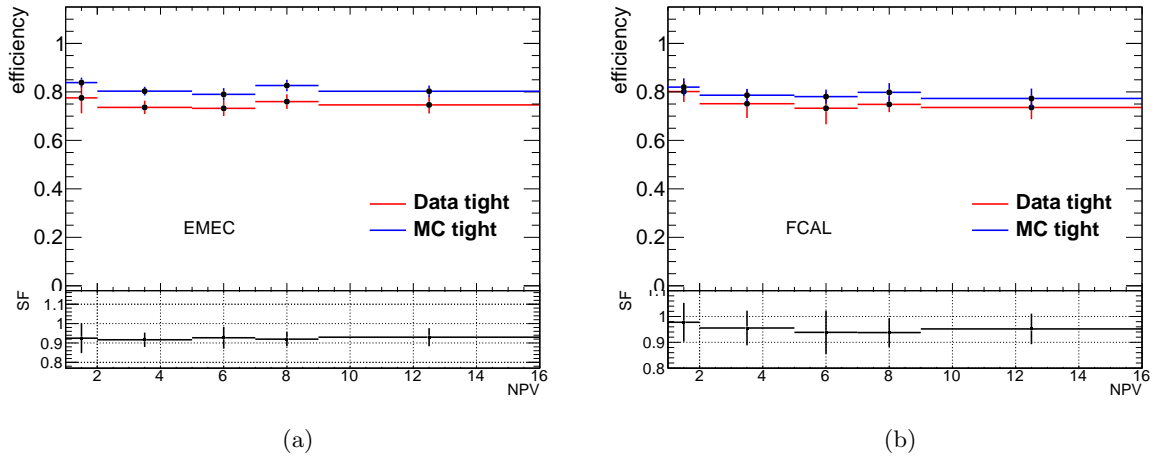


Figure 4.13: Identification efficiencies as function of NPV with new tight identification. EMEC (a) and FCal (b).

4.3.3.1 Efficiency as Function of NPV

With the new set of optimized identification cuts, the strong dependency of the efficiencies as function of the NPV is reduced in the 2011 data, as can be seen in the figures 4.11, 4.12 and 4.13. The new efficiencies are constant in the full range of variation of the NPV in EMEC and in FCal. At the same time, the agreement Data-MC is quite good, especially for the loose and the new medium identification criteria, as can be seen in the ratio plot at the bottom of the figures 4.11 and 4.12. In the case of the tight selection (figure 4.13), a 5% deviation of the unity in both forward calorimeters can be seen. As with the old set of cuts, the nice agreement of the efficiencies for the data and the predicted MC efficiencies make the use of SFs as function of the NPV unnecessary.

4.3.3.2 Efficiency as Function of p_T

The efficiency as function of p_T can be seen in the figures 4.14, 4.15 and 4.16 for EMEC and FCal. It can be observed that the agreement Data-MC is quite good in EMEC at low energy for all three identification criteria; only the last bin shows a bigger discrepancy. In the FCal the agreement is not as good as in EMEC, but between the total uncertainties, data and MC still correspond, so no further scale factor corrections as a function of p_T are necessary.

4.3.3.3 Efficiency as Function of Eta

The efficiencies as a function of $|\eta|$ are shown in figures 4.17, 4.18 and 4.19. It can be observed that the Data-MC agreement is not as good as that shown in figure 4.5 with the old identification set of cuts, in EMEC and in FCal, but both, data and MC efficiencies, show the same tendency.

The drop in efficiency seen in the range $3.16 < |\eta| < 3.35$ is as before due to the fact that this is the transition region between EMEC and FCal.

The lack of agreement between the predicted and observed efficiencies demands the introduction of new scale factors as a function of η , as before. The corresponding SFs can be seen in the bottom plots in each figure. The systematic uncertainties are between 2% and 4% in the EMEC and between 4% and 7% in FCal; those are calculated as before.

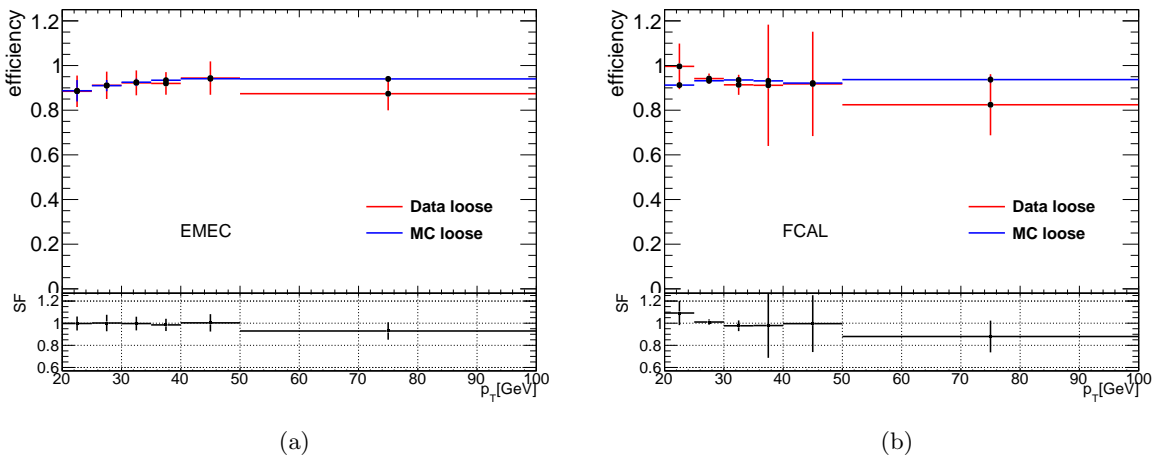


Figure 4.14: Identification efficiencies as function of p_T with new loose identification. EMEC (a) and FCal (b).

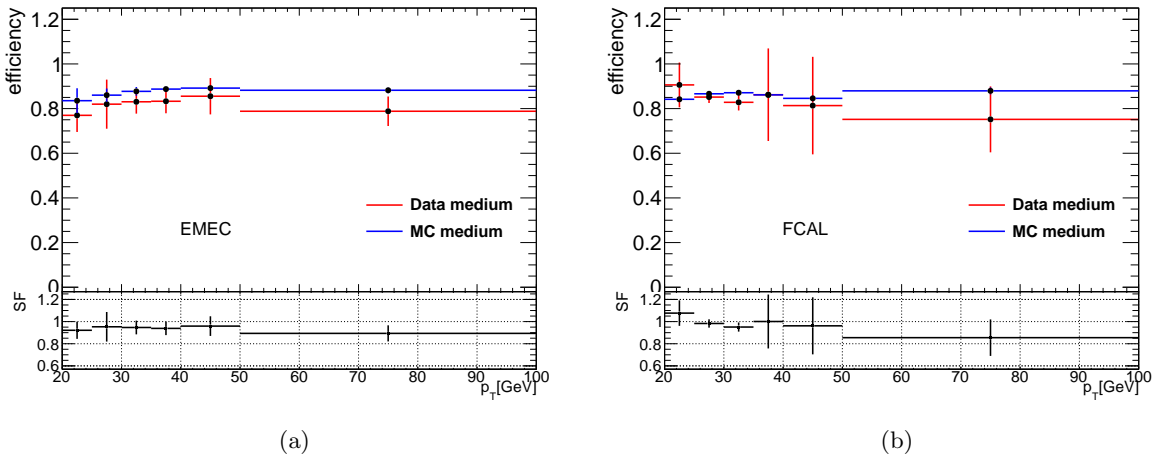


Figure 4.15: Identification efficiencies as function of p_T with new medium identification. EMEC (a) and FCal (b).

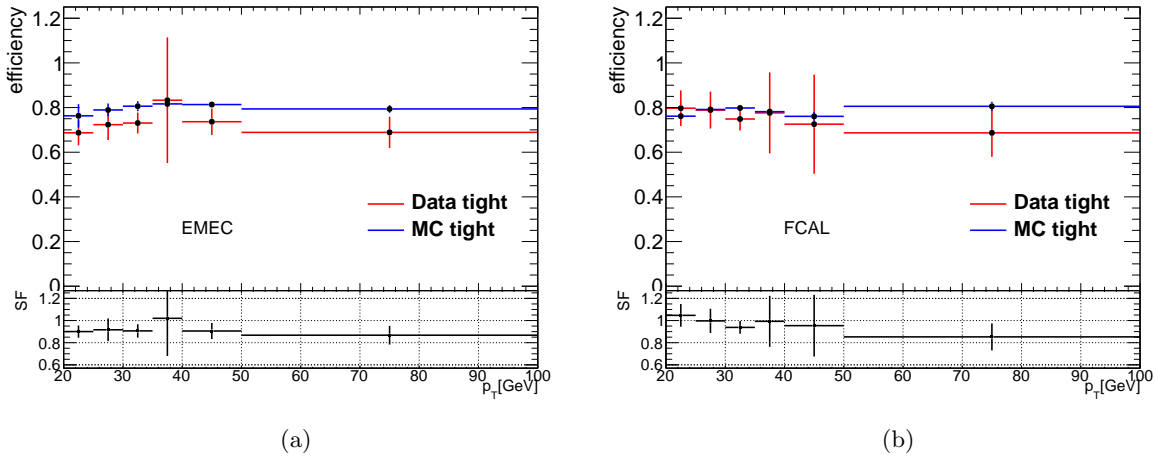


Figure 4.16: Identification efficiencies as function of p_T with new tight identification. EMEC (a) and FCAL (b).

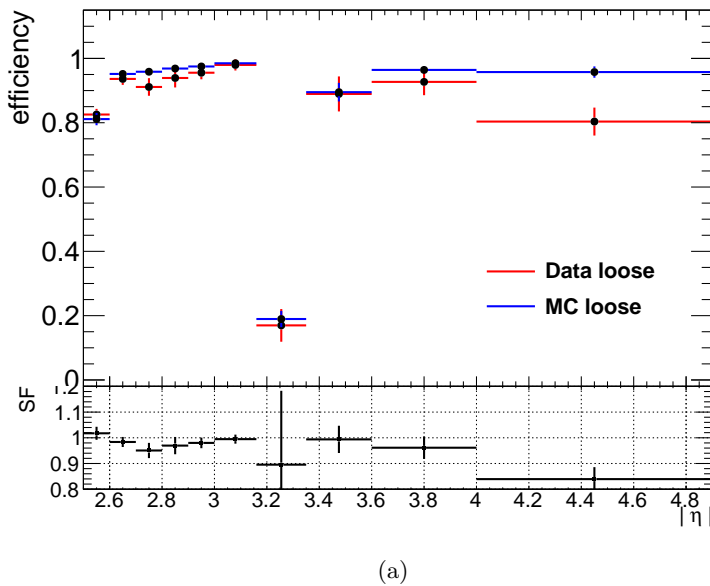


Figure 4.17: Identification efficiencies in $|\eta|$ bins. New loose identification.

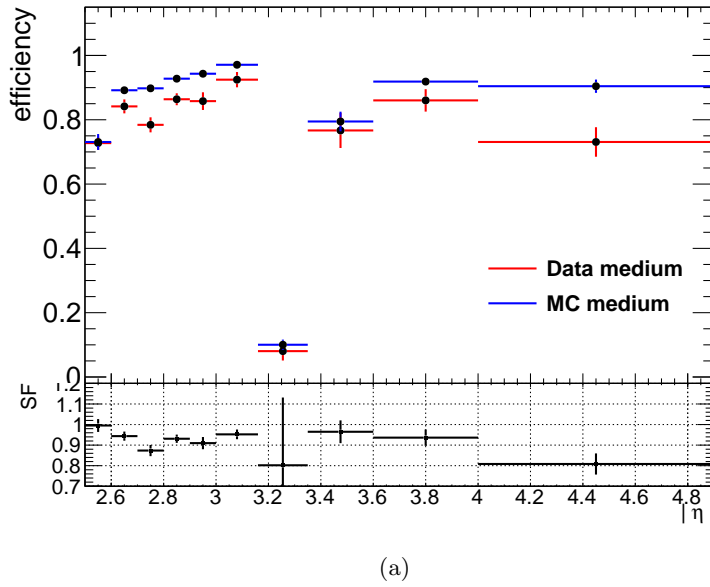


Figure 4.18: Identification efficiencies in $|\eta|$ bins. New medium identification.

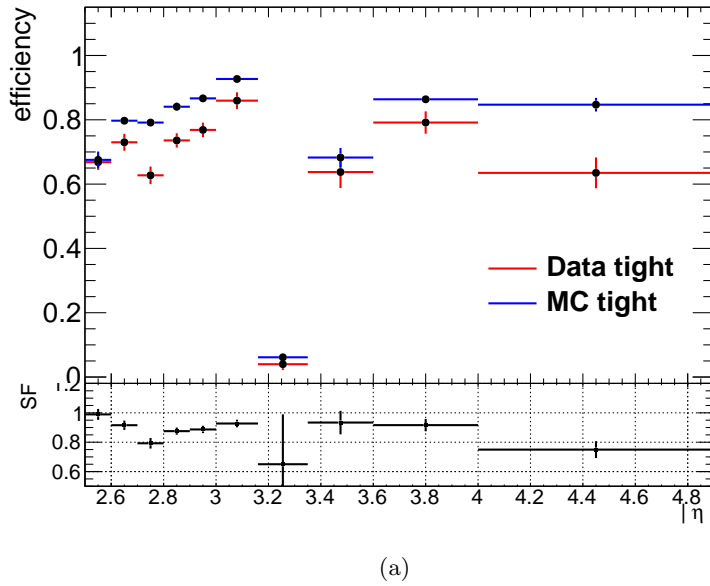


Figure 4.19: Identification efficiencies in $|\eta|$ bins. New tight identification

4.4 Discussion and Outlook

The identification of electrons with high values of the pseudorapidity represent a demanding task, due to the lack of covering of the track system at this regions. In the present chapter, a

description of the methods used to identify the central, and particularly the forward electrons was given. The dependency of the forward electron identification on the different data taking periods was shown, as was the implementation of the menu optimization and correction of the observed identification using data analysis.

The work made for the ATLAS collaboration led to use the forward electron in present analyses, an example is the ZZ analysis. Previous measurements of the diboson production cross section, didn't use the forward region of the electromagnetic calorimeter, or only a part of the forward calorimeter. In the next part of this work, the use of forward electrons in the ZZ analysis is presented.

Chapter 5

$ZZ \rightarrow 4e$ Events in the 2012 ATLAS Data

“There are three kinds of people, those who can count and those who can’t.”
—Homer Simpson

In chapter 2, it was mentioned that the study of the production cross section of ZZ is important to test the electroweak sector of the Standard Model (SM). Diboson production via a triple neutral vertex is one of the prospects to find new physics. For that reason, a precise measurement of the diboson production cross section is important to put limits to the range of validity of the SM.

This chapter will offer a description of the methodology used to search for ZZ candidates in ATLAS data collected in year 2012 at a center of mass energy of $\sqrt{s} = 8$ TeV, corresponding to an integrated luminosity of $\mathcal{L} = 20.3 \text{ fb}^{-1}$. Also, different background sources that affect these processes and their treatment are discussed. At the end of the chapter, a comparison of kinematic variables of the diboson candidates found in the 2012 data with MC simulations is given.

5.1 Diboson Event Selection

The leptonic decay of ZZ is characterized by the production of four isolated leptons few physical processes possess the same final state signature; for that reason, the $ZZ \rightarrow 4\ell$ is an almost free background process. This work is focused on diboson events with four electrons in final state. The major background contribution to this process consists of events with real electrons and jets that can fake the signal of electrons in the calorimeters and tracking system.

This section offers a general description of the selection criteria applied to the proton-proton collision data, in order to get a sample of electron candidates to be analyzed. The reconstruction

of ZZ candidates in the selected sample is explained and the final number of diboson candidates found is shown.

5.1.1 Data Selection

The data selection applied in the ZZ analysis can be divided into three steps. The first one consists of the selection of events to be further analyzed, based on the integrity of the recorded data. The second part is an object identification in the selected events, where the objects in this case correspond to electrons. The last part of the data selection corresponds to the reconstruction of Z pairs from the electron candidates found in the second step. In the following part of this section, a detailed description of each data selection step is presented.

1. Event selection

In the event selection, some characteristics of the data-taking conditions are used as discriminators to define a good event. Optimal beam conditions and operational behavior of each ATLAS subdetector are parameters to take account of in order to discard background sources like cosmic rays (number of primary vertex) or noise coming from the electronic (LAr and Tile monitoring). Apart from the data-taking conditions, the selected events must be triggered for specific energy and object thresholds.

Two triggers for electrons are used in this analysis, corresponding to the unrescaled lowest threshold triggers: One trigger requiring electrons with p_T larger than 24 GeV (EF_e24vhi_medium1¹) and one requiring electrons with p_T larger than 60 GeV (EF_e60_medium1) were used. Both triggers required one electron with medium identification and additionally the 24 GeV required an isolation criterion ($p_T^{cone20}/p_T < 0.1$) on the p_T of the electron and one veto on the energy deposited for the triggered object in the hadronic calorimeter.

ATLAS Definition	Description
GRL	Beam conditions and data quality.
Trigger	Lowest threshold electron triggers.
Primary vertex	Primary vertex with at least 3 associated tracks.
Event cleaning	Integrity of the data collected by the LAr.
Data corruption	Tile calorimeter information free of data corruption.

Table 5.1: Summary of the event selection used in the ZZ analysis.

The reason for the usage of the two set of cuts in the triggered objects is to reduce a loss of efficiency at high energy electrons. Single triggers are preferred over double object triggers

¹The ATLAS trigger naming convention is:
(trigger level)_(number of objects)(type of object)(threshold)_(quality criteria)

in order to avoid a loss of statistics. In table 5.1, a summary of the event selection criteria is given.

2. Object selection

Events that fulfill the requirements shown in table 5.1 are further examined. Electrons candidates in the events are reconstructed in the central ($|\eta| < 2.47$) and forward region ($2.5 < |\eta|$). The candidates are then filtered using identification criteria and, in the case of central candidates, track quality requirements.

As already mentioned at the beginning of this section, isolated leptons are signatures for ZZ process. For that reason, a track isolation (see 4.2.3) requirement is applied on the central electrons. Any further isolation criteria are used in the case of forward electrons.

If two selected electrons in the event overlap in a cone $\Delta R = \sqrt{\Delta\eta^2 + \Delta\phi^2} < 0.1$, the electron with the lowest p_T is removed from the selection. Electrons passing the previous lepton candidates selections are called good electrons and only events with exactly four good central candidates are further considered.

In the table 5.2, a list of the object selection requirements is provided with cut values.

	Central electron	Forward electrons
Reconstruction	author 1 or 3	author 8
Energy	$p_T > 7$ GeV	$p_T > 20$ GeV
η acceptance	$ \eta < 2.47$	$2.5 < \eta < 3.16$ or $3.35 < \eta < 4.9$
Identification	multilepton	loose forward
Longitudinal impact parameter	$ z_0 \times \sin \theta < 0.5$ mm	
Transverse impact parameter	$\frac{ d_0 \times \sin \theta }{\sigma(d_0)} < 6$	
Isolation	$\sum \frac{p_T^{Track}(\Delta R < 0.2)}{p_T^{Track}} < 15\%$	

Table 5.2: Criteria used in the ZZ analysis to select electron candidates.

3. ZZ reconstruction

With the electrons found in the selected events, as described in the previous section, a ZZ reconstruction procedure is done to determinate the final number of ZZ candidates. At least one of the selected electrons should match a trigger object, meaning that one of the selected electrons should be in a cone $\Delta R < 0.1$ of one trigger object. The match electron should have a p_T 1 GeV over the p_T trigger threshold and fulfill tighter identification criteria.

In order to build the Z pairs, two steps are followed:

- Opposite charge: If possible, only pairs of electrons are considered when they have opposite charge. That would not be the case for events with one good forward electron; in this case, all the possible combinations with the forward electron are considered.
- Pairing algorithm: With the combination of previously found pairs the invariant mass of the two electrons is calculated and the absolute difference with respect to the mass of the Z is obtained. The sum of the difference is calculated and the smaller sum involving different electrons is taken as the correct pair.

An additional requirement in events with forward electron is used to reduce background contamination. It consists of a cut on the p_T of the central partner of the forward electron. The transverse momentum of the central electron should be larger than 20 GeV.

Only real Z 's are further considered in the analysis, so reconstructed bosons with invariant mass in the range 66 to 116 GeV are also taken into account. With the selection described above, a total of 64 ZZ candidates were found in the 2012 data sample. Table 5.3 shows the number of candidates in each calorimeter region. The number of ZZ candidates with four central electrons corresponds to 54. In the table, the effect of different identification criteria in the selection of forward electrons can be seen in the last column.

	Four central electrons	Three central and one forward electron
Forward loose	54	10
Forward Medium	54	8
Forward Tight	54	6

Table 5.3: Number of ZZ candidates in 2012 data. The effect of different forward identification criteria in forward electrons is shown.

To finalize this section, a representation of two events with ZZ candidates is offered. One of the selected events consists of four central electrons and the second is an event with three central electrons and one forward.

In figure 5.1, a ZZ candidate with an invariant mass of 170 GeV is represented. The left side of the figure shows the electromagnetic calorimeter in blue. The tracks of the electrons are visible in the inner part of the figure. The red tracks correspond to negatively charged electrons and the green ones to the tracks of positive electrons. The energy deposited by each particle in the calorimeter is represented in yellow. On the right side of the figure, a frontal view of the same event is shown. Only the components of the inner detector are presented. The tracks of the electrons can be seen clearly here, too.

In figure 5.2 a ZZ candidate with three central electrons and one forward is shown. The left side of the figure shows the tracks of the particles in the inner detector. Only three tracks are

visible, two in green, corresponding to positrons and one in red corresponding to one electron. The fourth track is not visible because it corresponds to the forward electron and, as already mentioned, for these electrons, there is no information of the inner detector. The energy deposits for the four particles are shown in yellow. The energy deposit of the forward electron, almost parallel to the beam pipe, can be seen. The right side part of the figure shows a frontal view of this event; only the inner detector components are shown. In this case, tracks and energy deposits are visible too. The invariant mass of the ZZ is, in this case 226 GeV.

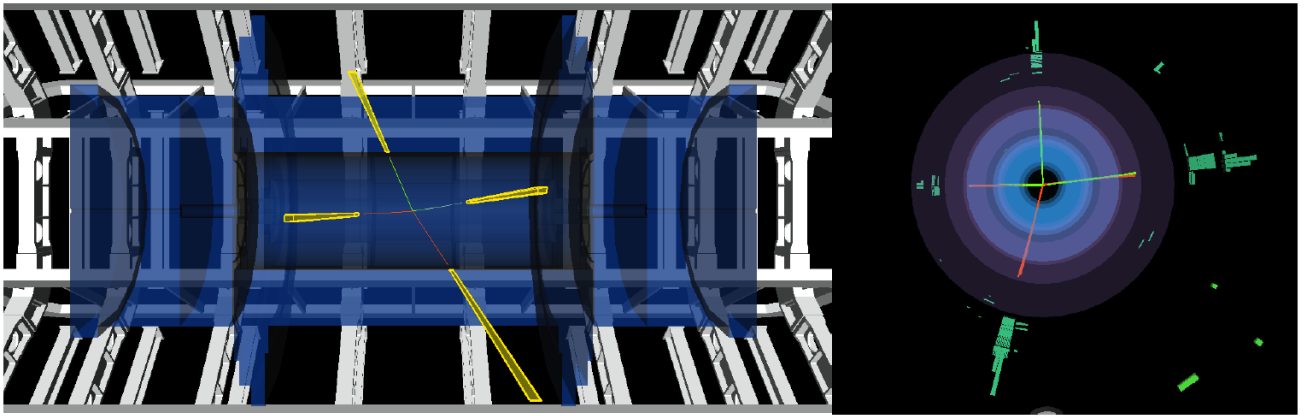


Figure 5.1: ZZ candidate with four central electrons. The left side of the figure shows the tracks and energy deposits of the electrons in the electromagnetic calorimeter. The right side shows a frontal view of the event, only inner detector components are visible. (RunNumber: 214160, EventNumber: 81925870)

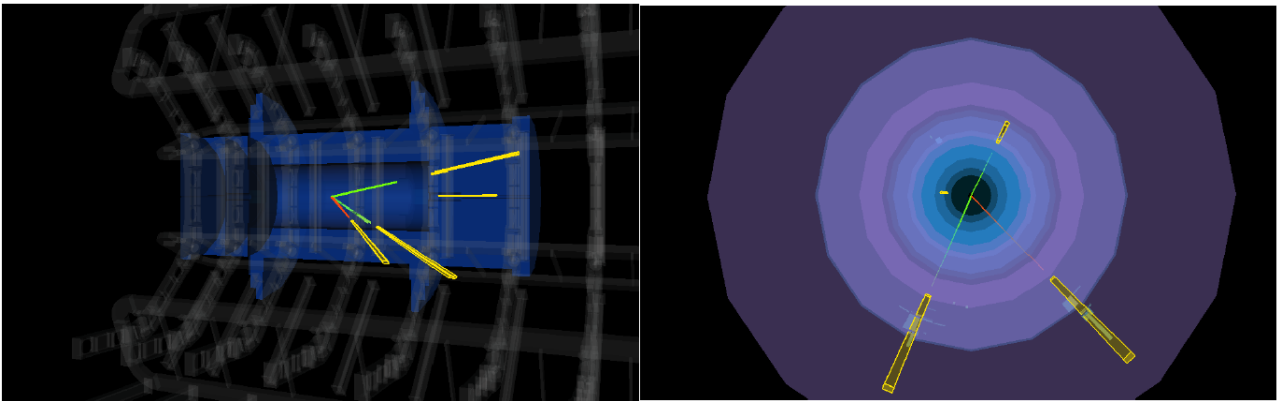


Figure 5.2: ZZ candidate with three central electrons and one forward. The left side of the figure shows the tracks and energy deposits of the electrons in the electromagnetic calorimeter. The right side shows a frontal view of the event, only inner detector components are visible. (RunNumber:214544; EventNumber: 96882558)

5.2 MC Signal and MC Backgrounds

Monte Carlo (MC) simulations are powerful tools in particle physics in order to make an optimization of the different elements involved in a physics analysis involving many particles.

For example, in order to have an idea of the number of events that could be expected in the analysis of the production of dibosons, different samples, that simulate the production of ZZ pairs and the performance of the detector to find the products of the decay of neutral bosons, are prepared. Processes with real electrons in the final states are used, too, in order to have an idea of the background contribution to the analysis, but due to the lack of statistics in some cases, background predictions based on data-driven methods can also be used.

In chapter 2, a description of the MC generators and Parton Density Functions (PDF), used in this analysis and the detector simulation, was given. In appendix A, a description of the MC samples used in this analysis is provided.

In the next section, a description of the MC correction applied in this analysis is described and the different MC samples used are explained.

5.2.1 MC Corrections

A better understanding of the ATLAS detector, after the two years of operation, allows a refinement of the detector simulation. An example is the actual knowledge of the material distribution in the detector, that affects the energy resolution and calibration. In that way, corrections to the MCs predictions can be obtain from the data to make a correct Data-MC comparison. Below, a list of the MC corrections, derived from data used in this analysis, is given.

- Pileup Reweighting:

The number of hard interactions during data taking depends on certain parameters of the proton-proton collisions; e.g., the number of protons per bunch, the spatial and time separation between bunches. For that reason, a reweighting method should be introduced in the MC samples, where the distribution of the mean interactions per beam crossing (NPV) observed in the data is used to scale those of the MC. A general description of the tool can be seen in [46].

- Energy smearing:

The energy resolution of the calorimeters is determined by detector characteristics like the amount of material in front of the calorimeters or the geometry of the calorimeter. For that reason, the modeling of the resolution in the MC simulations is more complicated. A smearing procedure is applied on the MC energy of the objects, where the corrections are

derived from the data. A description of the implementation of the energy corrections is offered in [47].

- Scale factors:

In the previous chapter (see 4.3), the necessity to use of scale factors (SF) to correct the differences between the efficiency of the identification of electrons observed in data and the prediction from MC was shown. Similar SFs are necessary to cover the differences in the reconstruction efficiency of candidates and the trigger selection efficiency. Additionally, SFs for some parameters used in this analysis, like the calorimeter isolation and the parameter of impact selection, are also applied as corrections to the MC. A description of the general strategy to get SFs in ATLAS can be consulted in [44].

The corrections listed above are applied to the MC simulation to make a comparison with the data. The MC that simulate the ZZ production in this analysis consists of two different generators. The `PowhegPythia` [29] simulates the production of ZZ via quark-antiquark interaction. ZZ produced via gluon-gluon fusion ($\approx 6\%$) is simulated using `ggVV` [30].

In chapter 2, a description of the major background processes for ZZ events was given. The background sources can be separated into two principal classes:

- Irreducible background: composed of the product of processes like ZZZ^* , ZWW or $t\bar{t}Z$, which have leptonic final states with four real electrons. The generator available for the simulation of this process is *madgraph* [32].
- Reducible background: Processes with two real electrons and a variable number of jets that can fake the electron signatures in the calorimeters. That is the case of Z +Jets, $Zb\bar{b}$, top decays ($t\bar{t}$ and single Top). These processes can contain two real electrons and two jet-faking electrons or not-isolated leptons from heavy flavour decay. WZ +Jets events are the source of background in these cases, with three prompt electrons and one fake lepton [19]. Processes with Z + Jets are simulated using `ALPGEN` [33]; WZ +jets with the `PowhegPythia` and top events were modeled with `MC@NLO` [31].

Table 5.4 shows the expected number of events predicted for the different sources of background and the MC signal. Only statistical uncertainties are presented.

As can be seen in table 5.4, the numbers corresponding to irreducible backgrounds are in some cases zero (Z +Jets and Top) or possess big statistical uncertainties. For that reason, a different approximation is used in this analysis to obtain the background in the case of jets-faking electrons. Sources of background with at least one fake candidate are studied using a data driven method that will be explained in the following section.

	Only central electrons	One forward electron
PowhegPythia + ggVV	50.3 ± 0.3	12.0 ± 0.1
$ZZZ^*/ZWW/t\bar{t}Z$	0.2 ± 0.1	0.03 ± 0.02
Z+Jets	0.0 ± 0.0	7.4 ± 6.4
WZ+ Jets	1.1 ± 1.0	1.5 ± 1.4
$t\bar{t}$ and single top	0.00 ± 0.00	0.02 ± 0.09
Higgs	0.00 ± 0.00	0.001 ± 0.0002

Table 5.4: Number of expected ZZ candidates in proton-proton collisions for a center of mass energy of $\sqrt{s} = 8$ TeV normalized to $\mathcal{L} = 20.3 \text{ fb}^{-1}$. Different sources of background are considered. Only statistical uncertainties are shown.

5.3 Data Driven Background Estimation

Data driven methods represent a good alternative to the use of MC simulations in studies where the total number of events that can be produced for the MC is low, or when the modeling of some of the properties is too hard to be simulated or not well understood. In the case of background studies using this data driven method, it is necessary to determine the probability of identification of a background candidate as a real candidate. For that reason, the standard selection is loosened or inverted to create a sample of candidates with high background contamination and to see how many of the fake candidates are seen at the end of one particular analysis.

There are different strategies to perform background studies using inversion selection. In the case of diboson production, the so-called matrix method is used. In the following section, a description of the matrix method is given.

5.3.1 Matrix Method

The principle behind the matrix method is the possibility of make a correspondence between the inaccessible true information, represented through the real leptons (R) and the real non-leptons (F) and the measured objects, i.e., lepton candidates (L) and jet candidates (J).

Due to the measurement procedure there is a probability r to measure one real lepton R as one lepton candidate L; similarly, one non-lepton F can be measured as a lepton candidate L with a probability f . r is referred to as efficiency and f is named fake rate.

In the case of the ZZ analysis, the total number of measured candidates of one class; e.g., N_{LLLL} , N_{LLLJ} , N_{LLJJ} , etc, can be written as a linear combination of the number of N_{RRRR} , N_{RRRF} , N_{RRFR} , ..., N_{FFFF} , with coefficients resulting of the product of r , f , $1 - r$, $1 - f$, etc.

The relation between all the possible combinations can be written in a matrix form as:

$$N^{Meas} = MN^{Real} \quad (5.1)$$

where M is a 16×16 matrix and N^{Meas} and N^{Real} are vectors with the numbers of measured events and the real quantities respectively. The elements of M are the product of r , f , $1 - f$ and $1 - f$ of each object.

With the help of symmetry properties, the size of the matrix can be reduced. For example, if the number N_{LLJJ} is equivalent to N_{JJLL} or N_{LJLJ} or N_{LJLJ} .

In case of dibosons with three central electrons and one forward electron, the background can be considered due to the presence of one jet in forward region J_f , one jet in central region J_c or two jets one in central region and one in forward $J_c J_f$. Considering all cases the matrix M can be written as:

$$M = \begin{pmatrix} r_c^3 r_f & r_c^3 f_f & r_c^2 r_f f_c & r_c^2 f_f f_c \\ r_c^3 (1 - r_f) & r_c^3 (1 - f_f) & r_c^2 f_c (1 - r_f) & r_c^2 f_c (1 - f_f) \\ r_c^2 (1 - r_c) r_f & r_c^2 (1 - r_c) f_f & r_c^2 (1 - f_c) r_f & r_c^2 f_f (1 - f_c) \\ r_c^2 (1 - r_c) (1 - r_f) & r_c^2 (1 - r_c) (1 - f_f) & r_c^2 (1 - f_c) (1 - r_f) & r_c^2 (1 - f_c) (1 - f_c) \end{pmatrix}$$

Making easy to notice, that if $r_c = r_f = r = 1$, the matrix can be written as:

$$\begin{pmatrix} 1 & f_f & f_c & f_f f_c \\ 0 & 1 - f_f & 0 & f_c (1 - f_f) \\ 0 & 0 & 1 - f_c & f_f (1 - f_c) \\ 0 & 0 & 0 & (1 - f_f) (1 - f_c) \end{pmatrix}$$

With help of this relation, it is possible to write an equation for the $N_{L_c L_c L_c L_f}$, as a function of the true elements with at least one fake F object. The equation is shown below:

$$N_{back}^{forw} = f_f \times N_{R_c R_c R_c F_f} + f_c \times N_{R_c R_c F_c R_f} + f_f \times f_c \times N_{R_c R_c F_c F_f} \quad (5.2)$$

To solve the previous equation, it is necessary to find an expression for the $N_{R_c R_c R_c F_f}$, $N_{T_c T_c F_c T_f}$ and $N_{T_c T_c F_c F_f}$ as function of the quantities that can be measured with the detector. To do that, the matrix M should be inverted.

After the inversion, the background equation 5.2 for three candidates in the central region plus one forward can be written as:

$$N_{back}^{forw} = \frac{f_f}{1 - f_f} \times N_{L_c L_c L_c J_f} + \frac{f_c}{1 - f_c} \times N_{L_c L_c J_c L_f} - \frac{f_f}{1 - f_f} \times \frac{f_c}{1 - f_c} \times N_{L_c L_c J_c J_f} \quad (5.3)$$

A similar expression can be derived from the background, corresponding only to electron candidates in the central region, using the same $r = 1$ approximation. The equation 5.3 can be modified taking $f_f = f_c$, $L_f = L_c$ and $J_f = J_c$. The equation is shown below

$$N_{back}^{central} = \frac{f_c}{1-f_c} \times N_{L_c L_c L_c J_c} + \frac{f_c}{1-f_c} \times N_{L_c L_c J_c L_c} - \frac{f_c}{1-f_c} \times \frac{f_c}{1-f_c} \times N_{L_c L_c J_c J_c} \quad (5.4)$$

The two first terms of the equation above are similar, but the position of the J_c is different. Due to combinatorics, the final expression for the background in the central region is:

$$N_{back}^{central} = \frac{f_c}{1-f_c} \times N_{L_c L_c L_c J_c} - \left(\frac{f_c}{1-f_c}\right)^2 \times N_{L_c L_c J_c J_c} \quad (5.5)$$

The values $FF_f = \frac{f_f}{1-f_f}$ and $FF_c = \frac{f_c}{1-f_c}$ are called Fake Factors. With this definition, the final equations for the background are shown below:

$$N_{back}^{forw} = FF_f \times N_{L_c L_c L_c J_f} + FF_c \times N_{L_c L_c J_c L_f} - FF_c \times FF_f \times N_{L_c L_c J_c J_f} \quad (5.6)$$

$$N_{back}^{central} = FF_c \times N_{L_c L_c L_c J_c} - (FF_c)^2 \times N_{L_c L_c J_c J_c} \quad (5.7)$$

In the next section, a description of the estimation of the Fake Factors (FF) is provided.

5.3.2 Fake Rate Estimation

In the previous equations (5.7 and 5.6), the L_i and J_i categories correspond to candidates that pass or fail a set of cuts. The candidates that belong to the J_i group are called jet-like leptons and they are candidates that do not pass the full selection applied in the analysis. The L_i type are well identified candidates. As shown before, the standard selection of candidates includes identification (multilepton) plus isolation requirements for the central candidates. Candidates in the forward region should pass the loose forward identification criteria. A summary of the criteria of L_i and J_i types are shown in the next table (5.5).

	Central electrons	Forward electron
Lepton like type	multilepton + isolation	loose forward
	fail multilepton + isolation	
Jet like type	or	fail loose forward
	multilepton + fail isolation	

Table 5.5: Criteria to classified electron candidates as lepton-like or jet-like in the central and forward region.

With the definitions given above, it is now possible to write more explicitly the equations for the fake rates and fake factors.

$$f_i = \frac{L_i}{L_i + J_i} \quad (5.8)$$

$$FF_i = \frac{L_i}{J_i - L_i} \quad (5.9)$$

The FF should be determined for central and forward electrons as a function of p_T and η . In order to calculate the fake factors, a reverse tag and probe method is implemented over the preselected candidates ($L_i + J_i$) to have a pure sample of fake candidates. The inverse tag and probe method takes only pairs of candidates beyond of the Z peak $|M_{ee} - M_{ZPDG}| > 20$ GeV, the event should pass the trigger requirement and have a MET < 25 GeV. The anti-tag candidate should fail the identification and, in the case of central candidates, fail the isolation criteria too. With these selections, the number of probe candidates passing the full selection over the number of preselected probe candidates are used to calculate the fake factor.

The average fake factors for central and forward electrons are shown in the table 5.6. With the help of this average values, the statistical and systematic uncertainties of the background determination, using the matrix method, will be calculated.

	Central electrons	Forward electron
FF average	0.043 ± 0.003	0.048 ± 0.005
LLLJ	62.0 ± 7.9	44.0 ± 6.6
LLJJ	482.0 ± 21.9	1041.0 ± 32.3
LLJL _f	–	62.0 ± 7.9

Table 5.6: Average FF in p_T and η for central and forward electrons. The elements used in the equations 5.7 and 5.6 can be seen too. Only statistical uncertainties are shown.

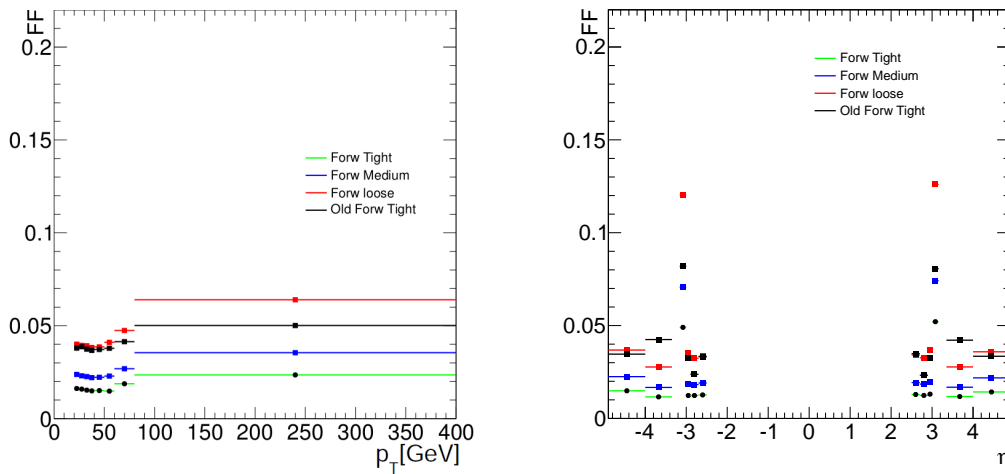


Figure 5.3: The figure shows the fake factors of forward electrons comparing the effect of different identification criteria and new and old tight forward menu. On left side plot, the behavior as a function of p_T is shown. The right side plot shows the η behavior.

In figures 5.3 and 5.4, the fake factors of forward and central electrons as function of p_T and

η are shown. The effect of different forward identification criteria can be seen in the figure 5.3; the more loose the identification the higher the fake factor. As can be seen, the new forward identification discussed in 4.3.3 improves the background rejection because the fake factors with new loose forward identification are closer to the fake factors with old tight forward identification. In the case of the fake factors for the central electrons (fig. 5.4), the distribution as function of η is flatter compared with the same distribution in the case of forward electrons (as shown in the right side of figure 5.3). The distribution of the fake factors as function of p_T is very similar for the central and forward electrons. The different thresholds on the p_T -in central and forward regions- can be seen.

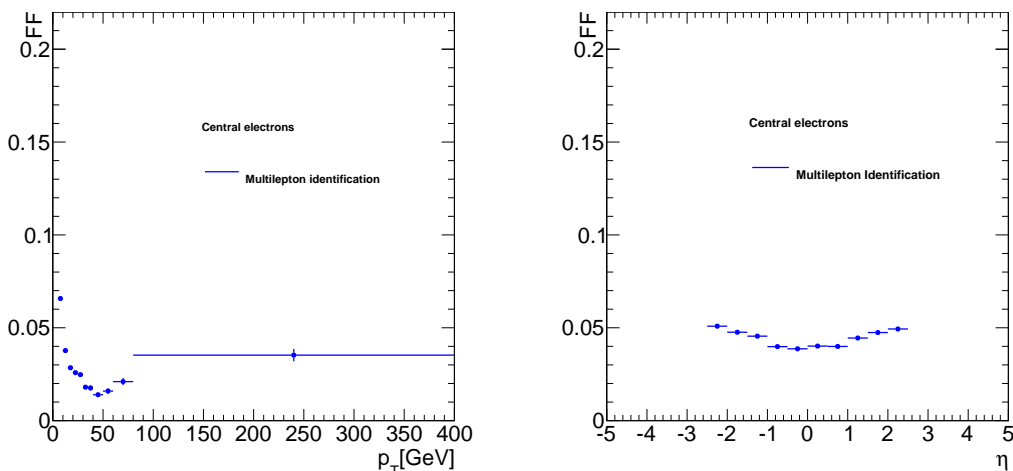


Figure 5.4: Fake factors of central electrons. On the left side of figure, the behavior as a function of p_T is shown. Right side of the figure shows the η behavior.

With help of the equations 5.5 and 5.3 and the fake factors, calculated using the inverse tag and probe, the values of the background obtained using the data driven method are shown in the table below :

	Four central electrons	Three central and one forward electron
Background DD	1.5 ± 0.4	2.9 ± 0.5

Table 5.7: The table shows the background estimation for the data driven method. Only statistical uncertainties are shown.

The statistical uncertainties shown in the table 5.7 are obtained running a series of pseudo-experiments, where the FF factor was assumed to belong to a Gaussian function around the average FF given in the table 5.6 and the elements in the equations 5.5 and 5.3 were selected from a Poisson distribution with a mean equal to the nominal values given in the table 5.6 for the LLLJ, LLJJ and LLJL_f.

5.4 Systematic Uncertainties to the Background Estimation

In the previous section, the background predictions for the ZZ production were derived in two ways. For the case of irreducible background, a MC based prediction was used; for the process with at least one fake candidate, a data driven method was used. For that reason, the systematic uncertainties are calculated using two different methods: In the case of irreducible background, that is MC derived, the uncertainties are calculated through variation on the SF used to correct the MC. In the case of the data driven method, a simple comparison with the values given for the average FF is used as a measurement of the systematic uncertainties.

In the next sections, the calculation of the systematic variation is described in more detail.

5.4.1 MC Systematic Uncertainties Estimation

As shown in section 5.2.1, smearing of the energy and scale factors (SFs) to correct inefficiencies of the MC simulations are necessary to make a correct Data-MC comparison. There are SFs that correct the reconstruction, identification, trigger selection and the efficiency of the isolation variables. The SFs and energy smearing used in this work are provided by the ATLAS collaboration. Systematic variations of the SFs and smearing can be applied to the MCs in order to make a propagation of the uncertainties.

Variations of the central value are obtained by the SFs using the systematic uncertainties of the latter and the energy smearing of each of the corrections. The absolute differences with the mean value are then calculated and the larger difference is used as the uncertainty related to the respective correction.

ZZ MC	Four central electrons	Three central and one forward electron
Nominal \pm Stat.	50.3 ± 0.3	12.0 ± 0.1
Energy	± 0.6	± 0.3
Identification	± 0.9	± 0.3
Isolation	± 0.5	± 0.05
Reconstruction	± 0.4	± 0.8
Trigger	± 0.03	± 0.002
Total	± 1.3	± 0.4

Table 5.8: Absolute systematic variations to the ZZ MC due to the SF and energy uncertainties.

Table 5.8 shows the value of the different variations over the ZZ MC signal; the total systematic uncertainty is calculated as the square root of the quadratic sum of each variation. As can be seen, the principal contribution to the systematic for central electrons comes from the identification correction. In the channel with one forward electron, the energy correction is

the principal source of uncertainty.

Similarly, the total absolute systematic variations for the irreducible sources of background are shown in 5.9.

	Four central electrons	Three central and one forward electron
ZWW	± 0.006	± 0.004
ZZZ^*	± 0.002	± 0.001
$t\bar{t}Z$	± 0.012	± 0.0001
Total Irr	± 0.01	± 0.004

Table 5.9: Absolute systematic variations to the irreducible background due to the SF and energy uncertainties.

5.4.2 Systematic Uncertainties for the Data Driven Background

In the case of the data driven method a more simple way to determinate the systematic variation was made. The idea consisted of taking the average fake factors and the total values of candidates with fake candidates and calculating a global prediction.

The difference with the central value calculated with the full p_T and η distribution of FF is taken as the absolute systematic uncertainty [48].

	Central value	Average value	Difference
Four central electrons	1.5	1.4	± 0.03
Three central and one forward electron	2.9	2.4	± 0.5

Table 5.10: Absolute systematic variations to the irreducible MC due to the SF and energy uncertainties.

As can be seen in the table 5.10, the total absolute systematic uncertainty for central electrons corresponds to ± 0.03 and, in the case of ZZ candidates with one electron in the forward region, ± 0.54 . The table 5.11 shows a summary of the background contributions with the respective absolute statistical and systematic uncertainties.

	Four central electrons	Three central and one forward electron
ZZ MC \pm (Stat.) \pm (Sys.)	$50.3 \pm 0.2 \pm 1.2$	$12.0 \pm 0.1 \pm 0.3$
Irr background \pm (Stat.) \pm (Sys.)	$0.20 \pm 0.09 \pm 0.01$	$0.030 \pm 0.020 \pm 0.001$
DD background \pm (Stat.) \pm (Sys.)	$1.5 \pm 0.2 \pm 0.03$	$2.9 \pm 0.5 \pm 0.5$

Table 5.11: Total background predictions. Absolute statistical and systematics uncertainties are shown.

5.5 Data-MC Comparison

This section is dedicated to a comparison between data and MC of different kinematic variables. In order to understand the effect of the forward electrons in the ZZ analysis, two categories of events are considered depending on the presence of forward electrons. Z pairs with all four electrons, detected in the central region, are marked as CCCC, and in the case of one electron with high values of η , the events are called CCCF events.

Data driven background (DD Back.) and irreducible background are shown together with the signal MC expectation. In all plots shown below, the MCs are normalized to the integrated luminosity of $\mathcal{L} = 20.3 \text{ fb}^{-1}$.

5.5.1 Electron Kinematic Variables

The angular and p_T distributions of the electrons product of the decay of ZZ candidates are shown in the following figures. A separate contribution of CCCC and CCCF events is shown. Additionally, in order to study the performance of the forward electrons, the analyzed kinematic distributions in CCCF events are shown separately for electrons in the central region and forward electrons.

As already mentioned, the background sources to the ZZ analysis consist principally of misidentified jets. For that reason, the larger component of the background showed in the following plots consist of the data driven method (DD Back.) used to calculate this background. The contribution of the irreducible background is small; for that reason, it is sometimes not visible in the shown distributions.

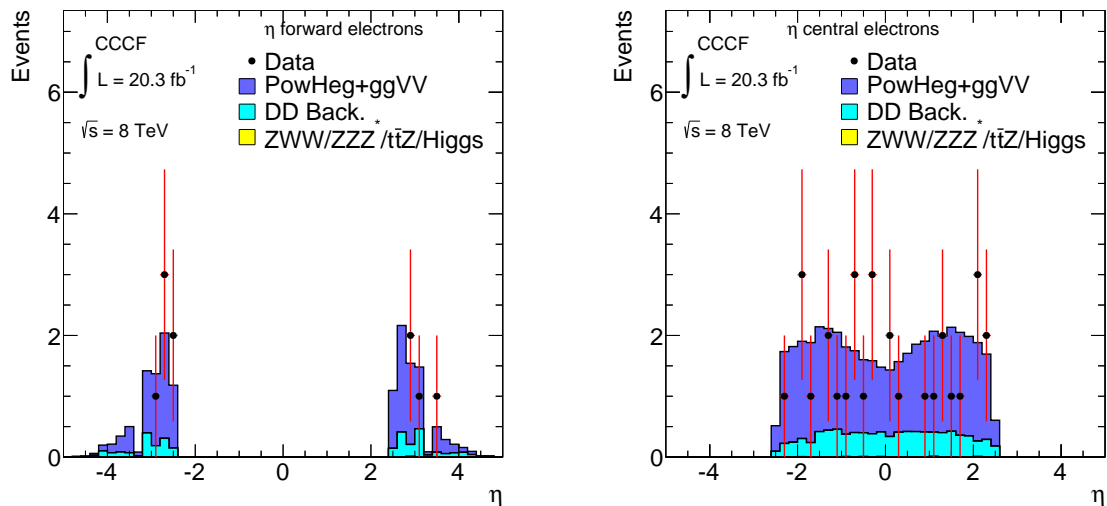


Figure 5.5: η distributions of electrons coming from ZZ candidates with three central and one forward electron. On the left side of the figure, the η distribution of the forward electrons is visible. The right side shows the pseudorapidity distribution of the central electrons.

In figure 5.5, the distribution of the η variable for electron in CCCF events is shown. On the left side of the figure, the eta distribution of the forward events in these events can be seen. The 90% of the forward electrons are found in the EMEC part of the forward calorimeter, the remaining 10% is in the FCal. However, the MC prediction for number of electrons in this region, as can be calculated from the MC signal (blue curve) in the figure, is around two forward electrons in the FCal, so the number of events in the data is in agreement with the MC expectation.

The right side of figure 5.5 shows the η of the central electrons in CCCF events. A uniformed distribution of the electrons as a function of the η variable is visible. The Data-MC agreement is good for the shown distribution, too.

The p_T of the electrons in CCCF events is shown in figure 5.6. Similarly as with η , the p_T distribution is presented separately for the forward electrons on the left side of the figure and for central electron only, in the right side. For the forward electrons, the minimal p_T requirement of 20 GeV is clearly visible. In the case of the central electrons of the CCCF events, the minimal p_T is 20 GeV, too, since in the selection of events with forward electrons, the partner of the forward electron should have a p_T larger than these value. As observed from the MC signal, central electrons with p_T smaller than 20 GeV are expected. However, no such events of these can be seen in the plots.

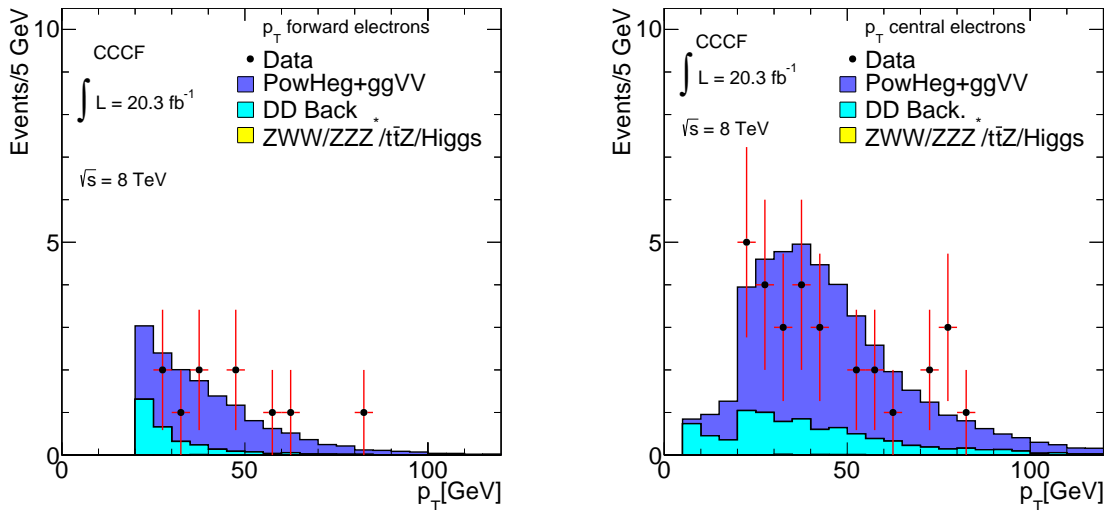


Figure 5.6: p_T distributions of electrons coming from ZZ candidates with three central and one forward electron. On the left side of the figure, the η distribution of the forward electrons is visible. The right side shows the pseudorapidity distribution of the central electrons.

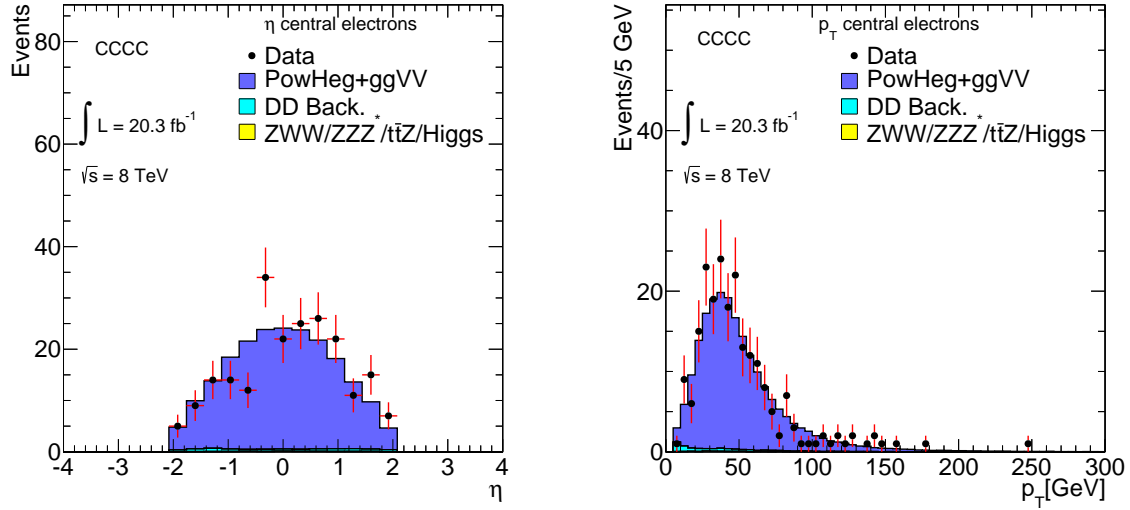


Figure 5.7: η (left side) and p_T (right side) distribution of electrons coming from ZZ candidates with four central electrons.

In the case of events with four central electrons (CCCC events), the η and p_T distributions of the electrons are shown in figure 5.7. The η distribution of the electrons can be seen on the left side of the figure. Data-MC agreement is good, considering the uncertainties, except for some statistical fluctuation in the η range -0.08 to -0.05 . In the case of the p_T distribution, the agreement is better.

5.5.2 ZZ Kinematic Variables

In the remaining part of this section, kinematic distributions of the Z and ZZ candidates found in data are compared to MC prediction for the distributions. As in the above part of this section, the ZZ events are separated into the two mentioned categories, CCCC and CCCF event. As already mentioned, the goal of this separation is to better understand the impact of the use of the forward region in the study of the production of Z pairs.

figure 5.8 and 5.9 show the invariant mass and the transverse momentum of the Z with the highest p_T , referred to as leading Z . The left side of both figures shows the distribution for the CCCC events, while the right side presents the corresponding distribution in CCCF events.

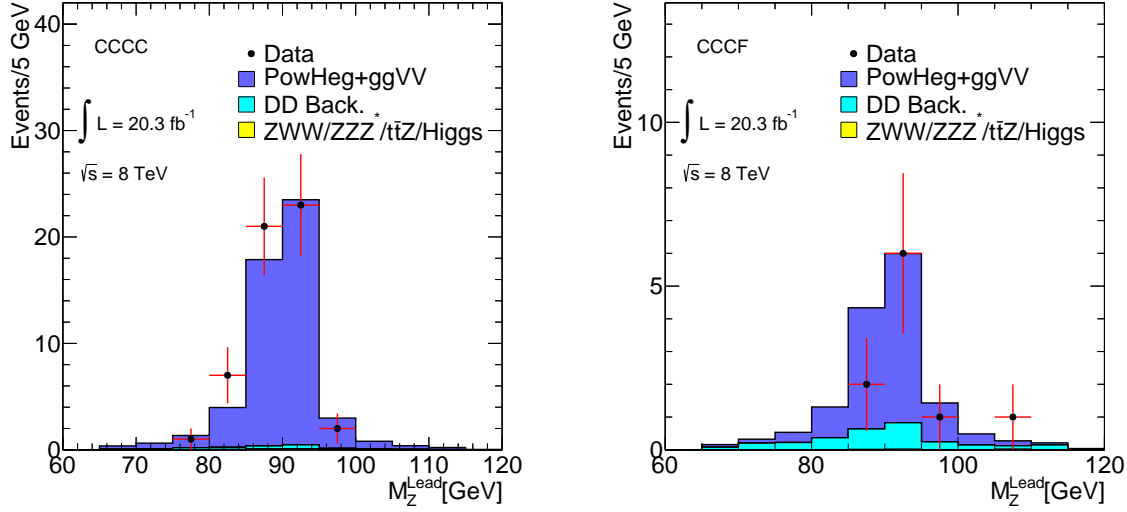


Figure 5.8: Invariant mass of the Z candidate with the larger p_T (leading Z). The left side shows events with four central electrons. The right side shows candidates with one forward electron and three centrals.

The good Data-MC agreement is visible in the invariant mass distribution of the leading Z (M_Z^{Lead}) for CCCC and CCCF events, especially around the nominal mass of the Z peak. In both distributions, the MC signal shows a long tail in the low part of the M_Z^{Lead} , that corresponds to electrons losing part of the energy due to bremsstrahlung process. In the case of the no-leading Z , the distributions of M_Z showed the same behavior as that of the leading. The corresponding distributions are shown in appendix C.

The p_T distributions of the leading Z , for CCCC and CCCF events are presented in figure 5.9. The CCCC events, on the left side of the figure, showed an acceptable Data-MC agreement. The same situation is observed in the CCCF events. In both cases, the MC signal shows the expected exponential decay in the energy of the Z . The p_T distribution of the second leading Z (subleading Z) can be seen in the appendix C. The p_T distribution in this case is similar to that of the leading Z .

Another important distribution to be analyzed is the invariant mass of the diboson system (M_{ZZ}). This distribution is shown separated for CCCC and CCCF events in the figure 5.10. The agreement between data and MC prediction is good for both cases.

A pair of bosons selected in this analysis, with invariant mass in the range 66 to 116 GeV, are on-shell bosons. For that reason, the distribution of the invariant mass of the ZZ starts at a value around of 114 GeV. The ZZ are only produced via non-resonant mechanisms, causing the invariant mass of the ZZ not to follows a Breit-Wigner form.

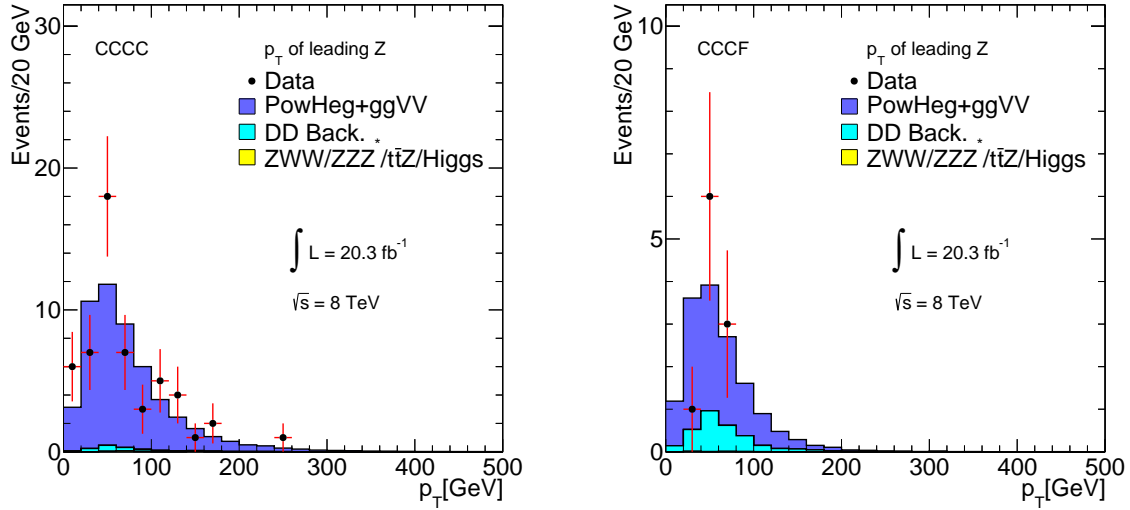


Figure 5.9: p_T distribution of the Z candidate with the larger p_T (leading Z). The left side shows events with four central electrons. The right side shows candidates with one forward electron and three centrals.

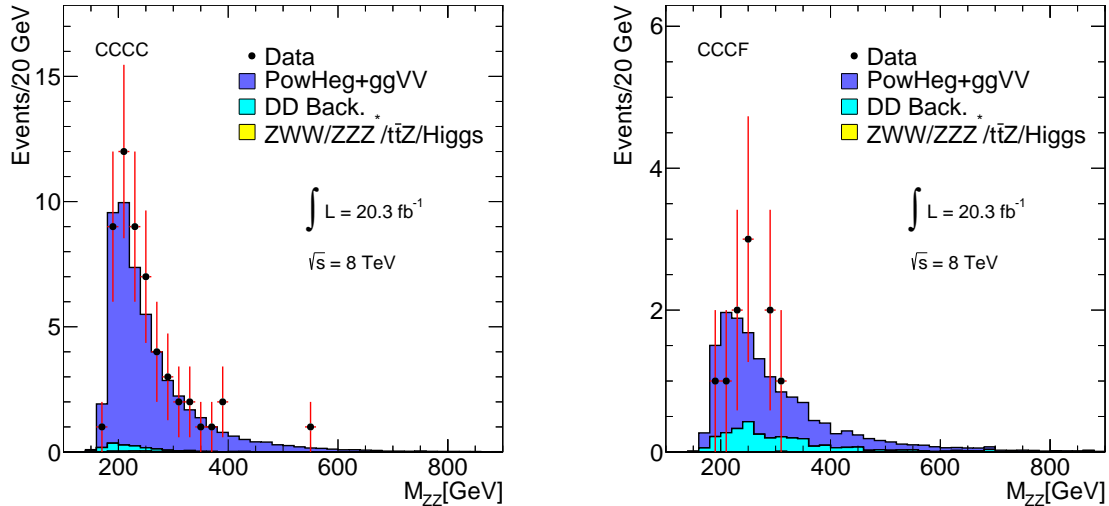


Figure 5.10: Mass spectrum of the ZZ candidates. The left side shows events with only central electrons while the right side shows candidates with one forward electron and three centrals.

In figure 5.11, the p_T distribution of ZZ is shown. The data and the MC show a better agreement for the CCCF events. The MC signal shows exponential decay, such as that observed in figures 5.6 and 5.7. The distribution in the rapidity of the pairs of Z is shown in the figure 5.12. The right side of the figure shows the CCCF events in comparison to the rapidity distribution of the CCCC events (left side of 5.11), which show that the use of forward electrons increases the available acceptance to the study of the ZZ production.

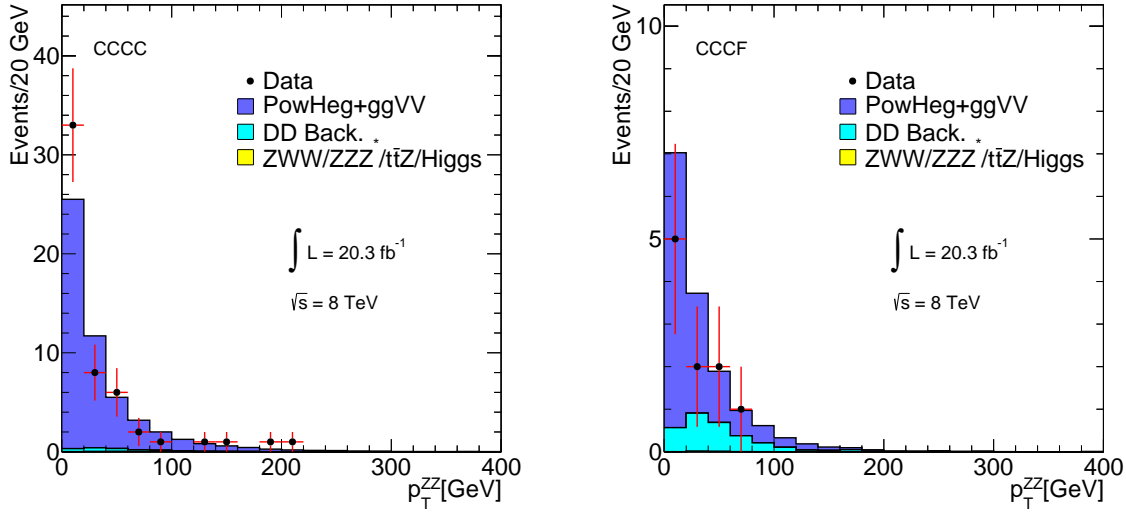


Figure 5.11: p_T of the ZZ candidates. The left side shows events with only central electrons while candidates with one forward electron and three centrals are shown at right side.

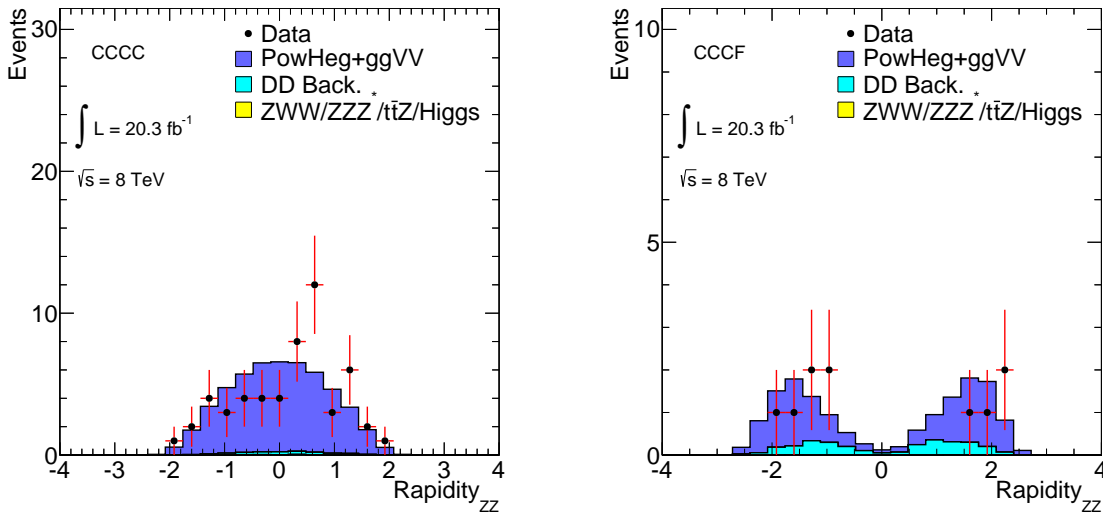


Figure 5.12: The figure shows the rapidity of the ZZ candidates. Left side shows events with only central electrons meanwhile at right side are candidates with one forward electron and three centrals.

The effect of the combination of the CCCC and CCCF events on kinematic variables are shown in figure 5.13. The invariant mass and the p_T of the ZZ can be seen in the left and right part of the figure, respectively. The same characteristics of the on-shell selected bosons are seen in the invariant mass of the combined CCCC and CCCF events. It is easy to see that the combination of central and forward electron channels shows a nice Data-MC agreement.

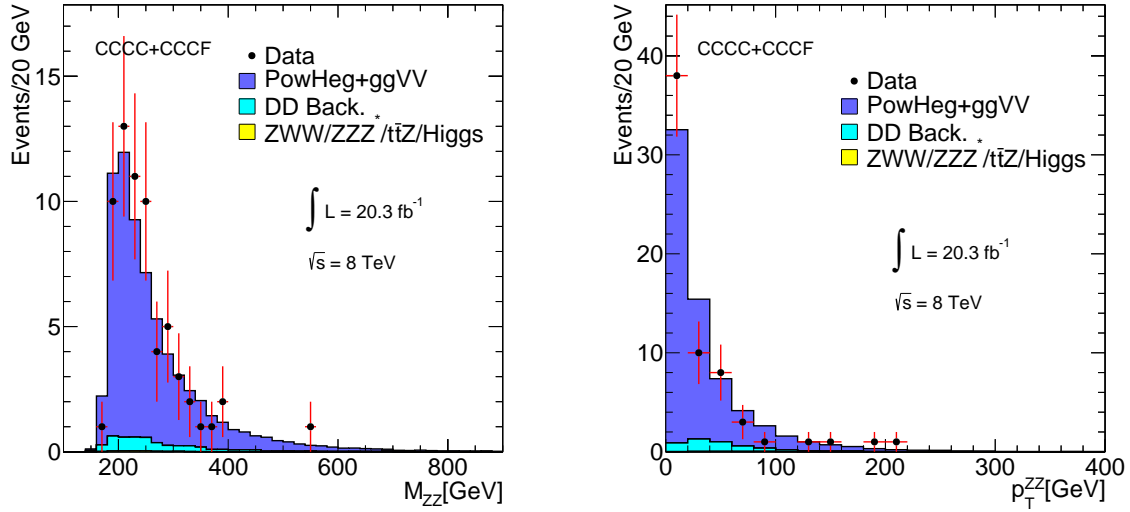


Figure 5.13: Mass spectrum (left) and p_T (right) of the ZZ candidates with four central electrons and three central and one forward electrons.

A conclusion of the results shown above, is that the extension of the analysis of the ZZ to cover electrons with high values of the pseudorapidity can improve the description of the kinematic distribution of the ZZ system. In the distributions of the different variables shown above, it can be seen that the background in the CCCF events is larger compared with the background in the CCCC events. The reason for these characteristics is the absence of track information in the identification of forward electrons. However, the forward electrons increase the number of possible ZZ candidates.

Chapter 6

Cross Section Measurement

“He repeated until his dying day that there was no one with more common sense, no stonemason more obstinate, no manager more lucid or dangerous, than a poet.”
—*Love in the Time of Cholera*
—*Gabriel Garcia Marquez*

As already mentioned in chapter 2, the number of expected events of a specific process is related to the experimental luminosity through a factor referred to as the cross section (σ). The cross section can be calculated using the equation shown below.

$$\sigma = \frac{N}{\mathcal{L}} \quad (6.1)$$

where N is the number of expected events corresponding to the process that σ represents and \mathcal{L} the total integrated luminosity. But the use of this equation assume the existence of a perfect detector, able to cover the full available phase space and work with 100% efficiency.

In order to determine the cross section of a process using experimental results, it is necessary to introduce some corrections related to the performance of the detector. In this chapter, the extraction of the production cross section of ZZ will be described. The definition of fiducial and total cross will be given. At the end of the chapter, differential cross section as a function of the invariant mass of the dibosons and the p_T of the most energetic Z (leading Z) will be shown.

6.1 Fiducial and Total Cross Section Definition

Experimental conditions, like the selection cuts or the detector p_T and angular covering, define a phase space where the events of a process can be measured. In addition, the behavior of the detector in terms of the energy resolution and identification efficiency of particles introduces a dependency of the number of observed events on the detector performance. For that reason, in general, two kinds of cross sections are defined, i.e., fiducial and total cross section.

The fiducial cross section (σ^{fidu}) is defined in a kinematic phase space as closest possible to the detector acceptance for the studied process, referred to as fiducial volume. The total cross section (σ^{tot}) corresponds to an extrapolation of the measured cross section in the fiducial volume to the full phase space, not full accesses for the detector.

The fiducial cross section can be calculated using the expression 6.2:

$$\sigma^{fidu} = \frac{N^{Signal} - N^{Back.}}{\mathcal{L} \times C_{ZZ}} \quad (6.2)$$

In the above equation, N^{Signal} and N^{Back} correspond to the number of events measured and the number of expected background events. C_{ZZ} is a correction factor, commonly known as efficiency, introduced in order to extrapolate the true number of events in the fiducial phase space from the number of observed events. For that reason, C_{ZZ} involves the efficiencies of the detector to the reconstruction, identification and trigger selection. The efficiency can be calculated using the equation shown below:

$$C_{ZZ} = \frac{N_{\text{Reconstructed } ZZ}^{\text{MC pass all cuts}} \times SF}{N_{\text{Generate } ZZ}^{\text{MC fiducial volume}}} \quad (6.3)$$

The Numerator of C_{ZZ} is calculated with the full ZZ selection at reconstruction level corrected with Scale Factors (SF). The Denominator is calculated with true variables.

The total cross section can be calculated from the fiducial cross section by introducing a correction referred to as acceptance A_{ZZ} and the branching ratio of $ZZ \rightarrow 4e$ (see equation 2.22):

$$\sigma^{tot} = \frac{N^{Signal} - N^{Back.}}{\mathcal{L} \times C_{ZZ} \times A_{ZZ} \times BR\{ZZ \rightarrow 4e\}} \quad (6.4)$$

where the acceptance is calculated by using the equation 6.5. In that case, A_{ZZ} is calculated as a ratio between the number of expected events with the fiducial cuts at generate level and the number of events without cuts at generate level. In this thesis, the total cross section is defined in the full phase space for Z paira with an invariant mass in the range 66–116 GeV.

$$A_{ZZ} = \frac{N_{\text{Generate } ZZ}^{\text{MC fiducial volume}}}{N_{\text{Generate } ZZ}^{\text{MC all}}} \quad (6.5)$$

In the next sections, a detailed description of the production cross section extraction for the ZZ process will be given.

6.2 Fiducial Volume Definition

As already mentioned in chapter 2, previous ATLAS results of the production cross section of dibosons, involving electrons, covered a η region limited to the central part of the detector.

In this work an extended cross section calculation is provided, with $|\eta| < 4.9$. In order to make a comparison with previous results and to provide the cross section measurement at high pseudorapidity values, two fiducial volumes are defined. The fiducial volumes are:

1. Fiducial volume central:

- $66 < M_{\ell\ell} < 116$ GeV
- $\Delta R(\ell, \ell) > 0.2$
- $p_T^\ell > 7$ GeV
- $|\eta^\ell| < 2.5$

2. Fiducial volume central-forw.:

- $66 < M_{\ell\ell} < 116$ GeV
- $\Delta R(\ell, \ell) > 0.2$
- $p_T^\ell > 7$ GeV
- Three electrons with $|\eta^\ell| < 2.5$ and one with $2.5 < |\eta^\ell| < 4.9$

As can be seen in the definition of the fiducial volume central-forw, events with one forward electron are included. For both of the volumes only on-shell Z are considered. In the next section, the calculation of the efficiency corrections is shown.

6.3 Efficiency Determination

In order to calculate the C_{ZZ} , the number of expected events in the fiducial volume is determined at reconstruction level and at generate level. It is made using MC simulations. Two different generators are used: The `PowhegPythia` [29] simulates the production of ZZ via quark-antiquark interaction. ZZ produced via gluon-gluon fusion ($\approx 6\%$) is simulated using `ggVV` [30].

In figures 6.1 and 6.2, the mass distribution of Z pairs at reconstructed and generated level for each mentioned generator are shown. The left side of the figure shows only events in the fiducial volume central. The right side shows the distribution for ZZ events, including forward electrons.

	Fiducial volume central	Fiducial volume central-forw.
$C_{ZZ}^{\text{PowhegPythia}}$	0.558 ± 0.002	0.318 ± 0.003
C_{ZZ}^{ggVV}	0.568 ± 0.002	0.290 ± 0.010
C_{ZZ} Combined.	0.559 ± 0.003	0.317 ± 0.010

Table 6.1: C_{ZZ} values for ZZ `PowhegPythia` and `ggVV` signal samples and the combined value taken 6% of contribution from the `ggVV` sample. Numbers for only central and central-forw. volume are shown. Only statistical uncertainties are shown.

In table 6.1, the values of C_{ZZ} for each generator and both defined fiducial volumes are shown with only statistical uncertainties. The combined C_{ZZ} are calculated considering a 6% contribution from the $ggVV$ sample. Comparing the C_{ZZ} combined for the fiducial volume central and the central-forw, a decrease in the efficiency of the order of 12% is observed.

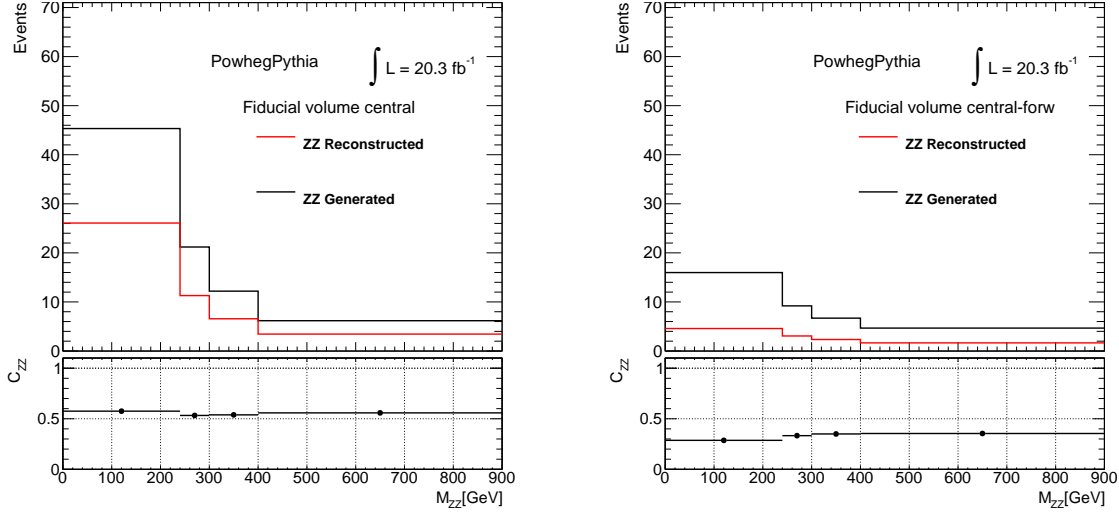


Figure 6.1: Number of ZZ events at reconstruction and generation level in PowhegPythia samples are shown. The left side shows central electrons, only. The right side shows the central-forw. fiducial volume.

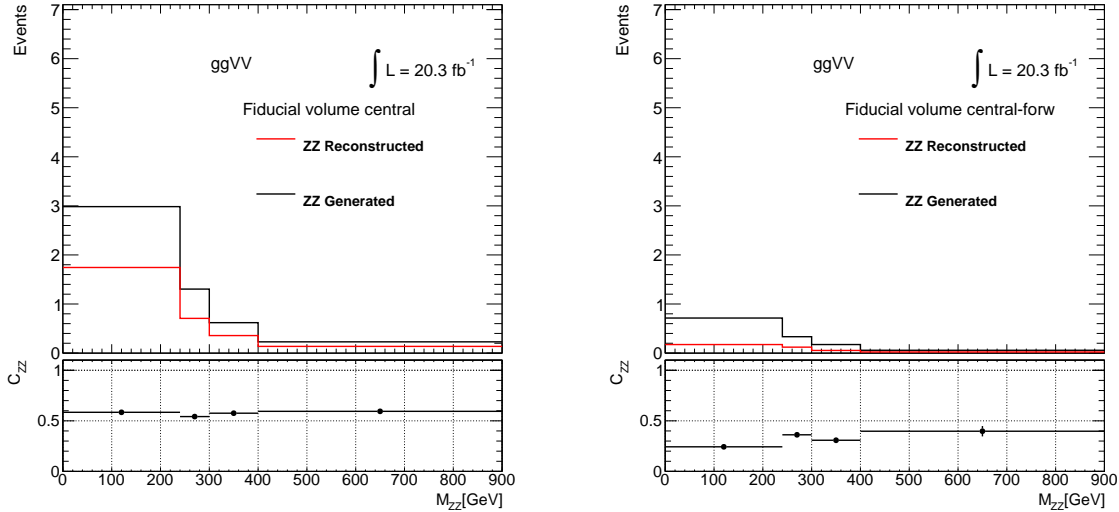


Figure 6.2: Number of ZZ events at reconstruction and generation level in $ggVV$ samples are shown. The left side shows central electrons, only. The right side shows the central-forw. phase space.

6.4 Acceptance Determination

The acceptance A_{ZZ} is calculated using MC simulations at generation level. The number of events in the fiducial volume are compared with the total number of events generated in the full

p_T and η range. No correction is made on the mass of the dibosons, so only pairs of on-shell Z are taken.

The mass spectrum of the ZZ and the A_{ZZ} for the `PowhegPythia` and `ggVV` are respectively shown in figure 6.3 and 6.4. In both figures, the fiducial volume only with central electrons (left side) and the fiducial volume central-forw (right side) can be seen. The gain in the acceptance including forward electrons is notable for the both kind of MC generators.

In table 6.2, the values of A_{ZZ} for each generator and both defined fiducial volumes are shown, only statistical uncertainties are shown. The combined A_{ZZ} are again calculated considering a 6% contribution from the `ggVV` sample. The increase on the A_{ZZ} with the introduction of forward electrons is around 44%.

	Fiducial volume central	Fiducial volume central-forw.
$A_{ZZ}^{\text{PowhegPythia}}$	0.583 ± 0.001	0.267 ± 0.001
A_{ZZ}^{ggVV}	0.723 ± 0.002	0.178 ± 0.004
A_{ZZ} Combined	0.591 ± 0.004	0.261 ± 0.004

Table 6.2: Values of A_{ZZ} for ZZ `PowhegPythia` and `ggVV` signal samples and the combined value taken a 6% of contribution from the `ggVV` sample. Numbers for only central and central-forw. volume are shown with only statistical uncertainties.

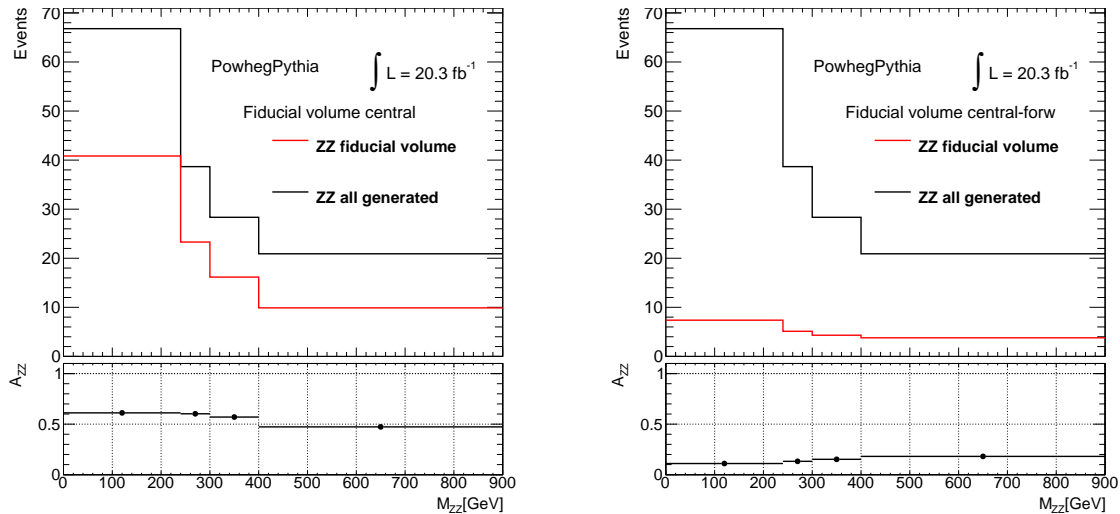


Figure 6.3: Number of ZZ events at generation level in `PowhegPythia` samples are shown. On the left side only central electrons are shown. On the right side is shown the central-forw. volume.

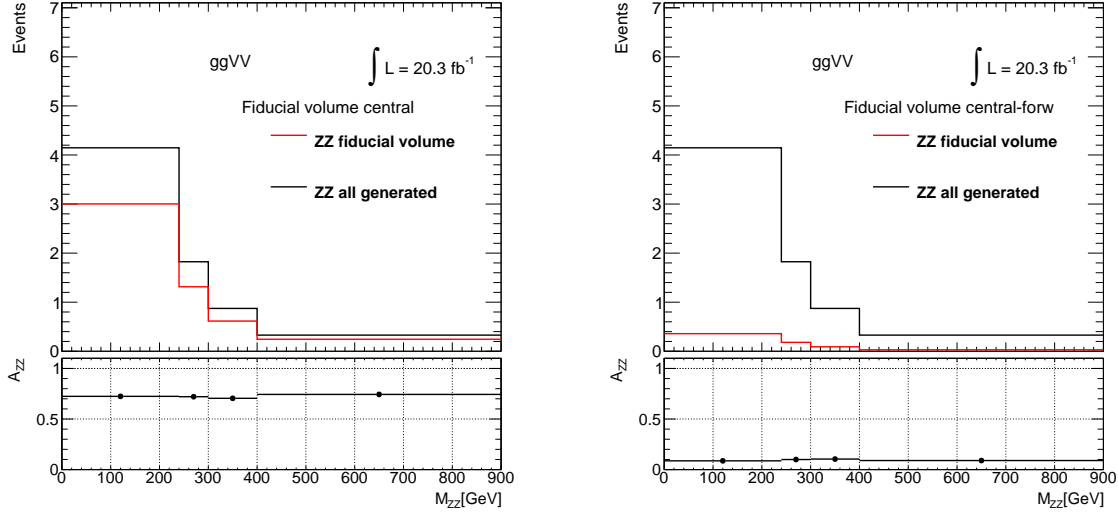


Figure 6.4: Number of ZZ events at reconstruction and generated level in $ggVV$ samples. On the left side only central electrons are shown. The right side shows the central-forward volume.

6.5 Cross Section Calculation

The fiducial cross section and the total cross section of the ZZ production can be calculated using the equations 6.2 for σ^{fidu} and 6.4 for σ^{tot} . The value of the integrated luminosity is $\mathcal{L} = 20.3 \pm 0.6 \text{ fb}^{-1}$. The rest of the necessary elements to do the calculation are shown in table 6.3

	Fiducial volume central	Fiducial volume central-forw.
N^{Signal}	54	10
$N^{Back.}$	1.7 ± 0.5	2.9 ± 0.7
C_{ZZ}	0.559 ± 0.003	0.317 ± 0.003
A_{ZZ}	0.591 ± 0.004	0.261 ± 0.004

Table 6.3: Values required to calculate the fiducial and cross sections. Only statistical uncertainties are given.

With the values given in table 6.3 the fiducial σ^{fidu} and total σ^{tot} cross section values are calculated and shown in the table below (6.4) where only statistical uncertainties are shown. In the next section, a description of the source of systematic uncertainties considered in this analysis is discussed.

	Fiducial volume central	Fiducial volume central-forw.
$\sigma^{fidu}(\text{fb})$	4.6 ± 0.6	1.3 ± 0.6
$\sigma^{tot}(\text{pb})$	6.9 ± 1.0	7.4 ± 3.4

Table 6.4: Fiducial and total cross section for the two defined volumes. Only statistical uncertainties are shown.

6.6 Systematic Determination

Different sources of systematics affect the final result of the measured cross section. The characteristics of the MC simulations used to calculate A_{ZZ} and C_{ZZ} and the background calculations are examples of parameters that need to be considered to calculate the final uncertainty in the measured cross sections. A detailed description of the principal sources of systematic uncertainties is offered below:

1. **MC corrections:** As mentioned in section 5.2.1, scale factors (SFs) are derived from Data-MC studies and used to correct inefficiencies of the MC simulations. There are SF, that correct the reconstruction and identification of electrons, the trigger selection and the efficiency of the isolation variables.
Systematic variations are provided together with the scale factors. Up and down variations of the SFs are applied to the MCs and propagated into the calculation of the cross section. A comparison of the cross sections after variation of the SF and the nominal value obtained with the values given in table 6.4, is made and the highest difference is taken as systematic uncertainty for σ^{fidu} and σ^{tot} in each defined volume.
2. **Energy correction:** Variations on the energy smearing of the MC are applied and propagated to study the effects of the energy calibration on the calculation of the cross section.
3. **Data driven uncertainties:** The statistical and systematic uncertainties were introduced in the calculation of the cross section. The uncertainty in the data driven method is one of the biggest sources of uncertainty in the cross section, due principally to the low statistics available, especially in the forward region.
4. **MC Generator:** The nominal MC used in the calculation of A_{ZZ} and C_{ZZ} are the `PowhegPythia` and the `ggVV`. A ZZ MC generated with Pythia [49] was used to compare the already shown values of the cross section.
5. **Normalization and renormalization scales:** A definition of the normalization μ_R and factorization μ_F scales was given in chapter 2. The nominal values of μ_R and μ_F used in this analysis are $\mu_R = \mu_F = M_Z$. `PowhegPythia` MC samples were generated with

different values of μ_R and μ_F to investigate the effect of scale variation. A list of the produced samples is given in table 6.5. The cross section obtained with those samples was compared to the nominal value and the highest difference to the cross section at the nominal value was taken as a symmetric uncertainty.

	μ_F	μ_R
Nominal	M_Z	M_Z
Sample 1	M_Z	$2M_{ZZ}$
Sample 2	M_Z	M_{ZZ}
Sample 3	$2M_{ZZ}$	M_Z
Sample 4	$2M_{ZZ}$	$2M_Z$
Sample 5	$2M_{ZZ}$	M_{ZZ}
Sample 6	M_{ZZ}	M_{ZZ}
Sample 7	M_{ZZ}	M_Z
Sample 8	M_{ZZ}	$2M_{ZZ}$

Table 6.5: Values of the normalization and factorization scales and nominal value used to study the effect of the scale election on the cross section calculation.

6. **PDF variation:** The nominal value of the cross section with the CT10 PDF is compared with the cross section obtained using the MSW2008 PDF set.

In table 6.6, the relative systematic uncertainties on the total cross section for each systematic source are shown. The sources of systematics are separated into experimental and theoretical sources. The experimental sources are related to the SFs used to the correction of the MCs and the background estimation. The theoretical sources are due to changes in the MC used in the calculation of the C_{ZZ} and A_{ZZ} correction factors.

From the table shows how that the statistical uncertainty of the data driven method (DD stat.) is the principal source of uncertainty in the experimental uncertainties. In the case of the theoretical sources the MC generator is the major source of uncertainty.

In table 6.7, the fiducial and total cross sections with statistical and systematics uncertainties are shown for each defined phase space. The uncertainty in the Luminosity is not included.

To finalize this section, the fiducial and total cross sections, due to the combination of the central and central-forw. phase spaces, are shown. In table 6.8, the combined cross sections are shown. Statistical and systematic uncertainties can be seen. The fiducial cross section increases with the addition of the central-forw. phase space. The total cross section can be compared to the theoretical prediction given in equation 2.23 of $\sigma_{ZZ}^{total}(pp \rightarrow ZZ + X) = 7.2_{-0.2}^{+0.3}$ pb. No significant deviation of the measured value with respect to the theoretical prediction is observed.

	Fiducial volume central	Fiducial volume central-forw.
Experimental uncertainties		
Luminosity	2.8	2.8
Energy smearing	0.01	0.19
reconstruction efficiency	1.0	1.2
Identification efficiency	1.7	2.2
Isolation and IP	0.9	0.4
Trigger efficiency	0.04	0.1
DD stat.	1.0	12.1
DD sys.	0.1	5.4
Theoretical uncertainties		
MC Generator	5.3	0.3
MC Scale	0.4	0.9
PDF	0.8	0.8

Table 6.6: Relative systematic uncertainties (%) on the total cross section for all considered volumes.

	Fiducial volume central	Fiducial volume central-forw.
σ^{fidu}	4.6 ± 0.6 (Stat.) ± 0.3 (Sys.) ± 0.1 (Lumi) (fb)	1.3 ± 0.6 (Stat.) ± 0.3 (Sys.) ± 0.04 (Lumi.) (fb)
σ^{tot}	6.9 ± 1.0 (Stat.) ± 0.3 (Sys.) ± 0.2 (Lumi) (pb)	7.4 ± 3.4 (Stat.) ± 0.2 (Sys.) ± 0.2 (Lumi.) (pb)

Table 6.7: Fiducial and total cross section for the two defined volumes. Absolute statistical and systematic uncertainties are shown.

	Combined
σ^{fidu}	6.0 ± 0.8 (Stat.) ± 0.3 (Sys.) ± 0.3 (Lumi.) (fb)
σ^{tot}	7.3 ± 1.0 (Stat.) ± 0.4 (Sys.) ± 0.2 (Lumi.) (pb)

Table 6.8: Fiducial and total cross section for the combination of the defined volumes. Absolute Statistical and systematic uncertainties are shown.

The combined total cross section can be compared with SM expectation of:

$$\sigma_{ZZ}^{total}(pp \rightarrow ZZ + X) = 7.2_{-0.2}^{+0.3} \text{ pb} \quad (6.6)$$

The agreement with the SM expectation is better with the inclusion of events with three central electrons and one forward electron.

6.7 Differential Cross Section

In order to do a better comparison of the production cross section of ZZ , the fiducial differential cross section as function of M_{ZZ} and the p_T of the leading Z is calculated. In figures 6.5 and 6.6, the differential fiducial cross sections are shown. In the figures, the obtained cross section is compared with the SM prediction given by `PowHegPythia + ggVV` samples. The blue boxes, shown in the figures, represent the total systematics and statistical uncertainties shown in table 6.7, added in quadrature. The agreement between the expected cross section and the measured is good between the uncertainties.

From the measurement of cross sections, fiducial and total, and from the differential distributions shown in the last part of this chapter, there is no evidence of a significant deviation from the expectation of the cross section with the measured values. For that reason, in the next chapter, limits to the values of the neutral triple gauge couplings aTGCs will be calculated.

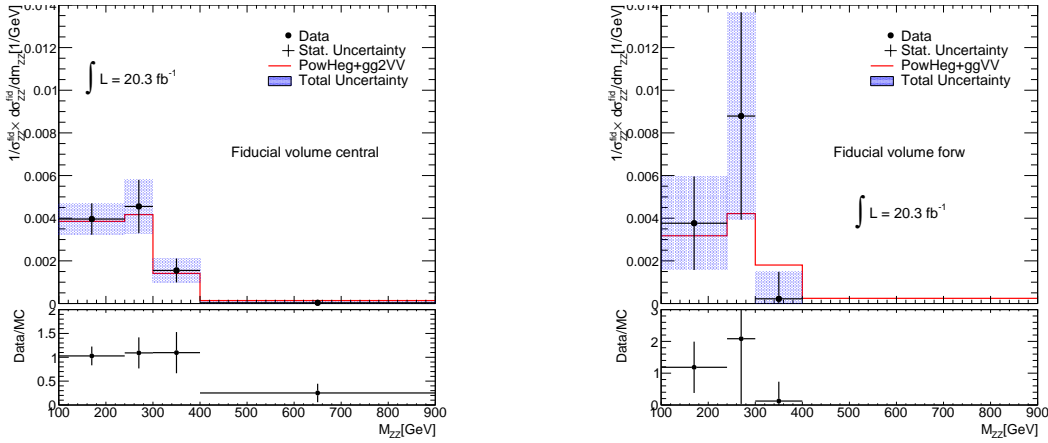


Figure 6.5: Differential fiducial cross as function of the invariant mass of the ZZ .

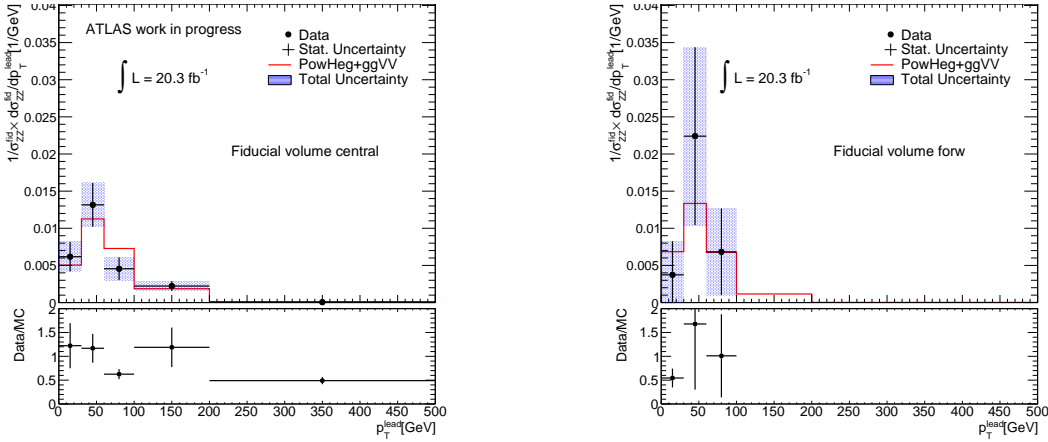


Figure 6.6: Differential fiducial cross as function of the p_T of the leading Z .

Chapter 7

Limits on aTGC in ATLAS

“I’m sciencing as fast as I can.”

—Professor Farnsworth

As discussed in 2.6.2, anomalous triple gauge couplings would lead to an increase in the cross section for ZZ production, especially at high values of the transfer momentum. As shown in figure 2.5, the p_T of the leading Z is particularly sensitive to the presence of aTGCs. Other variable, usually considered in searches of anomalous TGCs, is the invariant mass of the ZZ system. The observed number of events compare to the predicted SM are used to look for aTGCs. If deviations are not observed, limits to the possible values of the anomalous couplings can be derived.

In this chapter, the strategy to set limits to the aTGCs is described. Then, the expected limits to the anomalous triple gauge couplings are shown.

7.1 Anomalous Triple Gauge Couplings

In order to study the effect of the anomalous TGCs, MC simulations with different values of the parameters f_4^γ , f_4^Z , f_5^γ and f_5^Z are produced. The samples were generated using SHERPA[50] with CT10 PDF. Three samples are used in this analysis, with the following couplings: $f_4^\gamma = 0.1$ denoted TGC0, $f_4^\gamma = f_5^Z = 0.1$ denoted TCG1 and $f_4^\gamma = f_4^Z = f_5^\gamma = f_5^Z = 0.1$ denoted TGC2. The samples are generated without a form factor and the couplings are selected close to the experimental limits set by the LEP experiment.

Figures 7.1 and 7.2 show a comparison between the SM prediction and the TGC0 samples for the invariant mass of the ZZ and the p_T of the leading Z . The effect on ZZ events with four central electrons (left side of the figure) and events with three central electrons and one forward electron (right side of the figure) can be seen in the figures. The effect of the anomalous TGCs is more clearly visible on the left side of figures 7.1 and 7.2. In the case of the invariant mass, the increase in the number of events, due to the TGC, is more important for values starting at

600 GeV. For the p_T , the aTGCs make a contribution at values larger than 150 GeV. For the events with one forward electron, the effect of TGCs on the expected number of events is more important in the p_T distribution.

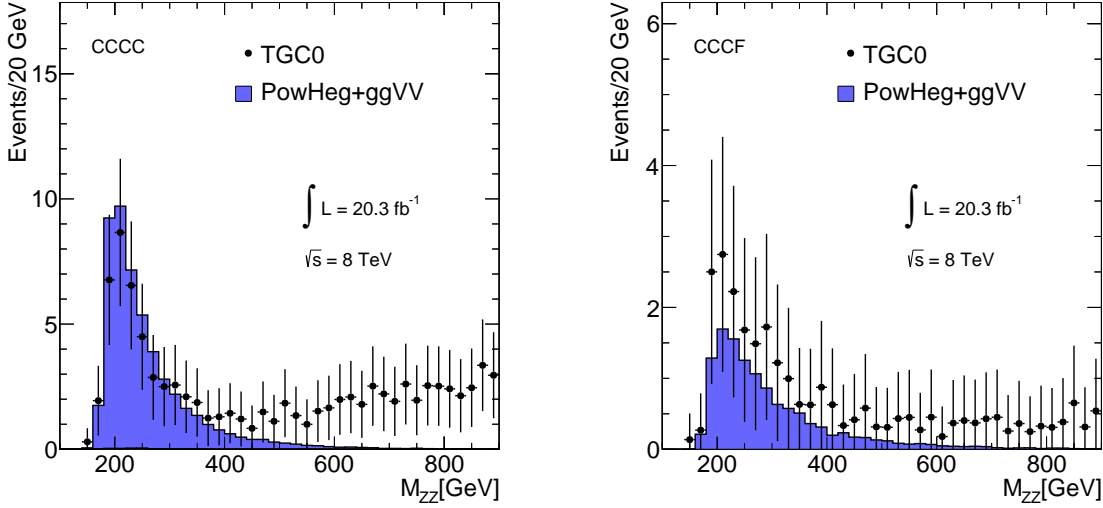


Figure 7.1: Invariant mass of the ZZ events predicted by SM (blue line) is compared to the distribution for the TGC0 sample. The left side shows events with four central electrons, and the right side shows events with three central and one forward electron.

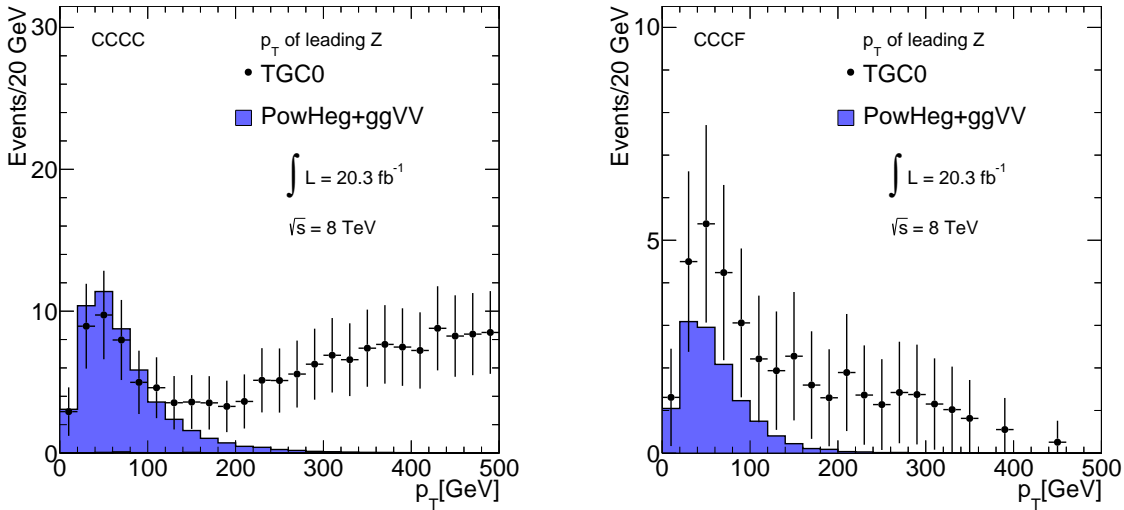


Figure 7.2: Transverse momentum of the leading Z predicted by SM (blue line) is compared to the distribution for the TGC0 sample. The left side shows events with four central electrons, and the right side shows events with three central and one forward electron.

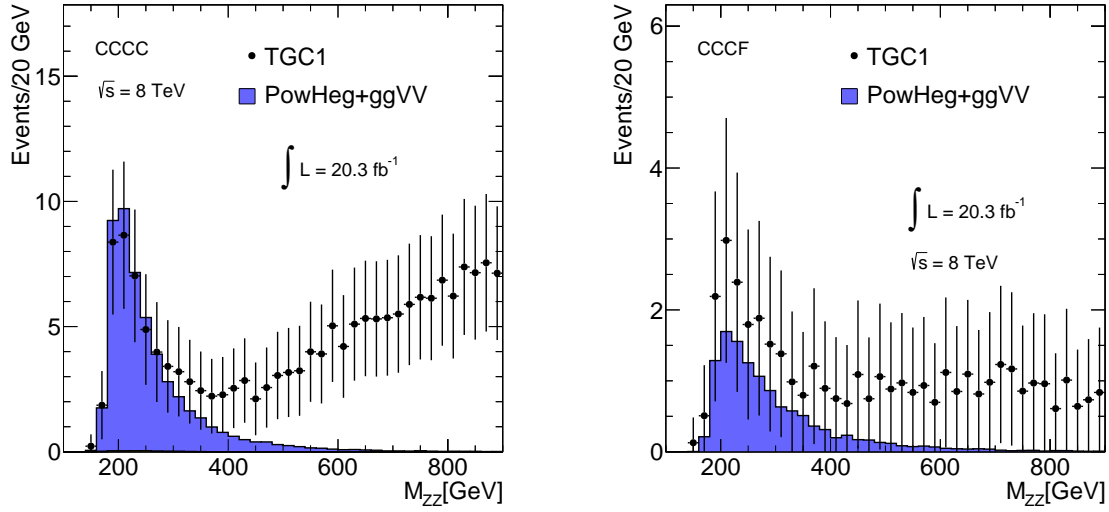


Figure 7.3: Invariant mass of the ZZ events predicted by SM (blue line) is compared to the distribution for the TGC1 sample. The left side shows events with four central electrons, and the right side shows events with three central and one forward electron.

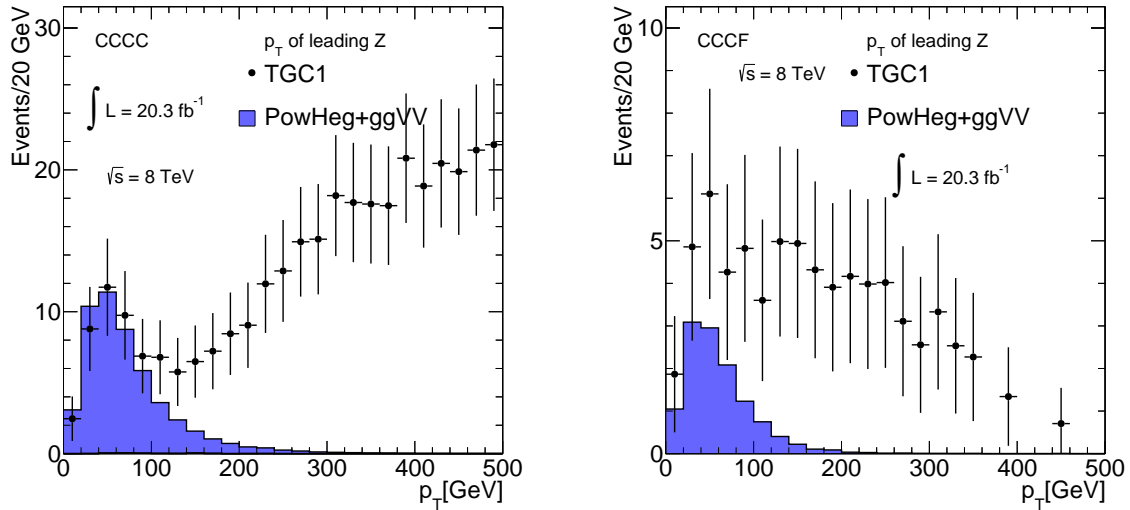


Figure 7.4: Transverse momentum of the leading Z predicted by SM (blue line) is compared to the distribution for the TGC1 sample. Left side shows events with four central electrons, and the right side shows events with three central and one forward electron.

The TGC1 sample produces a stronger enhancement of the signal compare to TCG0, as can be seen in figure 7.3 and 7.4. The left side of the figures shows the invariant mass of the ZZ and the p_T of the leading Z distributions of events with four central electrons. The right side shows events with three central and one forward electron.

The values of the parameters f_i^V used to produce the TGC0, TGC1 and TGC2 samples are ten times larger than the values of the limits derived by ATLAS, shown in table 2.2, in

chapter 2. For that reason, in order to have a better idea of the effects of the aTGCs with limits close to these shown in table 2.2, a reweighting method is implemented. In the next section, a description of the reweighting procedure is given.

7.2 Matrix Elements Reweighting

As mentioned in section 2.6.2, the anomalous couplings affect the ZZ production. The result is the increase in the production cross section, especially at high values of p_T , as already shown in figures in section 7.1. The increase in the production cross section can be parametrized as function of the couplings as shown below:

$$\begin{aligned}
 d\sigma_{SM+TGC} = & F_{00} + f_4^\gamma F_{01} + f_4^Z F_{02} + f_5^\gamma F_{03} + f_5^Z F_{04} \\
 & + (f_4^\gamma)^2 F_{11} + f_4^\gamma f_4^Z F_{12} + f_4^\gamma f_5^\gamma F_{13} + f_4^\gamma f_5^Z F_{14} \\
 & + (f_4^Z)^2 F_{22} + f_4^Z f_5^\gamma F_{23} + f_4^Z f_5^Z F_{24} \\
 & + (f_5^\gamma)^2 F_{33} + f_5^\gamma f_5^Z F_{34} \\
 & + (f_5^Z)^2 F_{44}
 \end{aligned} \tag{7.1}$$

F_{ij} are coefficients that describe how the cross section change in the presence of the aTGCs. The F_{00} correspond to the contribution of the Standard Model.

With the help of the equation shown above, it is possible to reweigh a sample generated at any value of the TGCs to the SM or to other selection of couplings. For example, to reweigh the TGC0 sample, generated with $f_4^\gamma = 0.1$ to the Standard Model, one would apply to each event a weight of the form:

$$weight = \frac{F_{00}}{F_{00} + 0.1F_{01} + (0.1)^2 F_{11}} \tag{7.2}$$

The F_{ij} in equation 7.1 are completely specified by the kinematic of the incoming and outgoing particles, so they must be evaluated in an event on event basis. The values of F_{ij} are independent of the coupling choice, but depend on the form factor assumed.

The coefficients are determined from the SHERPA samples as follows. From the equations 7.1, it is possible to write down 15 equations that define the coefficients F_{ij} , uniquely. As an illustration, it is convenient to consider the case of only one coupling f . In that case, the equation 7.1 is reduced to:

$$\sigma_{SM+TGC} = F_{00} + fF_{01} + f^2 F_{11} \tag{7.3}$$

Only three coefficients must be determined. If f can take the values -1,0,1, the independent equations can be written as:

$$\begin{pmatrix} d\sigma_1 \\ d\sigma_2 \\ d\sigma_3 \end{pmatrix} = \begin{pmatrix} 1 & 0 & 0 \\ 1 & 1 & 1 \\ 1 & -1 & 1 \end{pmatrix} \begin{pmatrix} F_{00} \\ F_{01} \\ F_{11} \end{pmatrix}$$

If the complete 15 couplings are taken, there is a total of 15 independent equations. This system of equation can be written in matrix form, as:

$$d\vec{\sigma} = \hat{A}\vec{F} \quad (7.4)$$

The vector \vec{F} of the coefficients can be determined by inversion of the matrix \hat{A} ; $\vec{F} = \hat{A}^{-1}d\vec{\sigma}$. The matrix elements are obtained from the BHO[51] generator. The matrix elements are then introduced in the framework described in [52], which led to the calculation of the amplitude given by the four vectors and PDG values of the incoming and outgoing particles.

To finalize this section, an example of the reweighting process is shown. TGC0 and TGC1 samples are reweighted according to fit the SM expectations, the result of the reweighting is shown in the following figures.

In figures 7.5 and 7.6, TGC0 samples are reweighted according to suit the Standard Model expectation. The agreement of the reweighted curve and the SM prediction is quite good, especially for the plot shown on the left side of the figures, corresponding to the diboson events with four central electrons.

The other aTGC MC samples were reweighted, too according to fit to the SM expectation. In all cases the agreement between the curves is good.

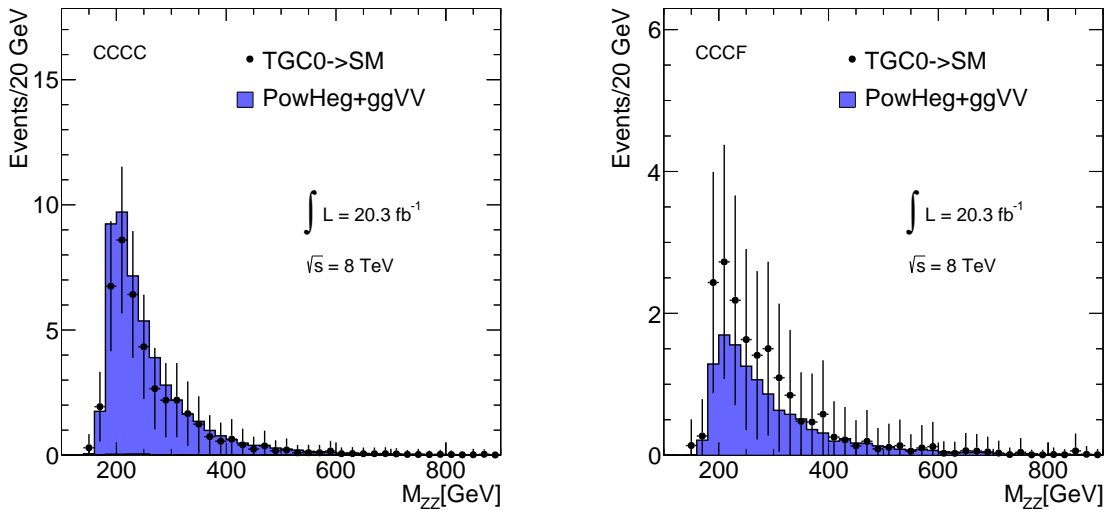


Figure 7.5: Invariant mass of the ZZ events predicted by SM (blue line) is compared to the distribution for the TGC0 sample, reweighted to the Standard Model expectation using the method described in this section. The left side shows events with four central electrons, and the right side shows events with three central and one forward electron.

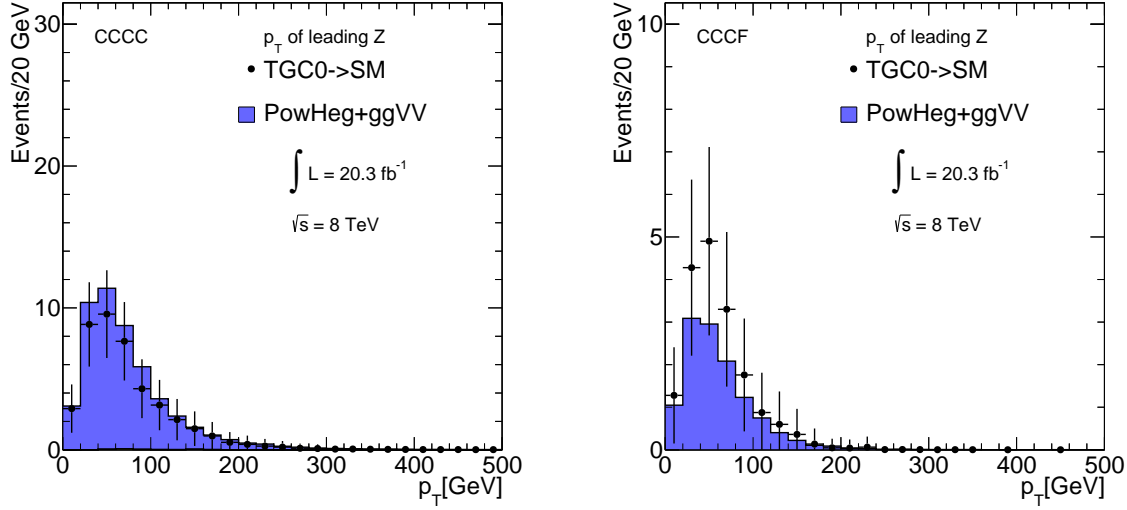


Figure 7.6: Transverse momentum of the leading Z predicted by SM (blue line) is compared to the distribution for the TGC0 sample, reweighted to the Standard Model expectation using the method described in this section. The left side shows events with four central electrons, and the right side shows events with three central and one forward electron.

7.3 Limits Extraction

In order to set limits to the neutral couplings; i.e., f_4^γ , f_4^Z , f_5^γ and f_5^Z a set of MC simulations with different values of the couplings can be produced and, then, the expected yield as a function of the coupling strength can be derived. However, this process is computationally very demanding.

A better approximation is to use the matrix element reweighting procedure, shown in section (7.2), to obtain a sample with values close to the limits already set for the anomalous couplings. With the reweighted matrix, the expected yield as a function of the aTGCs can be determined and, then, 95% confidence level limits can be set using a frequentist likelihood ratio. A detailed description of the whole procedure is given below.

7.3.1 Yield Determination

In order to extract limits on the aTGCs an estimation of the increase in the expected signal as a function of the couplings should be determined. The yield due to the aTGCs is parameterized by Y_{ij} coefficients, which are calculated from the F_{ij} , introduced in previous section, which are obtained by the matrix reweighting procedure described in section 7.2. The Y_{ij} are given by:

$$Y_{ij} = \sum_{Events} \left(\frac{F_{ij}}{d\sigma_{sample}} \right) \quad (7.5)$$

where the summation is over all the events passing the selection and the $d\sigma_{sample}$ corresponds to the differential cross section by event, obtained with the original parameters of the reweighted

sample.

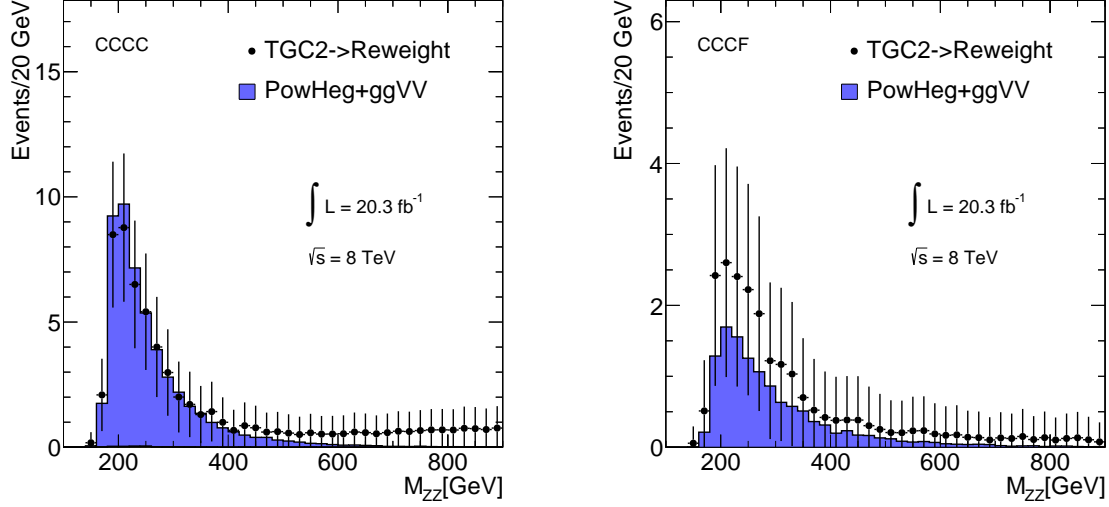


Figure 7.7: Invariant mass of the ZZ events predicted by SM (blue line) is compared to the distribution for the TGC2 sample, reweighted to $f_4^\gamma = f_4^Z = f_5^\gamma = f_5^Z = 0.012$, with an energy scale given by $\Lambda_{FF} = 3$ TeV. Left side shows events with four central electrons, and the right side shows events with three central and one forward electron.

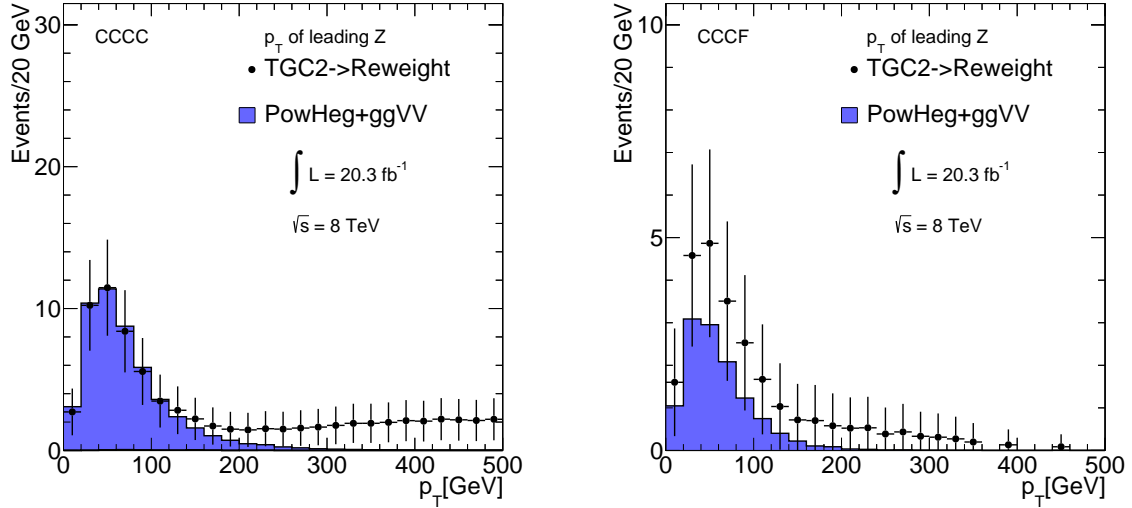


Figure 7.8: Transverse momentum of the leading Z predicted by SM (blue line) is compared to the distribution for the TGC2 sample, reweighted to $f_4^\gamma = f_4^Z = f_5^\gamma = f_5^Z = 0.012$, with an energy scale given by $\Lambda_{FF} = 3$ TeV. Left side shows events with four central electrons, and the right side shows events with three central and one forward electron.

In this work, the F_{ij} are calculated, from the reweighting of the TGC2 sample to the values of the anomalous couplings given by:

$$\begin{aligned}
f_4^\gamma &= f_4^Z = f_5^\gamma = f_5^Z = 0.012 \\
&\text{and} \\
\Lambda_{FF} &= 3\text{TeV}
\end{aligned} \tag{7.6}$$

and

$$\begin{aligned}
f_4^\gamma &= f_4^Z = f_5^\gamma = f_5^Z = 0.020 \\
&\text{and} \\
\Lambda_{FF} &= \infty
\end{aligned} \tag{7.7}$$

this choice was made in order to be close to the limits shown in table 2.2 of section 2.6.2, which correspond to the limits presented by ATLAS with a center of mass energy of $\sqrt{s} = 7$ TeV. Two energy scales were tested, one corresponding to $\Lambda_{FF} = \infty$ and the second $\Lambda_{FF} = 3$ TeV.

The effect of the reweighting process on the TGC2 sample can be seen in figures 7.7 and 7.8, where the mass spectrum of the ZZ and the p_T of the leading Z are shown, for the case of a $\Lambda_{FF} = 3$ TeV and $f_i^V = 0.012$.

The expected yield due to the anomalous couplings, can be written as:

$$\begin{aligned}
N_{exp} &= Y_{00} + f_4^\gamma Y_{01} + f_4^Z Y_{02} + f_5^\gamma Y_{03} + f_5^Z Y_{04} \\
&+ (f_4^\gamma)^2 Y_{11} + f_4^\gamma f_4^Z Y_{12} + f_4^\gamma f_5^\gamma Y_{13} + f_4^\gamma f_5^Z Y_{14} \\
&+ (f_4^Z)^2 Y_{22} + f_4^Z f_5^\gamma Y_{23} + f_4^Z f_5^Z Y_{24} \\
&+ (f_5^\gamma)^2 Y_{33} + f_5^\gamma f_5^Z Y_{34} \\
&+ (f_5^Z)^2 Y_{44}
\end{aligned} \tag{7.8}$$

In table 7.1 and 7.2, the expected yield as a function of the anomalous couplings is shown. Table 7.1 shows the case of a $\Lambda_{FF} = 3$ TeV and $n = 3$ (see equation 2.21). Table 7.2 shows the expected yield when any form factor is applied to the reweighting. In both tables, the yield coefficients Y_{ij} are normalized to the Standard Model expectation given by the `PowhegPythia + ggVV` samples for the CCC and CCCF combined events.

Y_{00}	Y_{01}	Y_{02}	Y_{03}	Y_{04}
62.3213	1.13077	-0.132434	-0.0530052	-0.20145
	Y_{11}	Y_{12}	Y_{13}	Y_{14}
	26079.5	23381.2	0.24532	0.098763
	Y_{22}	Y_{23}	Y_{24}	
	35309.1	0.0989338	0.28479	
	Y_{33}	Y_{34}		
	25459	22796.5		
	Y_{44}			
	34408.5			

Table 7.1: Expected yield as a function of the aTGCs. A value of $n = 3$ and an energy scale $\Lambda_{FF} = 3$ TeV was used. CCCC and CCCF events are considered.

Y_{00}	Y_{01}	Y_{02}	Y_{03}	Y_{04}
62.3213	1.01323	-0.126454	-0.0458298	-0.19698
	Y_{11}	Y_{12}	Y_{13}	Y_{14}
	26918.2	24139.7	0.253225	0.102224
	Y_{22}	Y_{23}	Y_{24}	
	36458.5	0.102372	0.295092	
	Y_{33}	Y_{34}		
	26274.5	23532.2		
	Y_{44}			
	35522.4			

Table 7.2: Expected yield as a function of the aTGCs. No form factor ($\Lambda_{FF} = \infty$) was used. CCCC and CCCF events are considered.

With the help of the signal parametrization shown in table 7.1 and 7.2, it is possible to set limits to the values of the triple gauge couplings. In the next section, a description of the limits extraction will be given.

7.3.2 aTGC Limits Extraction

The 95% confidence level intervals for the aTGCs are determined using a frequentist maximum profile-likelihood described in [53]. The implementation corresponds to the TGCLim package version 00-00-15, available for the use of the ATLAS collaboration. A description of the package is given in [54].

The basic idea behind the method is the maximization of the profile-likelihood function, L , with respect to the number of expected events, shown in the tables 7.1 and 7.2. The likelihood function can be written as:

$$L(f, \beta) = \prod_{i=1}^m \text{Poisson}(N_{data}^i, \phi^i(f, \beta)) \times \frac{1}{(2\pi)^m} e^{\frac{1}{2}(\beta \cdot C^{-1} \cdot \beta)} \quad (7.9)$$

where f are the neutral TGCs parameters and ϕ^i is the expected number of events in bin i :

$$\phi^i(f, \beta) = N_{sig}^i(f)(1 + \beta_i) + N_{back}^i(1 + \beta_{i+m}) \quad (7.10)$$

$N_{sig}^i(f)$ is the expected number of events as a function of the aTGCs. N_{sig}^i and N_{back}^i are parametrized as a function of the nuisance parameters β , that are introduced in order to make a description of the imperfect knowledge of the true N_{sig}^i and N_{back}^i and are taken from the uncertainties. C is a covariance matrix of the nuisance parameters.

A test statistic $q(f)$ is constructed as the ratio of two maximum profile-likelihood at a specific test value of the aTGCs parameters, f , to the full maximum profile-likelihood:

$$q(f) = \frac{L(N|f_{num}^{Max}, \beta_{num}^{Max})}{L(N|f_{den}^{Max}, \beta_{den}^{Max})} \quad (7.11)$$

where f_{num}^{Max} is the f that maximizes the numerator, and β_{num}^{Max} and β_{den}^{Max} the values of β that maximizes the numerator and denominator.

The distribution of $q(f)$ is made by running 10,000 pseudoexperiments, where the β parameters are Gaussian fluctuated from β_{den}^{Max} and the number of observed events is obtained randomly from a Poisson distribution around the considered f and β . The p-value, at the best value of the aTGCs parameters, is calculated as the fraction of pseudoexperiments, which have a test statistic smaller than the observed value of the test statistic $q(f)$. This process is repeated by scanning possible values of f and the 95% confident level is defined by all the values with p-value larger than 5%.

Limits are set for one parameter at a time, holding the other parameters to the SM value of zero, so one-dimensional confident levels are produced. In the table the limits derived using the previous described method are shown.

Λ_{FF}	f_4^γ	f_4^Z	f_5^γ	f_5^Z
3 TeV	[-0.009,0.011]	[-0.011,0.012]	[-0.009,0.011]	[-0.010,0.012]
∞	[-0.010,0.012]	[-0.008,0.010]	[-0.010,0.012]	[-0.008,0.010]

Table 7.3: One dimensional 95% confidence intervals for aTGCs derived from ATLAS results at $\sqrt{s} = 8$ TeV. Limits are presented for $\Lambda_{FF} = 3$ TeV and $\Lambda_{FF} = \infty$; both include the total systematics and statistical uncertainties.

Comparing the values shown in the table 7.3 to the previous limits derived from ATLAS results at a center of mass energy of $\sqrt{s} = 7$ TeV (see table 2.2), the new limits are 1.5-2 times more stringent than the previous limits.

Chapter 8

Conclusions

Studies of the ZZ production cross section are important, because they allow testing for the electroweak sector of the Standard Model. Searches for new physics are also possible if dibosons are produced via anomalous Triple Gauge Couplings. Data collected at the ATLAS experiment at a center of mass energy of $\sqrt{s} = 8$ TeV, were used to calculate the ZZ production cross section. Events were selected which were consistent with four electrons coming from two Z bosons.

Two fiducial phase spaces were used in this analysis: One corresponding to four electrons with values of the pseudorapidity in the interval $|\eta| < 2.5$ and a transverse momentum larger than 7 GeV (central phase space). A second smaller phase space was studied, which involved three electrons in the pseudorapidity interval $|\eta| < 2.5$ and one electron in the region of high pseudorapidity ($2.5 < |\eta| < 4.9$), and transverse momentum larger than 7 GeV for all electrons (central-forw. phase space). In both cases, the invariant mass of the two leptons was required to be in the range $66 < M_{\ell_1\ell_2} < 116$ GeV, with a separation $\Delta R_{\ell\ell}$ between leptons larger than 0.2. The fiducial cross section in each phase space, and for the combination was extrapolated to the total cross section, for ZZ production for Z bosons in the range 66 GeV to 116 GeV.

	central phase space	central-forw. phase space
σ^{fidu}	4.6 ± 0.6 (Stat.) ± 0.3 (Sys.) ± 0.1 (Lumi.) (fb)	1.3 ± 0.6 (Stat.) ± 0.3 (Sys.) ± 0.04 (Lumi.) (fb)
σ^{tot}	6.9 ± 1.0 (Stat.) ± 0.3 (Sys.) ± 0.2 (Lumi.) (pb)	7.4 ± 3.4 (Stat.) ± 0.2 (Sys.) ± 0.2 (Lumi.) (pb)

Combined

σ^{fidu}	6.0 ± 0.8 (Stat.) ± 0.3 (Sys.) ± 0.3 (Lumi) (fb)
σ^{tot}	7.3 ± 1.0 (Stat.) ± 0.4 (Sys.) ± 0.2 (Lumi) (pb)

The uncertainties in the measurements are statistically dominated and the major contribution to the systematic uncertainty arise due to the background estimation, using a data driven

method. The combined total cross section can be compared to SM expectation of:

$$\sigma_{ZZ}^{total}(pp \rightarrow ZZ + X) = 7.2_{-0.2}^{+0.3} \text{ pb} \quad (8.1)$$

Differential distributions of kinematic variables of the ZZ system were calculated and compared to the Standard Model expectation. No significant deviation was observed.

Limits on the anomalous neutral couplings were derived using the ZZ observed events and MC samples simulating anomalous Triple Gauge Couplings. A reweighting process was carried out to fit the MC samples to the most updated limits given by ATLAS. Then, 95% confidence level intervals for the aTGCs were determined using a frequentist maximum profile-likelihood method.

The results are shown below and are 1.5-2 times more stringent than previous limits obtained by other experiments.

Λ_{FF}	f_4^γ	f_4^Z	f_5^γ	f_5^Z
3 TeV	[-0.009,0.011]	[-0.011,0.012]	[-0.009,0.011]	[-0.010,0.012]
∞	[-0.010,0.012]	[-0.008,0.010]	[-0.010,0.012]	[-0.008,0.010]

In this work, the analysis was focused on the electron decay channel of the ZZ production, in order to show the effect of the inclusion of electrons with high values of pseudorapidity. It can be concluded that forward electrons could help to improve the measurement of the diboson production cross section, due to the increase in the acceptance of the detector.

A difficulty of considering only one decay channel is the low available statistics. Therefore this analysis can be improved if, additionally to the electron channel, other channels, e.g, 4μ , $2e2\mu$, are used. Detector effects can be reduced too, if an unfolding procedure is carried out on the kinematic distributions of the ZZ , like the ones shown in chapter 5. Naturally, the principal constraint in the use of forward electrons is the lack of information of the track system in that region. Plans are considered at the moment to extend the coverage of the track system up to $|\eta| = 3.2$ in the next LHC collision time (LHC-Run 3).

Bibliography

- [1] Steven Weinberg. A model of leptons. *Phys. Rev. Lett.*, 19(21):1264–1266, 1967.
- [2] Peter W. Higgs. Broken symmetries and the masses of gauge bosons. *Phys. Rev. Lett.*, 13(16):508–509, 1964.
- [3] Peter W. Higgs. Spontaneous symmetry breakdown without massless bosons. *Phys. Rev.*, 145(4):1156–1163, 1966.
- [4] R. Brandelik et al. Evidence for planar events in e^+e^- annihilation at high energies. *Physics Letters B*, 86(2):243 – 249, 1979.
- [5] Ch. Berger et al. Evidence for gluon bremsstrahlung in e^+e^- annihilations at high energies. *Physics Letters B*, 86(3-4):418 – 425, 1979.
- [6] W. Bartel et al. Observation of planar three-jet events in e^+e^- annihilation and evidence for gluon bremsstrahlung. *Physics Letters B*, 91(1):142 – 147, 1980.
- [7] D. P. et al. Barber. Discovery of three-jet events and a test of quantum chromodynamics at PETRA. *Phys. Rev. Lett.*, 43:830–833, 1979.
- [8] G. Arnison et al. Experimental observation of isolated large transverse energy electrons with associated missing energy at $\sqrt{s} = 540$ GeV. *Physics Letters B*, 122(1):103 – 116, 1983.
- [9] G. Arnison et al. Experimental observation of lepton pairs of invariant mass around 95 GeV/ c^2 at the CERN SPS collider. *Physics Letters B*, 126(5):398 – 410, 1983.
- [10] P. Bagnaia et al. Evidence for $Z^0 \rightarrow e^+e^-$ at the CERN pp collider . *Physics Letters B*, 129(1-2):130 – 140, 1983.
- [11] ATLAS Collaboration. Measurements of higgs boson production and couplings in diboson final states with the ATLAS detector at the LHC. *Physics Letters B*, 726(1-3):88 – 119, 2013.

- [12] S. Chatrchyan et al. Observation of a new boson at a mass of 125 GeV with the CMS experiment at the LHC. *Physics Letters B*, 716(1):30 – 61, 2012.
- [13] J. Beringer et al. Particle data group. *Phys. Rev. D* 86, 010001, 2012.
- [14] Noether Emmy. Invariante variationsprobleme. *Nachrichten von der Gesellschaft der Wissenschaften zu Göttingen, Mathematisch-Physikalische Klasse*, 1918:235–257, 1918.
- [15] A.D. Martin, W.J. Stirling, R.S. Thorne, and G. Watt. Parton distributions for the lhc. *The European Physical Journal C*, 63(2):189–285, 2009.
- [16] Sukanta Dutta, Ashok Goyal, and Mamta. New physics contribution to neutral trilinear gauge boson couplings. *The European Physical Journal C*, 63(2):305–315, 2009.
- [17] K. Hagiwara, R.D. Peccei, D. Zeppenfeld, and K. Hikasa. Probing the weak boson sector in $e^+e^- \rightarrow W^+W^-$. *Nuclear Physics B*, 282(0):253 – 307, 1987.
- [18] G. J. Gounaris, J. Layssac, and F. M. Renard. Signatures of the anomalous $Z\gamma$ and ZZ production at lepton and hadron colliders. *Phys. Rev. D*, 61:073013, 2000.
- [19] G. Aad et al. Measurement of ZZ production in pp collisions at $\sqrt{s} = 7$ TeV and limits on anomalous ZZZ and $ZZ\gamma$ couplings with the ATLAS detector. *Journal of High Energy Physics*, 2013(3):1–48, 2013.
- [20] P. Achard et al. Study of the process $e^+e^- \rightarrow Z\gamma$ at LEP and limits on triple neutral-gauge-boson couplings . *Physics Letters B*, 597(2):119 – 130, 2004.
- [21] G. Abbiendi et al. Study of Z pair production and anomalous couplings in e^+e^- collisions at \sqrt{s} between 190 GeV and 209 GeV. *The European Physical Journal C - Particles and Fields*, 32(3):303–322, 2003.
- [22] W Adam et al. Search for anomalous production of single photons at $\sqrt{s} = 130$ and 136 GeV. *Physics Letters B*, 380(3-4):471 – 479, 1996.
- [23] V.M. Abazov et al. Observation of ZZ Production in in $p\bar{p}$ Collisions at $\sqrt{s} = 1.96$ TeV . *Phys. Rev. Lett.*, 101:171803, 2008.
- [24] V.M. Abazov et al. $Z\gamma$ production and limits on anomalous $ZZ\gamma$ and $Z\gamma\gamma$ couplings in collisions at $\sqrt{s} = 1.96$ TeV. *Physics Letters B*, 653(5-6):378 – 386, 2007.
- [25] V.M. Abazov et al. Measurement of the ZZ production cross section and search for the standard model Higgs boson in the four lepton final state in in $p\bar{p}$ collisions. *Phys. Rev. D*, 88:032008, 2013.

BIBLIOGRAPHY

- [26] D. et al. Acosta. Measurement of $W\gamma$ and $Z\gamma$ Production in $p\bar{p}$ Collisions at $\sqrt{s} = 1.96$ TeV. *Phys. Rev. Lett.*, 94:041803, 2005.
- [27] Hung-Liang Lai, Marco Guzzi, Joey Huston, Zhao Li, Pavel M. Nadolsky, Jon Pumplin, and C.-P. Yuan. New parton distributions for collider physics. *Phys. Rev. D*, 82:074024, 2010.
- [28] A.D. Martin, W.J. Stirling, R.S. Thorne, and G. Watt. Parton distributions for the LHC. *The European Physical Journal C*, 63(2):189–285, 2009.
- [29] C. Oleari. The Powheg box. *Nuclear Physics B - Proceedings Supplements*, 205 206(0):36–41, 2010.
- [30] T. Binoth, N. Kauer, and P. Mertsch. Gluon-induced QCD corrections to $pp \rightarrow ZZ \rightarrow \ell\bar{\ell}\ell'\bar{\ell}'$. *Proceedings C08-04-07.1*, page 142, 2008.
- [31] Stefano Frixione and Bryan R. Webber. Matching NLO QCD computations and parton shower simulations. *Journal of High Energy Physics*, 2002(06):029, 2002.
- [32] Johan Alwall, Michel Herquet, Fabio Maltoni, Olivier Mattelaer, and Tim Stelzer. MadGraph 5: going beyond. *Journal of High Energy Physics*, 2011(6):1–40, 2011.
- [33] Michelangelo L. Mangano, Fulvio Piccinini, Antonio D. Polosa, Mauro Moretti, and Roberto Pittau. Alpgen, a generator for hard multiparton processes in hadronic collisions. *Journal of High Energy Physics*, 2003(07):001, 2003.
- [34] John M. Campbell, R. Keith Ellis, and Ciaran Williams. Vector boson pair production at the LHC. *JHEP*, 1107:018, 2011.
- [35] S. Agostinelli et al. Geant4 a simulation toolkit. *Nuclear Instruments and Methods in Physics Research Section A: Accelerators, Spectrometers, Detectors and Associated Equipment*, 506(3):250 – 303, 2003.
- [36] ATLAS Collaboration. ATLAS experiment. <http://www.atlas.ch/photos/detector-site-surface.html>, 2014. [Online; accessed 17-March-2014].
- [37] G. Aad et al. The ATLAS Experiment at the CERN Large Hadron Collider. *JINST*, 3:S08003, 2008.
- [38] F. Djama. Commissioning and operation of the ATLAS pixel detector at the CERN LHC collider. *JINST*, 6:C01082, 2011.
- [39] A Artamonov et al. The ATLAS Forward Calorimeter. *Journal of Instrumentation*, 3(02):P02010, 2008.

-
- [40] G. et al. Aad. Improved luminosity determination in pp collisions at $\sqrt{s} = 7$ TeV using the atlas detector at the lhc. *The European Physical Journal C*, 73(8):1–39, 2013.
- [41] ATLAS Collaboration. ATLAS experiment public results. https://twiki.cern.ch/twiki/bin/view/AtlasPublic/LuminosityPublicResults#2012_pp_Collisions, 2014. [Online; accessed 17-March-2014].
- [42] G. Aad et al. Electron performance measurements with the ATLAS detector using the 2010 LHC proton-proton collision data. *The European Physical Journal C*, 72(3):1–46, 2012.
- [43] J Kretzschmar and L Iconomidou-Fayard. Supporting document on electron performance measurements using the 2011 LHC proton-proton collisions. Technical Report ATL-COM-PHYS-2012-1023, CERN, Geneva, 2012. This is the Draft of the supporting document for the CONF note.
- [44] C Anastopoulos, E Benhar-Noccioli, A Bocci, K Brendlinger, F Bühner, L Iconomidou-Fayard, M Delmastro, O Ducu, R Fletcher, D Froidevaux, T Guillemin, S Heim, F Hubaut, M Karnevskiy, J Kretzschmar, J Kroll, C Lester, K Lohwasser, J B Maurer, A Morley, G Pásztor, E Richter-Was, A Schaffer, T Serre, P Sommer, E Tiouchichine, and H Williams. Supporting document on electron efficiency measurements using the 2012 LHC proton-proton collision data. Technical Report ATL-COM-PHYS-2013-1295, CERN, Geneva, 2013.
- [45] Wouter Verkerke and David P. Kirkby. The RooFit toolkit for data modeling. *eConf*, C0303241:MOLT007, 2003.
- [46] ATLAS Collaboration. ATLAS experiment. <https://twiki.cern.ch/twiki/bin/viewauth/AtlasProtected/ExtendedPileupRewighting>, 2014. [Online; accessed 3-May-2014].
- [47] ATLAS Collaboration. ATLAS experiment. <https://twiki.cern.ch/twiki/bin/view/AtlasProtected/EGammaCalibrationGEO20>, 2014. [Online; accessed 3-May-2014].
- [48] G. Aad et al. Measurement of the total ZZ production cross section in proton-proton collisions at $\sqrt{s} = 8$ TeV in 20 fb^{-1} with the ATLAS detector. Technical Report ATLAS-CONF-2013-020, CERN, Geneva, 2013.
- [49] S. Mrenna T. Sjostrand and P. Skands. Pythia 6.4 physics and manual. *Journal of High Energy Physics*, 2006(05):026, 2006.
- [50] T. Gleisberg, S. Höche, F. Krauss, M. Schönherr, S. Schumann, F. Siegert, and J. Winter. Event generation with sherpa 1.1. *Journal of High Energy Physics*, 2009(02):007, 2009.
- [51] U. Baur, T. Han, and J. Ohnemus. QCD corrections and anomalous couplings in $Z\gamma$ production at hadron colliders. *Phys. Rev. D*, 57:2823–2836, 1998.

BIBLIOGRAPHY

- [52] G. Bella. Weighting di-boson Monte Carlo events in hadron colliders. *arXiv:0803.3307 [hep-ph]*.
- [53] Glen Cowan, Kyle Cranmer, Eilam Gross, and Ofer Vitells. Asymptotic formulae for likelihood-based tests of new physics. *The European Physical Journal C*, 71(2):1–19, 2011.
- [54] ATLAS Collaboration. ATLAS experiment. <https://svnweb.cern.ch/trac/atlasphys/browser/Physics/StandardModel/ElectroWeak/Common/Software/TGC/TGClim/tags/TGClim-01-00-15/docs/TGClimManual.pdf>, 2014. [Online; accessed 21-April-2014].

Appendices

Appendix A

Monte Carlo Samples used in this Analysis

ZZ production and subsequent decays are simulated with the CT10 parton density function (PDF) set, and the generators `PowhegPythia` (NLO) and `ggVV` (LO). `PowhegPythia` is NLO, but does not include the NNLO gluon-gluon diagrams, which are expected to contribute 6% to the cross section. We simulate this contribution to the cross section using the `ggVV` generator. `ggVV` simulates the gluon-gluon process, which is an NNLO correction to the total cross section, at LO. The gauge-boson decays into τ leptons are included in the simulation with the τ leptons decaying into all known final states.

Table A.1 lists the ZZ MC signal samples used in this analysis, with the corresponding cross section, the k-factor needed to correct this to the full NLO prediction, and the event generator filter efficiency. In the `PowhegPythia` and `ggVV` samples, a filter is applied to the events at the generator level, demanding at least 3 leptons (e or μ) with $p_T > 5$ GeV and $|\eta| < 10$. The filter mainly rejects τ events. Only 0.05% of $ZZ \rightarrow \ell\ell\ell\ell$ ($\ell = e, \mu$) events are rejected for \sim on-shell ZZ production, i.e. for both Z boson masses in the range 66–116 GeV.

MCID	Process	Generator	Events	Fiducial k-factor	ϵ_{filter}	cross section [pb]
126937	$ZZ \rightarrow 4e$	<code>PowhegPythia</code>	600000	0.03	0.91	0.080
116601	$gg \rightarrow 4e$	<code>ggVV</code>	90000	1.00	1.00	0.000627

Table A.1: ZZ signal production process, cross section and number of fully simulated MC events. MC generator used to produce the MC events and the MC ID run number are indicated, as well.

Various MC samples are used to validate the data driven estimates for the background due to fake leptons. These include the main background contributions: W or Z gauge bosons produced in association with jets (V +jets), top events ($t\bar{t}$, Wt and single top), and other diboson processes (mainly WW and WZ).

The MC datasets used to model the backgrounds can be found in Tables A.2, A.3, and A.4.

MCID	Process	Generator	PDF	Events	Fiducial k-factor	ϵ_{filter}	cross section [pb]
108343	SingleTopSChanWenu	McAtNlo+Herwig	CT10	199997	1.00	1.00	0.606
117360	singletop_tchan_e	AcerMC+Pythia	CTEQ6L1	299899	1.00	1.00	9.480
110001	ttbar_dilepton	McAtNlo+Herwig	CT10	9988449	1.00	0.105	252.890
105200	ttbar_LeptonFilter	McAtNlo+Herwig	CT10	14990603	1.00	0.543	252.890
105204	ttbar_allhad	McAtNlo+Herwig	CT10	1199990	1.00	0.457	252.890
126928	WpWm_ee	Powheg+Pythia8	CT10	299700	1.00	1.00	0.631
129477	WZ_Wm11Z11	Powheg+Pythia8	CT10	190000	1.00	0.295	1.407
129486	WZ_W11Z11	Powheg+Pythia8	CT10	189899	1.00	0.297	0.980
119355	$t\bar{t}Z$	MadGraph+Pythia	CTEQ6L1	361611	1.00	1.00	0.068
167008	$ZZZ^* \rightarrow \ell\ell\ell$	MadGraph+Pythia	CTEQ6L1	49690	1.00	1.00	0.00033

Table A.2: Top, Diboson and Triboson MC datasets used as background samples. Values for the filter efficiency, number of events and cross section values were taken from AMI.

MCID	Process	Generator	PDF	Events	Fiducial k-factor	ϵ_{filter}	cross section [pb]
117650	ZeeNp0	Alpgen+Pythia	CTEQ6L1	6619984	1.18	1.00	718.890
117651	ZeeNp1	Alpgen+Pythia	CTEQ6L1	1329498	1.18	1.00	175.600
117652	ZeeNp2	Alpgen+Pythia	CTEQ6L1	404998	1.18	1.00	58.849
117653	ZeeNp3	Alpgen+Pythia	CTEQ6L1	109999	1.18	1.00	15.560
117654	ZeeNp4	Alpgen+Pythia	CTEQ6L1	30000	1.18	1.00	3.932
117655	ZeeNp5	Alpgen+Pythia	CTEQ6L1	10000	1.18	1.00	1.199

Table A.3: MC datasets for Z+jets and Z+ γ . Values for the filter efficiency, number of events and cross section values were taken from AMI.

MCID	Process	Generator	PDF	Events	Fiducial k-factor	ϵ_{filter}	cross section [pb]
146430	WgammaNp0	Photos+Herwig	CTEQ6L1	50000	1.15	1.00	230.090
146431	WgammaNp1	Photos+Herwig	CTEQ6L1	50000	1.15	1.00	59.343
146432	WgammaNp2	Photos+Herwig	CTEQ6L1	50000	1.15	1.00	21.469
146433	WgammaNp3	Photos+Herwig	CTEQ6L1	49999	1.15	1.00	7.103
146434	WgammaNp4	Photos+Herwig	CTEQ6L1	364999	1.15	1.00	2.122
146435	WgammaNp5	Photos+Herwig	CTEQ6L1	60000	1.15	1.00	0.466

Table A.4: MC datasets for W+jets and W+ γ . Values for the filter efficiency, number of events and cross section values were taken from AMI.

Appendix B

Signal and Background functions in Forward Region

In chapter 4, the reconstruction and identification of electrons in ATLAS was described. As already mentioned, the identification of electrons with high values of the pseudorapidity uses only information of the calorimeters, due to the non-coverage of the track system beyond of $|\eta| > 2.5$.

A fit procedure is implemented using RooFit[45] in the mass range 55 to 130 GeV, to make a separation of signal a background in forward region. The signal is fitted using a Crystal-Ball function, convoluted to a Breit-Wigner.

The Breit-Wigner function is shown in equation B.1, where M is the resonance pole, in this case corresponding to the mass of the Z and g is the resonance width. This function is commonly used to describe the shape of the resonance in the presence of a finite detector resolution.

$$f(x) = \frac{1}{(x - M)^2 + \frac{1}{4}g^2} \quad (\text{B.1})$$

The Crystal-Ball function is a Gaussian with a tail on the low side of the energy that is used to describe the effect of radiative energy loss. The function is shown in equation B.2.

$$f(x; \alpha, n, \bar{x}, \sigma) = N \cdot \begin{cases} \exp\left(-\frac{(x-\bar{x})^2}{2\sigma^2}\right), & \text{for } \frac{x-\bar{x}}{\sigma} > -\alpha \\ A \cdot \left(B - \frac{x-\bar{x}}{\sigma}\right)^{-n}, & \text{for } \frac{x-\bar{x}}{\sigma} \leq -\alpha \end{cases} \quad (\text{B.2})$$

where

$$A = \left(\frac{n}{|\alpha|}\right)^n \cdot \exp\left(-\frac{|\alpha|^2}{2}\right), \quad (\text{B.3})$$

$$B = \frac{n}{|\alpha|} - |\alpha|, \quad (\text{B.4})$$

$$N = \frac{1}{\sigma(C + D)} \quad (\text{B.5})$$

$$C = \frac{n}{|\alpha|} \cdot \frac{1}{n-1} \cdot \exp\left(-\frac{|\alpha|^2}{2}\right) \quad (\text{B.6})$$

$$D = \sqrt{\frac{\pi}{2}} \left(1 + \operatorname{erf}\left(\frac{|\alpha|}{\sqrt{2}}\right)\right) \quad (\text{B.7})$$

With the help of Z MC simulation parameters like mean of the Breit-Wigner are determined and used as start parameters when the data are fitted; the width of the Breit-Wigner is fixed to the PDG [13] value of the Z width. The exponential fall of the Crystal-Ball is fixed, too, with the help of the MC. The mean and sigma values of this function are fitted with the data.

The background is described with a Landau function. The mean and the sigma value of the function are determined using data. The typical form of the curves is shown in figure B.1. The left plot shows the Crystal-Ball function in red and the Breit-Wigner in solid blue. The convolution is shown in dashed blue. The Landau function can be seen in the right plot.

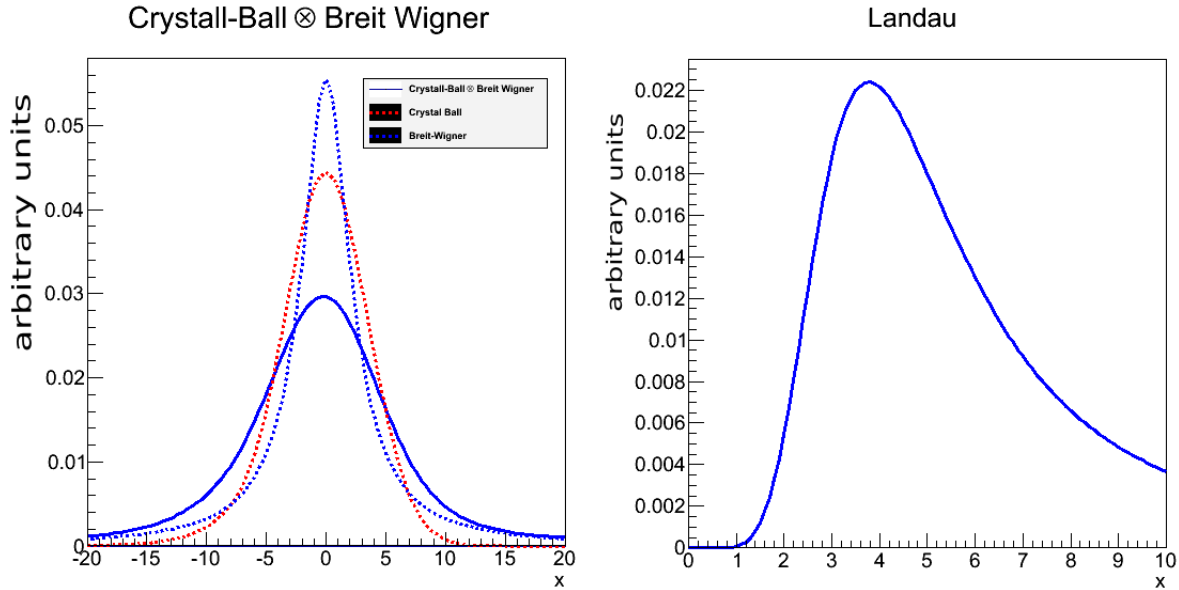


Figure B.1: Functions used to fit the data and the background, in order to have the number of electrons corresponding to signal and background.

Appendix C

Additional Kinematic Distributions of ZZ

In chapter 5, the kinematic distributions of the ZZ system and the electrons product of the decay of the Z bosons were shown. In this appendix, distributions are additionally shown, corresponding to the Z with the second larger p_T , referred to as subleading Z .

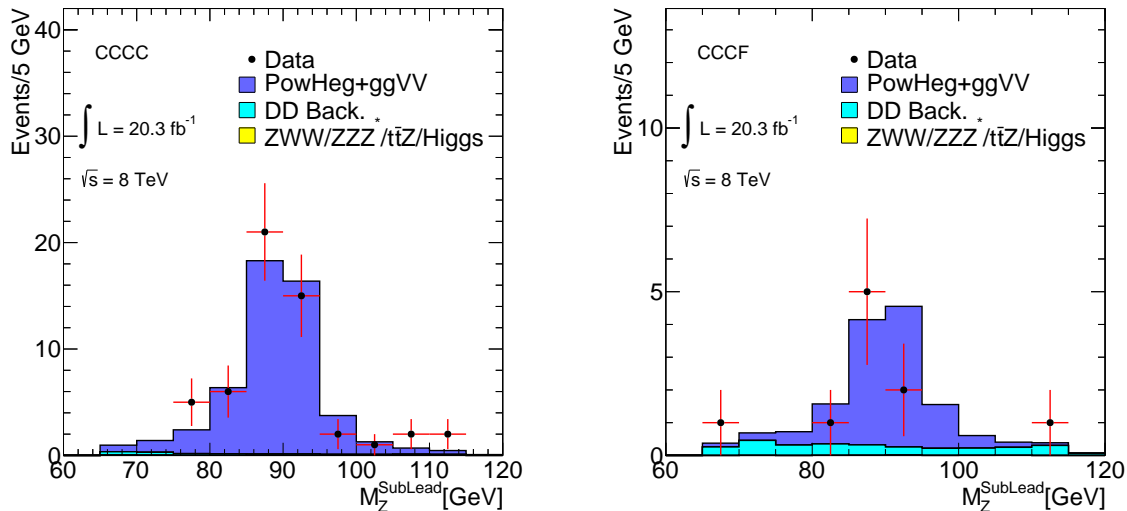


Figure C.1: Invariant mass of the Z candidate with the second larger p_T (subleading Z). The left side shows events with four central electrons. On the right side candidates with one forward electron and three central electrons are shown.

Figure C.1 shows the invariant mass of the subleading Z . The left side of the figure shows the invariant mass of events with four central electrons. The right side shows the invariant mass in the case of events with three central electrons and one forward. In both distributions, the MC signal shows a long tail in the low part of the $M_Z^{SubLead}$, that corresponds to electrons losing part of the energy, due to bremsstrahlung process. Compared with the distribution of the leading Z

(see chapter 5 fig. 5.8), the mass spectrum is wider; the reason is the lower resolution of the second Z with respect to the leading Z .

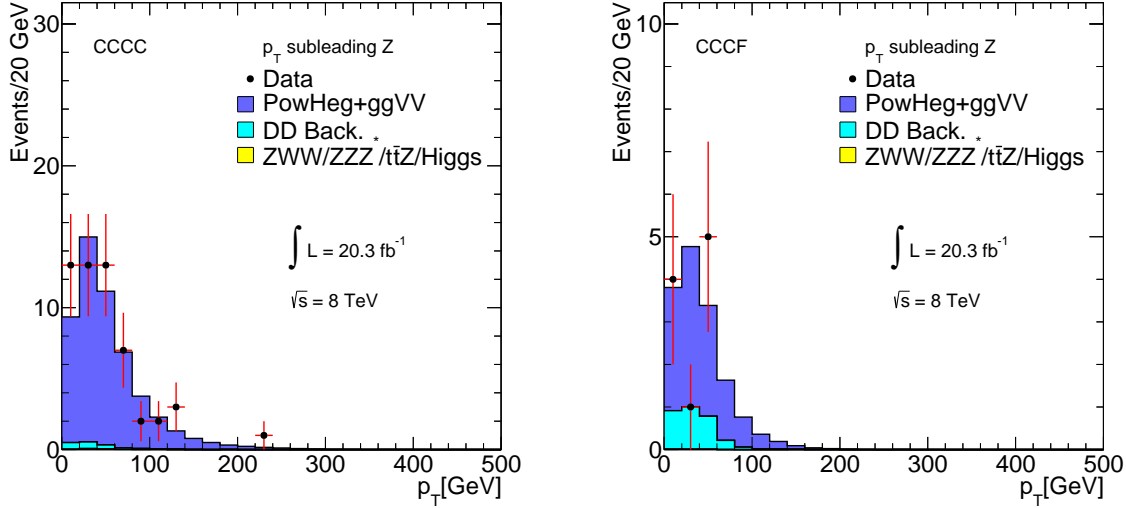


Figure C.2: p_T of the Z candidate with the second larger p_T (subleading Z). The left side shows events with four central electrons. On the right side candidates with one forward electron and three central electrons are shown.

In figure C.2, the p_T of the subleading Z is shown for the case of events with four central electrons (left side of figure) and in the case of three central electron and one forward. In both plots, it can be seen that the data agreement is relatively good, especially for the CCCC events. In the case of the CCCF events, statistical fluctuations are more important.

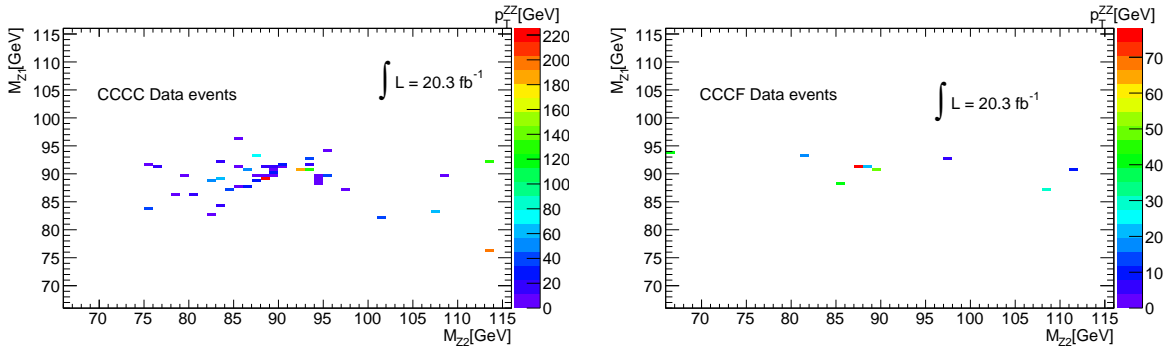


Figure C.3: Distribution of the ZZ candidates depending on the mass of the Z . On right side ZZ events with only central events are shown. The left side shows events with three central and one forward electron. y -axis corresponds to the mass of the Z , closer to the PDG value for the mass of the Z . The color shows the value of the p_T of the ZZ events.

Additionally to the p_T of the Z bosons, another classification of the Z consists of the distance of the mass of the Z with respect to the PDG nominal mass of the Z bosons. Two types of Z

are the result of this classification: the Z closest to the PDF mass of the Z , referred to as Z_{pole} , and the second closest called Z_{nopole}

Figure C.3 shows the mass of the Z closer to the PDG value of the mass of the Z versus the mass of the second Z . On right side of the figure, ZZ events, formed for central electrons (CCCC) are shown, on left side, events with three centrals and one forward electron can be seen (CCCF). The color of the points is proportional to the p_T of the ZZ .

Lebenslauf

- Persönliche Daten

Deywis Moreno-Lopez

Rheinallee 15

55118 Mainz

Geb. am 9.Dezember 1979 in Bogota, Kolumbien

Familienstand: Verheiratet

Nationalität: Kolumbianisch

- Schulbildung

02/1986-11/1990 CED San Agustin, Bogota, Kolumbien.

02/1991-11/1996 INEM Santiago Perez, Bogota, Kolumbien.

- Studium

02/1997-10/2004 Studium der Physik an der Universidad Nacional de Colombia, Bogota, Kolumbien.

03/2009-05/2011 Diplomarbeit in Physik an der Johannes-Gutenberg-Universität Mainz.

05/2011 Erledigung des Diploms in Physik an der Johannes-Gutenberg-Universität Mainz.

07/2011-05/2014 Promotionsstudium an der Johannes-Gutenberg-Universität Mainz.

06/2014 Erlangung des Grades Doktor der Naturwissenschaften an der Johannes-Gutenberg-Universität Mainz.